



Delft University of Technology

## Turbulent axisymmetric base flows Symmetry and long-term behavior

Gentile, Valeria

### DOI

[10.4233/uuid:1d2dc82e-685b-4a80-963b-3c6a3d0d165f](https://doi.org/10.4233/uuid:1d2dc82e-685b-4a80-963b-3c6a3d0d165f)

### Publication date

2017

### Document Version

Final published version

### Citation (APA)

Gentile, V. (2017). *Turbulent axisymmetric base flows: Symmetry and long-term behavior*. [Dissertation (TU Delft), Delft University of Technology]. <https://doi.org/10.4233/uuid:1d2dc82e-685b-4a80-963b-3c6a3d0d165f>

### Important note

To cite this publication, please use the final published version (if applicable).  
Please check the document version above.

### Copyright

Other than for strictly personal use, it is not permitted to download, forward or distribute the text or part of it, without the consent of the author(s) and/or copyright holder(s), unless the work is under an open content license such as Creative Commons.

### Takedown policy

Please contact us and provide details if you believe this document breaches copyrights.  
We will remove access to the work immediately and investigate your claim.

# **TURBULENT AXISYMMETRIC BASE FLOWS**

**SYMMETRY AND LONG-TERM BEHAVIOR**

Valeria Gentile



# **TURBULENT AXISYMMETRIC BASE FLOWS**

**SYMMETRY AND LONG-TERM BEHAVIOR**

## **Proefschrift**

ter verkrijging van de graad van doctor  
aan de Technische Universiteit Delft,  
op gezag van de Rector Magnificus prof.ir. K.C.A.M. Luyben;  
voorzitter van het College voor Promoties,  
in het openbaar te verdedigen op  
24 april 2017 om 12:30 uur

door

Valeria GENTILE  
Master in Aerospace and Aeronautical Engineering  
Sapienza University of Rome, Italië  
geboren te Crotone, Italië

Dit proefschrift is goedgekeurd door:

Promotor Prof.dr. F. Scarano

Copromotors Dr.ir. B.W. van Oudheusden, Dr.ir. F.F.J. Schrijer

Samenstelling promotiecommissie:

Rector Magnificus,

Prof.dr. F. Scarano,

Dr.ir. B.W. van Oudheusden,

Dr.ir. F.F.J. Schrijer,

voorzitter

Technische Universiteit Delft, promotor

Technische Universiteit Delft, copromotor

Technische Universiteit Delft, copromotor

Onafhankelijke leden:

Prof.dr.ir. L.L.M. Veldhuis,

Prof.dr. P. Schmid,

Prof.dr.-Ing. habil. C. Brücker,

Dr.ir. M. Vanierschot,

Prof.dr.-Ing. habil. S. Hickel,

Technische Universiteit Delft

Imperial College London

London City University

KU Leuven

Technische Universiteit Delft, reservelid

This research has been funded by the "Beatrix de Rijk" PhD grant awarded by the Faculty of Aerospace Engineering at TU Delft.

Cover photo by Valeria Gentile

Cover editing by Matteo Tiberi

Copyright © 2017 Valeria Gentile. All rights reserved.



*Male nun fa', paura nun ave'.*  
Anonymous

# SUMMARY

This thesis deals with the flow around truncated bodies of revolution. Such flows are encountered in a variety of engineering applications relevant to the aerospace transportation industry, notably to space launcher vehicles. The work focuses on the unsteady behavior of the wake and particularly on the dynamics of the recirculation region behind the base.

The manuscript starts with a survey of the past literature on the topic of turbulent axisymmetric wake flows. Salient aspects are discussed mainly in relation to flow topology and dynamical behavior. The vortex shedding process is examined along with the associated instabilities, namely the large-scale wake oscillations, the backflow azimuthal meandering and the transition scenarios exhibited by the wake across the different flow regimes.

Chapter 3 illustrates the current methodology of investigation. The flow facility and the geometrical models used in the experiments are described. The operating principles of the Particle Image Velocimetry (PIV) technique are summarized. The main contributions of uncertainty affecting the present results are defined. Details are provided of the Proper Orthogonal Decomposition (POD) procedure adopted in the analysis of the large-scale fluctuations.

The influence of base geometry and symmetry on the behavior of a turbulent incompressible reattaching flow is addressed in Chapter 4. Afterbody geometries with varying diameter ratios are discussed as to model axisymmetric backward facing step (BFS) flows of varying step heights. Any increase in the afterbody diameter induces earlier shear layer reattachment and inhibits the large-scale shear layer fluctuations. Comparison with equivalent planar BFS flows reveals an opposite scaling of the reattachment distance for the axisymmetric and the two-dimensional flow case, with convergence towards small values of the step height.

The large-scale fluctuations of the turbulent wake behind a circular base are spatio-temporally characterized in chapter 5. It is found that the wake dynamics is dominated by very-low-frequency backflow fluctuations in proximity of the stagnation point on the base, while it undergoes a global radial displacement closer to the rear-stagnation point.

The very-low-frequency turbulent wake unsteadiness is examined in chapter 6 under the effects of a small pitch angle. It is found that the reversed-flow region tends to stabilize away from the body axis of symmetry with increasing angles between the body and the freestream flow. Analysis of the instantaneous velocity field and



POD of the velocity fluctuations gives evidence of a backflow large-scale unsteadiness only within  $0.1^\circ$  deviations from axisymmetric inflow conditions.

The near-wake azimuthal organization in presence of an afterbody is analyzed in chapter 7 within different azimuthal-radial planes behind the base and for different diameter ratios. The afterbody is found not to alter the shear layer behavior significantly, but it interferes with the inner backflow meandering. It is shown that the wake unsteadiness of an afterbody flow is dominated by the shear layer development.

The main findings from the preceding chapters are summarized at the end of the manuscript. The conclusions of the present research are drawn and possible directions for future research on the topic of turbulent wake dynamics are outlined.

# SAMENVATTING

Dit proefschrift is gewijd aan de stroming rond afgeknotte omwentelingslichamen. Zulke stromingen komen voor in verschillende technische toepassingen die relevant zijn voor de luchtvaart- en ruimtevaartindustrie, zoals met name lanceerraketten. Het werk richt zich vooral op het instationaire gedrag van het zog en in het bijzonder op de dynamica van het terugstroomgebied direct achter de achterkant.

Het manuscript begint met een overzicht van de eerdere literatuur over het onderwerp van turbulente axiaalsymmetrische zogstromingen. De voornaamste aspecten worden besproken in relatie tot de topologie en het dynamische stromingsgedrag. Het proces van wervelafschudding is onderzocht samen met de bijbehorende instabiliteiten van het zog, namelijk de grootschalige oscillaties, de azimutale meandering van het terugstromingsgebied en de transities die het zog vertoont over de verschillende stromingsregimes.

Hoofdstuk 3 beschrijft de gevolgde onderzoeksmethode. De stromingsfaciliteit en de geometrische modellen die in de experimenten zijn gebruikt worden omschreven. De werkingsprincipes van de Particle Image Velocimetry (PIV) techniek worden samengevat. De belangrijkste bijdragen tot de onzekerheid in de huidige resultaten zijn gedefinieerd. Details worden gegeven van de Proper Orthogonal Decomposition (POD) procedure die is gebruikt bij de analyse van de grootschalige fluctuaties.

De invloed van de geometrie en symmetrie van de modelachterzijde op het gedrag van een heraanliggende onsamendrukbare turbulente stroming komt in hoofdstuk 4 aan de orde. Achterlichaam geometrieën met variabele diameterverhoudingen worden besproken, die zijn gemodelleerd als een axiaalsymmetrische achterwaarts gerichte stap (BFS = backward facing step) met variërende staphoogte. Een verhoging van de diameter van het achterste deel induceert een eerder heraanliggen van de losgelaten shear layer en belemmert de grootschalige fluctuaties ervan. Vergelijking met gelijkwaardige tweedimensionale configuraties vertoont een tegengestelde schaling van de afstand tot heraanliggen voor het axiaalsymmetrische en het tweedimensionale geval, met convergentie voor kleine waarden van de staphoogte.

De grootschalige fluctuaties van het turbulente zog achter een ronde achterzijde zijn ruimtelijk-temporeel gekarakteriseerd in hoofdstuk 5. Er is gevonden dat het zog wordt gedomineerd door zeer-laagfrequente fluctuaties van het terugstroomgebied in de nabijheid van het stuwpunt op de basis, terwijl deze een globale radiale verplaatsing ondergaat meer in de nabijheid van het achterste stuwpunt.

De gevolgen van een kleine instellingshoek op de zeer-laagfrequente turbulente zog wankel is onderzocht in hoofdstuk 6. Het blijkt dat met toenemende hoek tussen het lichaam en de vrijestroming het terugstroomgebied zich op afstand van de symmetrieas van het lichaam neigt te stabiliseren. Analyse van het instantane snelheidsveld en POD van de snelheidsfluctuaties tonen aan dat de grootschalige

beweging van het terugstroomgebied slechts optreedt binnen  $0,1^\circ$  afwijking van de axaalsymmetrische aanstroomconditie.

De azimuthale organisatie van het nabije zog in aanwezigheid van een achterlichaam wordt geanalyseerd in hoofdstuk 7, in verschillende azimuthaal-radiale vlakken achter het model en voor verschillende diameter verhoudingen. Het achterlichaam blijkt het gedrag van de shear layer niet aanzienlijk te veranderen, maar het interfereert met de meanderende beweging van het terugstroomgebied. Er wordt aangetoond dat het instationaire gedrag van het zog in aanwezigheid van een achterlichaam wordt gedomineerd door de ontwikkeling van de shear layer.

De voornaamste bevindingen uit de voorgaande hoofdstukken worden samengevat aan het einde van het manuscript. De conclusies van dit onderzoek worden getrokken en de mogelijke richtingen voor toekomstig onderzoek op het onderwerp van turbulente zogdynamica worden geschetst.

# TABLE OF CONTENTS

**CHAPTER 1.....1**

**INTRODUCTION .....1**

1.1 BACKGROUND..... 1

1.2 CURRENT KNOWLEDGE ..... 3

1.3 PRESENT RESEARCH OBJECTIVES..... 8

1.4 THESIS OUTLINE..... 10

**CHAPTER 2.....13**

**TURBULENT AXISYMMETRIC BASE FLOWS.....13**

2.1 BASE FLOW TOPOLOGY ..... 14

    2.1.1 *Separated flow features*..... 14

    2.1.2 *Influence of boundary conditions*..... 14

2.2 BASE FLOW BEHAVIOR ..... 17

    2.2.1 *Separated flow dynamics*..... 17

    2.2.2 *Antisymmetric mode  $m = 1$*  ..... 19

    2.2.3 *Very-low-frequency backflow unsteadiness*..... 21

    2.2.4 *Base flow symmetry and experimental sensitivity* ..... 24

    2.2.5 *Bifurcations and symmetry breaking modes*..... 25

**CHAPTER 3.....27**

**EXPERIMENTAL APPARATUS, MEASUREMENT TECHNIQUES AND DATA REDUCTION  
27**

3.1 EXPERIMENTAL APPARATUS ..... 28

    3.1.1 *Flow facility* ..... 28

    3.1.2 *Wind tunnel model*..... 28

3.2 PARTICLE IMAGE VELOCIMETRY ..... 32

    3.2.1 *Basic principles*..... 32

    3.2.2 *Stereoscopic PIV*..... 41

3.3 EXPERIMENTAL UNCERTAINTY ..... 44

3.4 PROPER ORTHOGONAL DECOMPOSITION ..... 47

**CHAPTER 4.....51**

**AFTERBODY EFFECTS ON AXISYMMETRIC BASE FLOWS .....51**

4.1 INTRODUCTION ..... 52

4.2 EXPERIMENTAL SETUP..... 53

    4.2.1 *Flow facility and wind tunnel model* ..... 53

    4.2.2 *Measurement apparatus and procedure* ..... 54

    4.2.3 *Data processing and assessment* ..... 56

4.3	RESULTS .....	56
4.3.1	<i>Boundary layer properties</i> .....	56
4.3.2	<i>Mean flow field</i> .....	57
4.3.3	<i>Shear layer development</i> .....	61
4.3.4	<i>Turbulence statistics</i> .....	62
4.3.5	<i>Proper Orthogonal Decomposition</i> .....	66
4.4	CONCLUSIONS.....	71
<b>CHAPTER 5.....</b>		<b>73</b>
<b>LOW-FREQUENCY BEHAVIOR OF THE TURBULENT AXISYMMETRIC NEAR-WAKE.....</b>		<b>73</b>
5.1	INTRODUCTION .....	75
5.2	EXPERIMENTAL SETUP.....	76
5.2.1	<i>Flow facility and wind tunnel model</i> .....	76
5.2.2	<i>Measurement apparatus and procedure</i> .....	77
5.2.3	<i>Data processing and assessment</i> .....	77
5.3	RESULTS .....	78
5.3.1	<i>Flow Field Statistics</i> .....	79
5.3.2	<i>Instantaneous flow field analysis</i> .....	82
5.3.3	<i>Proper orthogonal decomposition</i> .....	87
5.4	CONCLUSIONS.....	98
<b>CHAPTER 6.....</b>		<b>99</b>
<b>THE INFLUENCE OF FLOW SYMMETRY ON THE LONG-TERM BACKFLOW UNSTEADINESS</b>		
<b>99</b>		
6.1	INTRODUCTION .....	100
6.1.1	<i>Very-low-frequency wake behavior</i> .....	100
6.1.2	<i>Dynamical model of the backflow centroid motion</i> .....	101
6.2	EXPERIMENTAL SETUP.....	102
6.3	RESULTS .....	103
6.3.1	<i>Mean and instantaneous backflow behavior</i> .....	103
6.3.2	<i>Proper Orthogonal Decomposition</i> .....	110
6.4	CONCLUSIONS.....	112
<b>CHAPTER 7.....</b>		<b>115</b>
<b>AZIMUTHAL ORGANIZATION AND UNSTEADINESS OF AN AFTERBODY FLOW .....</b>		<b>115</b>
7.1	INTRODUCTION .....	116
7.2	EXPERIMENTAL SETUP.....	116
7.3	RESULTS .....	118
7.3.1	<i>Flow field statistics</i> .....	118
7.3.2	<i>Backflow unsteadiness</i> .....	119
7.3.3	<i>Proper Orthogonal Decomposition</i> .....	120
7.4	CONCLUSIONS.....	121

<b>CHAPTER 8.....</b>	<b>123</b>
<b>CONCLUSIONS AND RECOMMENDATIONS .....</b>	<b>123</b>
8.1 INFLUENCE OF THE BASE GEOMETRY ON THE SEPARATED FLOW BEHAVIOR .....	123
8.2 STREAMWISE DEVELOPMENT OF THE LARGE-SCALE WAKE UNSTEADINESS .....	124
8.3 RELATION BETWEEN FLOW SYMMETRY AND VERY-LOW-FREQUENCY WAKE UNSTEADINESS.....	125
8.4 INFLUENCE OF THE BASE GEOMETRY ON THE AZIMUTHAL WAKE ORGANIZATION AND LARGE-SCALE UNSTEADINESS.....	126
<b>REFERENCES .....</b>	<b>127</b>
<b>LIST OF PUBLICATIONS.....</b>	<b>132</b>
<b>CURRICULUM VITAE .....</b>	<b>134</b>
<b>ACKNOWLEDGEMENTS .....</b>	<b>135</b>



# CHAPTER 1

## INTRODUCTION

### 1.1 Background

The complexity of axisymmetric base flows challenges human talents since the early thousands. In his *Livres des merveilles du monde* (ca. 1300) Marco Polo reported of tubes filled with gunpowder and used as aerial fireworks during religious festivity in Song's China. These so-called *fire arrows* were equipped with a bamboo elongation to increase trajectory stability and became useful as incendiary weapons against the invasion of the Mongols (Fig. 1.1). After the Mongolian's siege of Baghdad in 1258 this technology spread to Middle East and Europe and has been developing ever since.



**Figure 1.1** Chinese rockets against Mongol army during the battle of Kai-Keng in 1232. Painting by Charles Hubbell. Courtesy of TRW Inc. and Western Reserve Historical Society, Cleveland (Ohio).

The need for understanding and controlling the motion of such objects triggered a great deal of research in the field of external ballistics, leading to the adoption of a standard elongated blunt-based ogive-nosed configuration (cf. Siacci 1888). The latter influences the design of warfare and space transportation vehicles to the present days (Fig. 1.2).

For these configurations the flow behavior in proximity of the blunt base, viz. *base flow*, has major consequences on the performance of the body with respect to both drag and stability. This makes base flow aerodynamics a most engaging research topic not solely with relevance to the military sector, but also to other

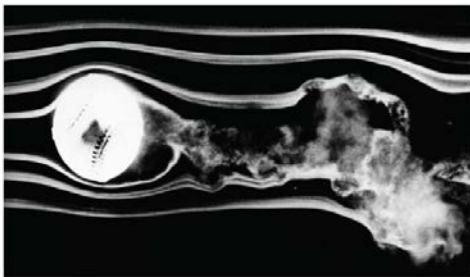


applications, ranging from the aerospace and marine transportation industry to the sport field.

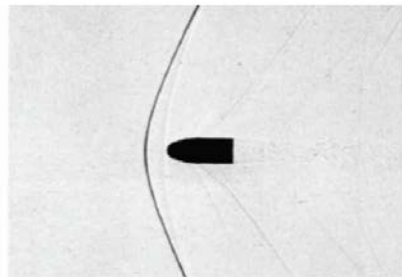


**Figure 1.2 Bumper 5 launch in 1945.**

To date base flow aerodynamics has built upon a century of researches. Systematic experimental studies began in the late 1800's with the invention of wind tunnels and the first test campaigns performed among others by Tsiolkowsky and Reynolds. The first research efforts mainly relied on flow visualization by means of tracers like dye, smoke or oil (Fig. 1.3a) or on optical methods such as Schlieren photography and shadowgraphy (Fig. 1.3b).



a)



b)

**Figure 1.3 Smoke visualization of a spinning baseball (a). Shadowgraphy of a bow shock in front a rifle bullet (b). From van Dyke (1982).**

The subsequent developments in the field of flow diagnostics allowed for retrieving quantitative information through probe-based measurement techniques such as hot wire anemometry (HWA) and later by means of non-intrusive optical measurement techniques like Laser Doppler Velocimetry (LDV) and particle image velocimetry (PIV, cf. Westerweel *et al* 2012). To date the progress made in the direction of high speed tomographic PIV (cf. Scarano 2012) allows for obtaining time-resolved information of entire volumes of flow.

The concurrent advancements in the informatics further opened the way to the numerical examination of base flows, either by discretization of the governing Navier-Stokes equations, which technique is known as *computational fluid dynamics* (CFD), or by their direct numerical simulation (DNS). Particularly the introduction of supercomputers has allowed for treating increasingly complex flow phenomena, like those associated with transonic speeds and with turbulence, which represent typical base flows scenarios.

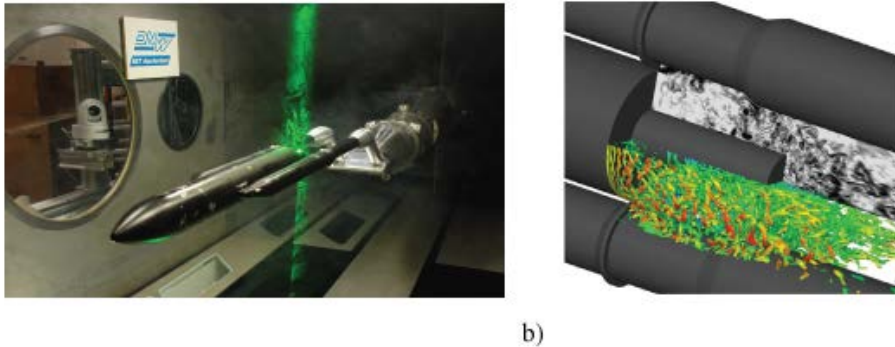


**Figure 1.4** PIV measurement setup for the investigation of the transonic base flow of a 1:60 Ariane 5 model (a), from Schrijer *et al* (2011). Isosurfaces of streamwise vorticity of a transonic base flow obtained by ZDES for a simplified launcher afterbody (b), from and Pain *et al* (2014).

The above progress in the field of both experimental and numerical aerodynamics has allowed for an ample characterization of base flows over the past years. Peculiarities could be identified, which served the understanding and prediction of these flows in the context of industrial applications. At high Reynolds numbers which are relevant to the engineering field, the topic of base flow dynamics emerges as being particularly complex. Contributions in the context of turbulence (cf. Townsend 1956), especially with regards to the discovery of *coherent* motions, have shed light on important mechanisms of the base flow dynamics and significantly helped modeling their behavior (cf. Lumley 1967). However, new complexities keep on being identified, which raise new topics of discussions.

## 1.2 Current knowledge

### Base flow separation and near-wake topology

The motion of a bluff-reared body in a viscous fluid is always accompanied by a massive flow separation in the back. As the flow detaches from the rear-surface it curves its trajectory and forms a stagnation point downstream of the base. The

outermost fluid in this region develops as a *shear layer*, whereas the innermost fluid reverses its trajectory forming a further stagnation point on the base (Fig. 1.5). The velocity defect developing between the base of the body and the rear-stagnation point is referred to as the *body near-wake*. Its presence is associated with an additional drag contribution called *base drag* (Roshko 1955) whose reduction has been the focus of many investigations to the present days (cf. Choi *et al* 2008). While most bluff-based geometries exhibit a similar organization, data gathered from past studies also highlight a number of parameters influencing the near-wake topology. The latter could be mainly related to the geometry of the body, e.g. its *bluffness*, and the inflow conditions, e.g. the state of the incoming boundary layer.

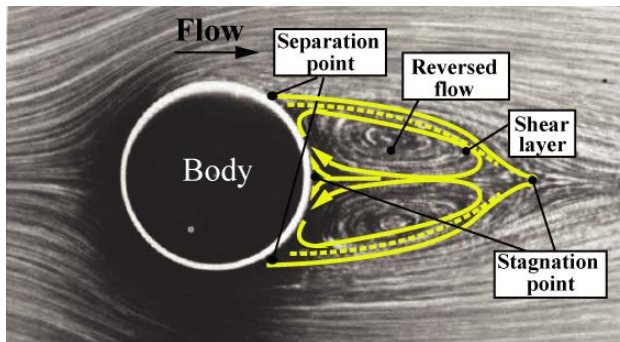


**Figure 1.5** Schematics of the near-wake flow past a cylinder at  $Re_D = 26$ . Adapted from van Dyke (1982).

### Base flow dynamics and vortex shedding

The wake generated by a cylinder in cross-flow, or *circular cylinder*, is one of the most documented wake flows in literature. This geometry induces a two-dimensional flow separation whose streamwise location varies according to the flow regime (cf. Williamson 1996).

The former analyses conducted by Gerrard (1966) on this kind of flow highlighted important interactions occurring across the shear layer and involving the inner reversed flow and the outer higher speed flow. At the Reynolds numbers of interest to most applications, viz. diameter-based  $Re_D > 10^2$ , these interactions are associated with a periodic shedding of streamwise oriented vortices from alternate sides of the body and with alternate sense of rotation. The shedding and development of these structures generates a so-called *vortex street* downstream of the body (Fig. 1.6) and has been linked with the occurrence of self-sustained large-scale oscillations of the wake (Provansal *et al* 1987; Monkewitz 1988).

The shedding frequency is found to be essentially constant in the fully turbulent regime, viz. diameter-based  $Re_D > 10^3$  (Gerrard 1966), not only in the circular cylinder case, but also in other wake flows, such as those occurring past prisms (van Oudheusden 2005) and spheres (Achenbach 1974). This characteristic frequency

is often expressed in terms of the convective time-scales of the shed vortices using the diameter-based Strouhal number  $St_D = fL/U_\infty$ , where  $U_\infty$  is the freestream velocity and  $L$  indicates a characteristic dimension of the body, e.g. the base diameter for axisymmetric bodies. Typically, the Strouhal number identified with the vortex shedding phenomenon is in the order of  $St_D \sim 10^{-1}$ , with minor variations depending on the specific geometry (Calvert 1967; Roshko 1955).

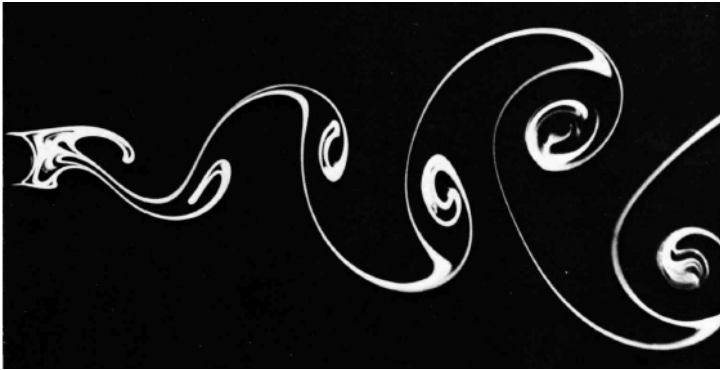


**Figure 1.6** Karman vortex street past a circular cylinder at  $Re_D = 140$ . Adapted from van Dyke (1982).

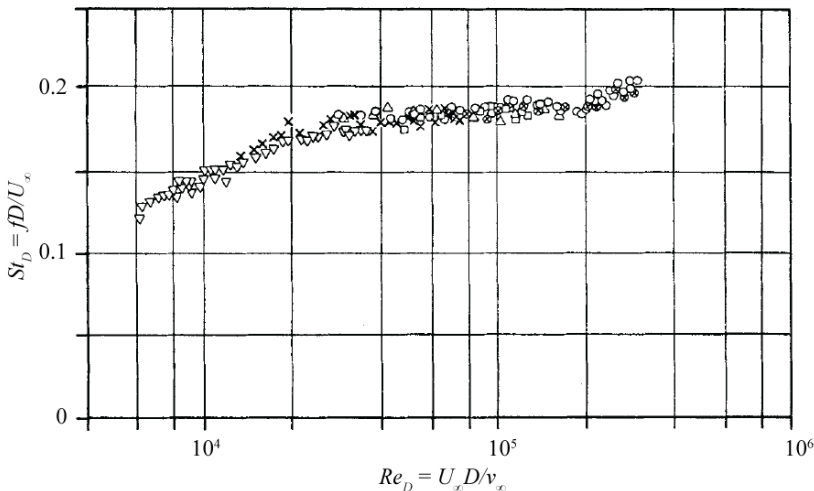


**Figure 1.7** Diameter-based Strouhal number as a function of the diameter-based Reynolds number for spheres of increasing diameters. Adapted from Achenbach (1974).

### Axisymmetric base flow unsteadiness: helical mode $m = 1$

The occurrence of vortex shedding has been linked with an absolute instability of the shear layer (Chomaz 2005) and thus, concerns a variety of wake flows regardless

of their specific geometry. Nonetheless, the spatial distribution of the fluctuations resulting from the shedding process appears strongly affected by the symmetry of the base. In particular, for bodies of revolution, such as spheres and disks oriented perpendicular to the freestream (Achenbach 1974; Fuchs *et al* 1979), it has been shown that the vortices are shed off the body as a pair of counter-rotating helices, which pattern yields anti-symmetric fluctuations of the wake.



**Figure 1.8** Flow visualization of the wake past a sphere at  $Re_D = 202$ . Adapted from Taneda (1956).

These fluctuations are typically identified with a dominant mode  $m = 1$ , often called *helical* mode, and represent a major concern for many industrial applications. In the context of the present work, a relevant example is the base flow of a space launcher, in which case the helical mode can trigger transonic buffeting on the nozzle protruding from the main stage. Such flow cases are widely treated in literature, especially with respect to the design of flow control strategies (cf. Schrijer *et al* 2011).

More fundamental research is also conducted on analogous, but simpler, bodies of revolution featuring a blunt trailing edge and a protruding cylinder of smaller diameter, viz. afterbody (cf. Dépres *et al* 2004; Deck and Thorigny 2009). The separated flow field around these simpler configurations (Fig. 1.9) displays essentially the same major features as the space launcher base flow. As such, it is usually treated as a reference case for the study of the latter more complex geometries and is also the object of the present research.

The latter erratic behavior is shown to dominate the wake dynamics of bluff-based bodies (Fig. 1.10), inducing anti-symmetric fluctuations at a characteristic frequency in the order of  $St_D \sim 10^{-3}$  (Rigas *et al* 2014; Grandemange *et al* 2014). This seemingly random behavior is currently considered as a *very-low-frequency* contribution to the helical mode  $m = 1$  and has been linked with a continuous reorientation of the shedding process along the azimuth.

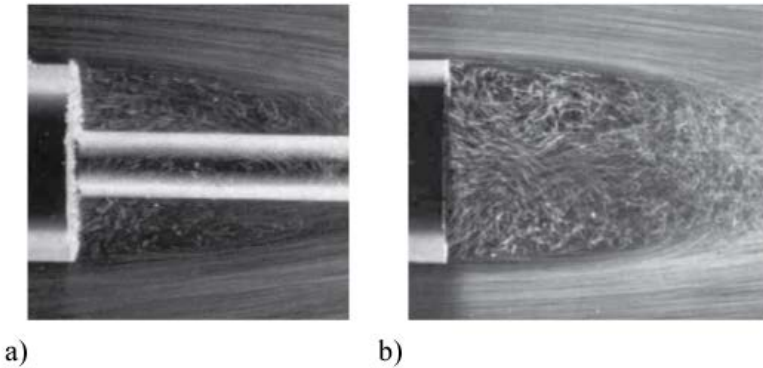


**Figure 1.9** Axisymmetric wake flow past a truncated body of revolution with (a) and without central protrusion (b).  $Re_D = 10,000$ . Adapted from van Dyke (1982).

As a result of this long-term instability the azimuthal-radial topology of the wake evolves continuously and very slowly recovering its axial symmetry only in a long-term average sense. The studies conducted in the framework of bifurcation theory (cf. Fabre *et al* 2008; Bury *et al* 2012) consider this behavior as a chaotic state attained at fully turbulent regime after several wake transitions. The turbulent wake flows past annular jets (Vanierschot and Van den Bulck 2011) as well as square-back bodies (Grangemange *et al* 2012b) are also found to feature an analogous very-low-frequency unsteadiness.

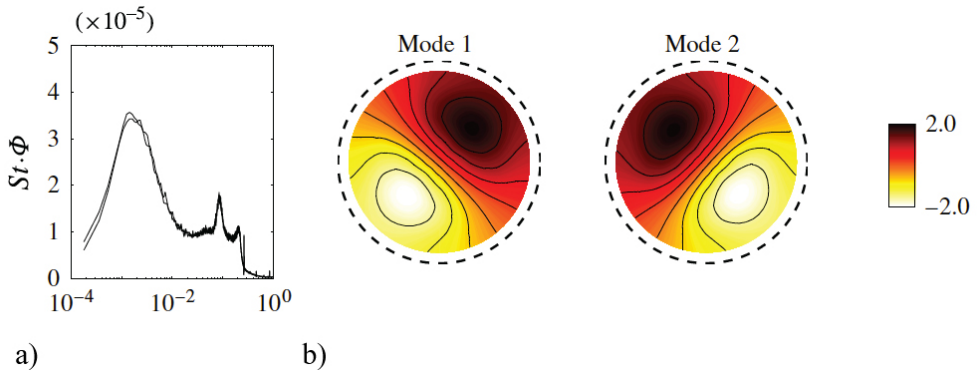


**Figure 1.10** Anti-symmetric pressure fluctuating modes 1 and 2 with  $|m| = 1$  on the base of a blunt-based cylinder. Frequency spectra (a). Color contours (b).  $Re_D \sim 10^5$ . Adapted from Rigas *et al* (2014).

The occurrence of a long-term backflow meandering is currently considered as the origin of the well-known turbulent wake sensitivity towards the experimental boundary conditions. The latter used to be entirely attributed to the experimental setup, namely the presence of a wind tunnel model support (see Fig. 1.11) and the

accuracy of the wind tunnel model orientation with respect to the freestream flow. In particular, it was shown by Wolf *et al* (2013) that sideslip angles of  $0.3^\circ$  between the wind tunnel model and the freestream flow can completely disrupt the symmetry of the near-wake. Further studies linked the presence of the model support to the occurrence of momentum deficits (Wolf *et al* 2010) and even of preferred azimuthal periodicities (Grandemange *et al* 2012a), with major effects on the near-wake axisymmetry.

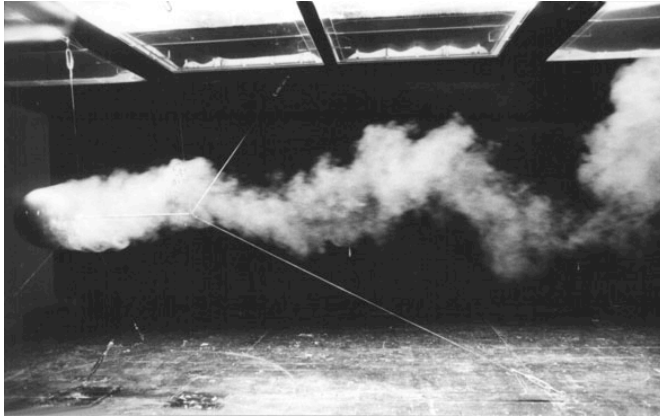


**Figure 1.11** Sphere suspended in a wind tunnel by wires during a flow visualization experiment.  $Re_D = 2.3 \cdot 10^5$ . From Taneda (1956).

Notwithstanding the importance of an accurate experimental setup, the occurrence of a very-low-frequency instability makes the symmetry a merely statistical feature, which is only achievable upon averaging a sufficient number of asymmetric topologies. Most importantly, the analysis of this particularly long-term instability requires an adequate observation-time. The latter imposes significant constraints not only to experimental investigations, but also in the context of a numerical study of such flows.

### 1.3 Present research objectives

The foregoing literature review shows that turbulent base flows are intrinsically unsteady due to the large-scale separation at the trailing edge with formation of a wake region and to the subsequent onset of a vortex shedding process. The symmetry of the flow emerges as being crucial in determining both the mean topology and the fluctuating base flow behavior. The latter appears to be dominated by the vortex shedding process as well as by the long-term meandering of the inner backflow region.

Although previous research efforts have shed light on several aspects of the turbulent wake behavior, other aspects still require further investigation. These points are addressed in terms of the following research questions:

### *Influence of the base geometry on the separated flow behavior*

The unsteady character that a wake flow exhibits at high Reynolds numbers is strongly dependent on its spatial organization (cf. Gerrard 1966). Former parametric investigations show that the bluntness of the body has a strong influence on both the extension of the velocity defect and the characteristic frequency of its fluctuations (cf. Roshko 1955; Calvert 1967). Similarly, the organization and unsteady behavior of the so-called afterbody flows, e.g. those occurring in the base region of a space launcher, are shown to change dramatically depending on the elongation of the central protrusion with respect to the base (Dépres *et al* 2004; Wolf *et al* 2012).

Currently, the majority of the information on these turbulent reattaching flows is retrieved from the data available on planar BFS geometries. Such flows are often regarded in literature as the planar counterpart of afterbody flows due to a number of shared similarities. However, the data obtained for axisymmetric BFS geometries (cf. Hudy *et al* 2005) reveal important differences between the two-dimensional and the axisymmetric case.

The present work aims at assessing the extent of these differences by examining the influence of the base symmetry on the behavior of the separated flow. Further objective is to determine how the development of the separated flow is affected by the base geometry.

### *Streamwise development of the large-scale wake unsteadiness*

Turbulent wake flows display a typical large-scale unsteadiness, which is unanimously ascribed to a vortex shedding process (Oertel 1990; Williamson 1996) occurring with a characteristic non-dimensional frequency  $St_D \sim 10^{-1}$  (Fuchs *et al* 1979). More recent studies report of an additional unsteadiness mechanism consisting in a meandering of the inner recirculation region along the azimuth with characteristic frequency in the order of  $St_D \sim 10^{-3}$  (cf. Rigas *et al* 2014). Currently these two instabilities are identified with two distinct contributions of the same fluctuating mode, namely the *helical* mode  $m = 1$ .

Past investigations have thoroughly characterized the streamwise development of the fluctuations induced by the helical mode, due to its relevance to industrial flow configurations, e.g. space launcher vehicles. On the other hand, the azimuthal backflow meandering has been only discussed at isolated streamwise stations.

The present research aims at characterizing the streamwise development of both unsteady mechanisms.



### Relation between flow symmetry and very-low-frequency wake unsteadiness

The most recent discussions on the subject of turbulent wake flows focus on understanding the long-term erratic motion of the inner recirculation region (cf. Rigas *et al* 2014, 2015). This behavior is documented as an important wake instability for a variety of configurations (cf. Vanierschot and Van den Bulck 2011; Grandemange *et al* 2014) and is found to affect both the short and the long-term wake topology significantly. The sensitivity of turbulent wake flows towards the experimental boundary conditions is currently attributed to this long-term wake unsteadiness and has been examined in a number of parametric studies (cf. Wolf *et al* 2013; Ashok *et al* 2015a, b; Grandemange *et al* 2012). Among those dealing with axisymmetric geometries, none has elaborated on the link with the above long-term backflow unsteadiness, which appears inherently related to the symmetry of the flow.

One of the present research objectives is to investigate the effects of angular misalignments on the very-low-frequency backflow dynamics.

### Influence of the base geometry on the azimuthal wake organization and large-scale unsteadiness

Afterbody flows are often regarded as a model of the turbulent base flow occurring behind space launcher vehicles. Their streamwise development has been comprehensively treated, both with regards to the mean wake topology and the ensuing fluctuating field (cf. Schrijer *et al* 2014). On the other hand, the information on the azimuthal-radial organization of such flows could be retrieved mainly from pointwise wall-pressure measurements or numerical simulations (cf. Deck and Thorigny 2007; Pain *et al* 2014). The experimental results of Dépres *et al* (2004) and Wolf *et al* (2012) have shown that the presence of the afterbody, viz. of a nozzle in the real flow case, can have a significant impact on the shear layer development. However, its influence on the large-scale azimuthal wake organization has not been yet examined.

## 1.4 Thesis outline

The most relevant aspects of turbulent axisymmetric wake flows have been briefly reviewed in this chapter. The main points of discussions which have been raised define the scope of the present work.

A more detailed literature survey on the topic of turbulent axisymmetric base flows is addressed in **chapter 2**. The topological features of separated flows behind bluff bodies of revolution are outlined. The onset of the vortex shedding phenomenon and the major instability mechanisms associated with it are examined. The related issue of the turbulent wake flow sensitivity is discussed. The wake

topology transitions experienced by the wake over the different flow regimes are illustrated.

An overview of the current methodology of investigation is provided in **chapter 3**. The flow facility and the wind tunnel model configurations considered in the present experiments are described. The operating principles of PIV and stereoscopic PIV are illustrated. The main uncertainty contributions affecting the present results are discussed. Details are given on the mathematical procedure of the POD adopted in the data reduction.

**Chapter 4** investigates the influence of the base geometry on the behavior of a turbulent separating and reattaching flow. Axisymmetric and planar BFS flows are analyzed for varying step heights. It is shown that the symmetry of the base leads to crucial differences between the axisymmetric and the planar BFS flow reattachment.

The streamwise evolution of the turbulent near-wake *low-frequency* unsteadiness is characterized in **chapter 5**. It is shown that the dynamics of the near-wake tends to be dominated by the backflow fluctuations in proximity of the base and by the fluctuations due to the shear layer development closer to the rear-stagnation point.

The erratic behavior of the inner backflow region is examined in **chapter 6** under the effects of small pitch angles. It is shown that the wake is affected by a very-low-frequency unsteadiness only for axisymmetric or nearly axisymmetric inflow conditions.

**Chapter 7** investigates the influence of a central protrusion on the azimuthal topology and large-scale organization of a turbulent afterbody flow. Even for small diameter ratios the afterbody is found to inhibit the inner backflow meandering.

**Chapter 8** summarizes the findings of the preceding chapters and draws the main conclusions of the present work.



## CHAPTER 2

*“Chaos in the middle of chaos isn’t funny,  
but chaos in the middle of order is”*

Steve Martin

## TURBULENT AXISYMMETRIC BASE FLOWS

**Abstract** A review of the existing literature on the topic of axisymmetric turbulent wakes is addressed in this chapter. The most relevant results are reported and discussed in relation to the near-wake topology and dynamics.

## 2.1 Base flow topology

### 2.1.1 Separated flow features

When an elongated bluff-body of revolution moves in a viscous incompressible fluid, the abrupt geometrical discontinuity on the back induces a massive flow separation. The latter creates a region of velocity defect whose size is comparable to the body cross-section and is thus, said to be of *large-scale*.

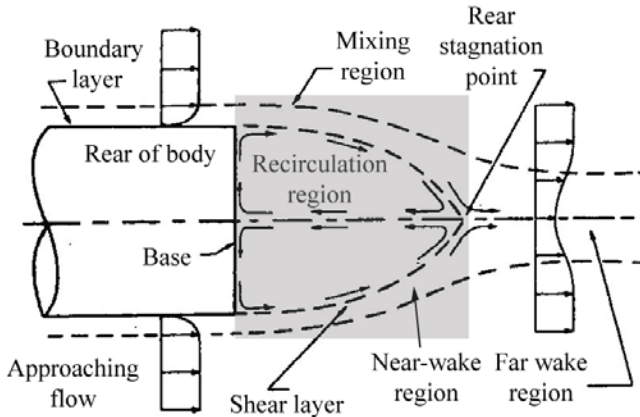


**Figure 2.1** Separated flow topology behind a truncated-base body. Near-wake region indicated by gray shading. Adapted from Merz *et al* (1978).

A schematic illustration of the separated flow behind a truncated cylinder aligned with the freestream is presented in Fig. 2.1. The flow region delimited by the curvature of the detaching flow between the separation point on the base and the so-called *rear-stagnation point* is referred to as *near-wake* of the body. The extension of this region in the streamwise direction is commonly called *reattachment length* or *distance*.

The innermost flow rolls up and reverses its trajectory forming two diametrically opposite vortical patterns, whose cores are identified as the near-wake *foci* (D elery 2001). In the case of an axisymmetric body these vortical structures define a toroidal *recirculation region* in the azimuthal-radial plane of the wake. The latter is separated from the outer higher speed unperturbed flow by a free *shear layer*, which thickens in the streamwise direction as the velocity defect recovers away from the body.

### 2.1.2 Influence of boundary conditions

The features above apply to all flows past blunt-based geometries. Nonetheless, former studies show that the organization of the near-wake is influenced by a number of factors, mainly related to inflow and geometrical boundary conditions.

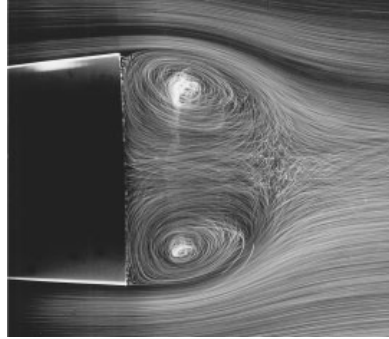


**Figure 2.2** Flow separation over a blunt trailing edge. From Délerly (2001).

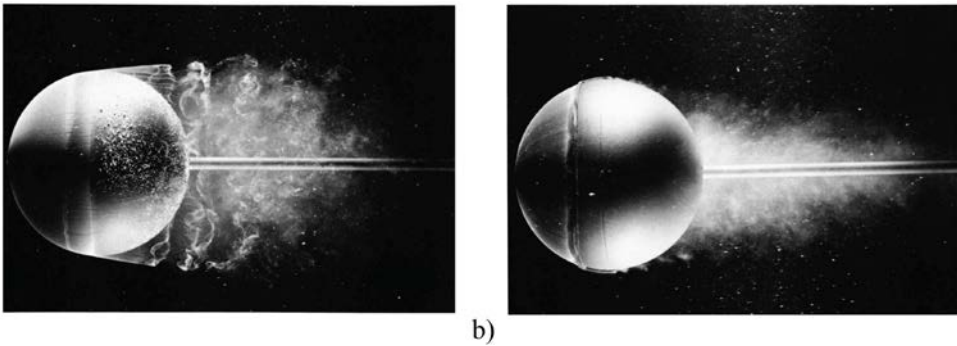


**Figure 2.3** Flow field past a sphere at  $Re_D = 15,000$  (a) and  $Re_D = 30,000$  with a trip wire (b). From van Dyke (1982).

More specifically, the streamwise location of the separation point is fixed in presence of geometrical discontinuities, such as sharp edges (Fig. 2.2). In the case of curved rear geometries (Fig. 2.3) on the other hand, it depends on the state of the separating boundary layer. This latter case applies for instance, to the wake behind spheres (Achenbach 1974) and circular cylinders (Williamson 1996).

Roshko (1955) compared the wake properties of bodies with the same frontal area, but different elongations with respect to the incoming flow and argued that the *bluffer* ones, viz. the less elongated ones, tend to produce a larger wake and thus, to experience a larger base drag contribution. Calvert (1967) further compared the wake properties of a variety of geometries, including a circular disk, a slender cylinder and cones with different vertex angles. The author found that the bubble length, i.e. the extension of the recirculation region, as well as the backflow intensity, increases with the vertex angle up to the limit case of the circular disk, with the lowest values being observed for the slender cylinder case (Fig. 2.4). The influence of the rear geometry of the body on the near-wake development has been widely investigated, especially for its relevance to the design of flow control strategies. Typical axisymmetric configurations of interest are unguided missiles and space launchers, in which case the separated flow physically surrounds the propulsive system. In this case the boattailing of the

trailing edge represents a common flow control approach. In particular, a boattailing angle of  $5^\circ$  is shown to reduce the base drag of a ballistic missile by 20% in the supersonic regime (cf. Herrin and Dutton 1994).

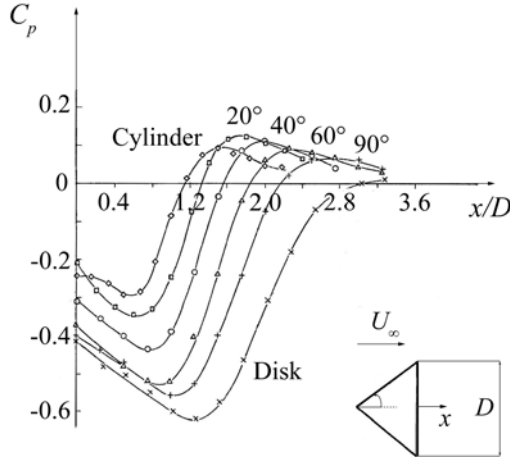


**Figure 2.4** Longitudinal variation of the pressure coefficient behind a cone for increasing vertex angles.  $Re_D = 50,000$ . Adapted from Calvert (1967).

Truncated cylinder geometries equipped with a rear-protrusion of smaller diameter, also called *afterbody*, are typically investigated in the transonic regime as a simple model for the base flow of a space launcher vehicle. The extension of the afterbody with respect to the main body diameter, viz. the ratio  $L/D$ , is shown to be critical for the separated flow development. In particular, the experimental results of Dépres *et al* (2004) showed that variations in this parameter can either induce impingement of the shear layer on the afterbody or downstream of its tip, with major differences on the unsteady flow behavior.

Further data obtained by Wolf *et al* (2012) in the subsonic regime indicate that the addition of an afterbody to the base can reduce the reattachment length by about 10% (Fig. 2.5).

With regards to the behavior of separating and reattaching shear layers, useful information can be retrieved by investigating the large amount of data available for planar *backward facing step* (BFS) flows. In view of their main features, i.e. the separation at the trailing edge, the development of a free shear layer and of an inner recirculation region, these flows are often treated as the two-dimensional homologous of afterbody flows (cf. Scharnowski and Kähler 2015).

The reattachment behavior of the BFS flow has been thoroughly characterized, among others by Le *et al* (1997) and Jovic and Driver (1994). The review by Eaton and Johnston (1981) showed that not only the step geometry, but also the inflow conditions influence the shear layer reattachment process. From this review it

emerged that increasing the boundary layer thickness promotes the reattachment and thus reduces the reattachment length. Interestingly, later parametric studies conducted by Hudy *et al* (2005) documented a completely opposite trend for the axisymmetric BFS. This seeming discrepancy between the planar and axisymmetric case is addressed in the present dissertation as an important point of discussion (cf. section 1.3).

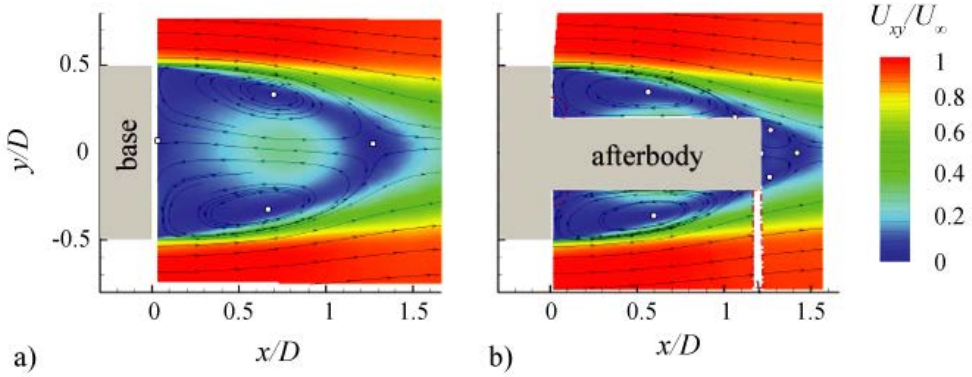


Figure 2.5 Near-wake velocity field behind a truncated base rocket model without (a) and with cylindrical afterbody (b).  $M_{\infty} = 0.2$ .  $Re_D \sim 10^5$ . Adapted from Wolf *et al* (2012).

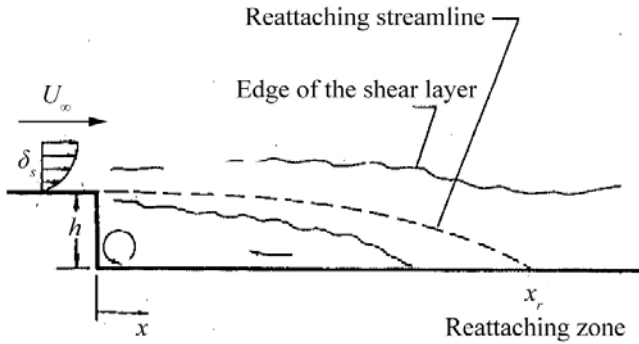


Figure 2.6 Turbulent flow separation and reattachment behind a two-dimensional BFS. Adapted from Eaton and Johnston (1981).

## 2.2 Base flow behavior

### 2.2.1 Separated flow dynamics

The shear layer developing in the near-wake flow represents an active interface, where important interactions occur between the separated flow and the outer



undisturbed flow. These interactions give rise to a distinctively unsteady flow field at high Reynolds numbers, e.g. those of interest to the present work and to most applications.

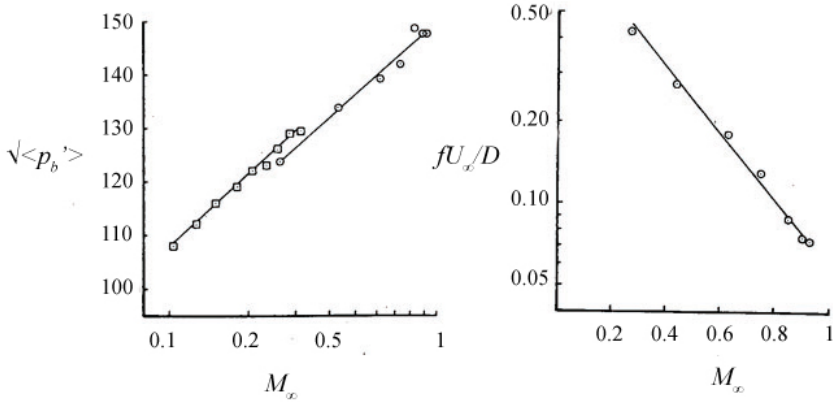


**Figure 2.7** Amplitude (a) and non-dimensional frequency (b) of the base pressure fluctuations behind a cylinder as a function of the freestream Mach number. Adapted from Merz (1979).

Merz *et al* (1978) and Merz (1979) previously conducted experiments on a cylinder geometry for a range of subsonic Mach numbers and showed that the presence of the recirculation region is associated with intense base pressure fluctuations, whose Strouhal number is observed to reduce with the Mach number (Fig. 2.7). This markedly unsteady behavior suggests that the foregoing discussion provides only an average picture of the near-wake topology. In fact, it was observed by Gerrard (1966) that the size of the near-wake region is instantaneously determined by the balance between the vortices rolling up in the shear layer and the outer fluid entrained in the recirculation region.

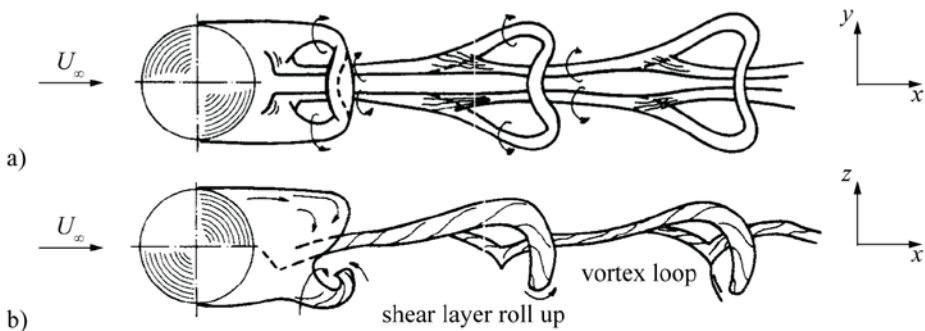


**Figure 2.8** Schematic representation of the vortex street formation in the wake of a sphere.  $Re = 10^3$ . Top view (a). Side view (b). Adapted from Achenbach (1974).

In particular, Gerrard found that with increasing flow speeds vortex loops start being shed off opposite sides of the body and with opposite sense of rotation. The

author argued that this process is initiated as soon as one side of the rolling-up shear layer grows strong enough to draw fluid from the diametrically opposite side and thus, stop its own growth (Fig. 2.8). Furthermore, he inferred that for  $Re_D = 10^3 - 10^5$  the vortices tend to be shed at a relatively constant frequency due to the conflicting effects of the increasing turbulent diffusion and entrainment.

### 2.2.2 Antisymmetric mode $m = 1$

The occurrence of vortex shedding has been reported for a variety of flow configurations, involving bodies of revolution (Calvert *et al* 1967; Achenbach 1974; Fuchs *et al* 1979) as well as prisms (van Oudheusden *et al* 2005), square-back bodies (Gohlke *et al* 2008) and planar BFS flows (cf. Scarano and Benocci 1999).

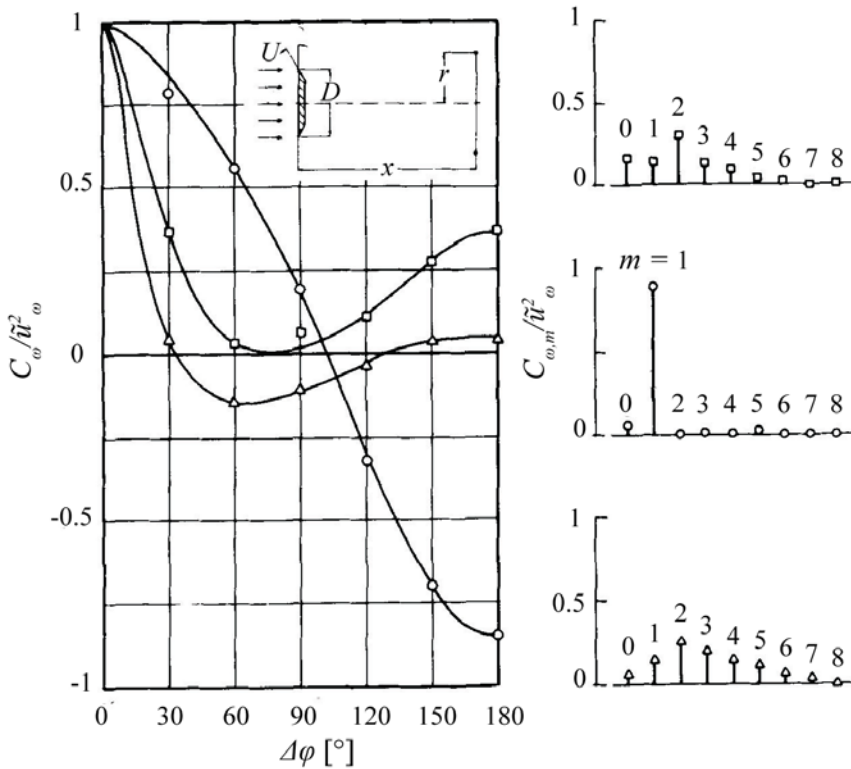


**Figure 2.9** Modal decomposition of streamwise velocity fluctuations in the wake of a disk. Circumferential correlation (a). Azimuthal modes (b).  $x = 3 D$  and  $r = 0.75 D$ .  $Re_D \sim 10^4$ . Adapted from Fuchs *et al* (1979).

Studies based on local and global stability analysis indicate that this phenomenon reflects a global instability of the shear layer and is associated with the occurrence of self-sustained oscillations of the near-wake flow (Oertel 1990; Huerre and Monkewitz 1985). The latter are referred to as *low-frequency* fluctuations in that their characteristic

frequency is typically identified with a Strouhal number  $St_D \sim 10^{-1}$ . While the specific base geometry appears to have only marginal influence on this characteristic frequency, instead the symmetry of the body has a strong impact on the spatial distribution of the shedding fluctuations.

In fact, the correlation analysis conducted by Achenbach (1974) on the sphere wake and the later modal analysis conducted by Fuchs *et al* (1979) on the circular disk wake, clearly showed that for an axisymmetric body, the vortices are shed as a pair of counter-rotating helices. This peculiar pattern is reflected in the occurrence of anti-symmetric wake fluctuations. Fuchs *et al* (1979) identified them with a dominant fluctuating mode with azimuthal wave-number  $m = 1$ , therefore referred to as a *helical* mode (Fig. 2.9).

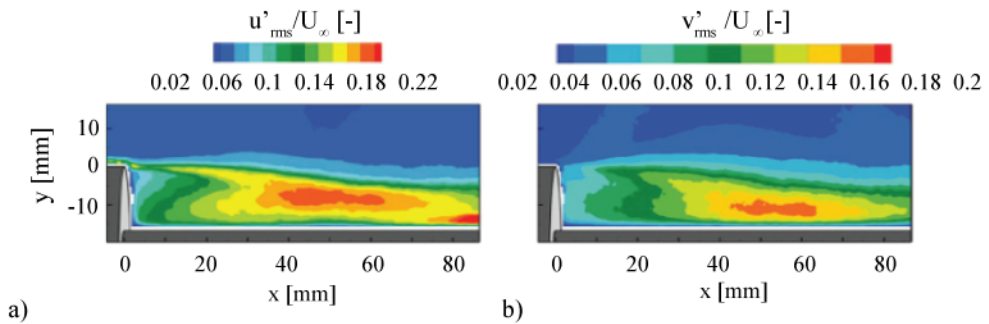


**Figure 2.10** Streamwise distribution of the turbulent fluctuations over an afterbody geometry. Color coded the RMS of the longitudinal (a) and vertical (b) velocity fluctuations.  $M_{\infty} = 0.702$ .  $Re_D \sim 10^6$ . Adapted from Schrijer *et al* (2014).

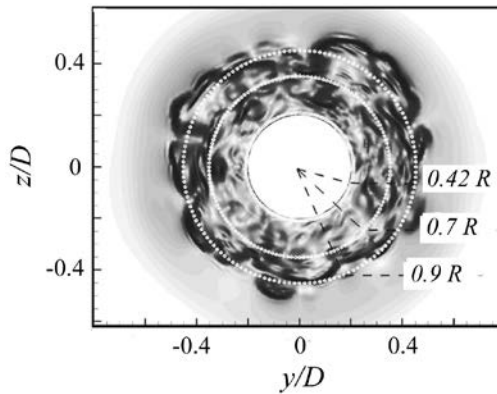


**Figure 2.11** Instantaneous Schlieren in the azimuthal-radial plane of an afterbody configuration.  $x_r = 0.67 / L_r$ .  $M_{\infty} = 0.702$ .  $Re_D \sim 10^6$ . Adapted from Deck and Thorigny (2007).

The unsteady side-loads induced by this mode are of major concern in engineering applications, particularly for transportation systems such as road vehicles or space

launchers. In the latter case for instance, the side loads associated with the helical mode can trigger transonic buffeting of the nozzle protruding from the first stage.

With regards to this specific problem, the fluctuations associated with the helical mode have been thoroughly characterized in the subsonic, transonic and supersonic regime by means of wall unsteady pressure measurements (cf. Dépres *et al* 2004; Hannemann *et al* 2011), two-component high-speed PIV (cf. Schrijer *et al* 2011; Schrijer *et al* 2014) and ZDES simulations (cf. Deck and Thorigny 2007; Pain *et al* 2014). The data available in the longitudinal plane of the wake show that the vortex shedding fluctuations intensify downstream of separation reflecting the growth of the structures within the shear layer (Fig. 2.10).

Cross-correlation analysis of velocity and pressure data in the azimuthal-radial plane gives further evidence of the interactions of the vortices along the azimuth (Fig. 2.11). Numerous studies conducted in the framework of active and passive wake control, e.g. by base bleeding or jets (Sanmiguel-Rojas *et al* 2009; Weiss and Deck 2011; Oxlade *et al* 2015) and by alterations of the base geometry respectively, indicate that interfering with the growth of the shear layer structures can substantially alter the wake dynamics. In the experiments of Dépres *et al* (2004) for instance, it is shown that the presence of a central protrusion, e.g. the propulsive nozzle, can strongly interfere with the growth of the vortices, influencing both the near-wake topology and fluctuating field (Fig. 2.12).

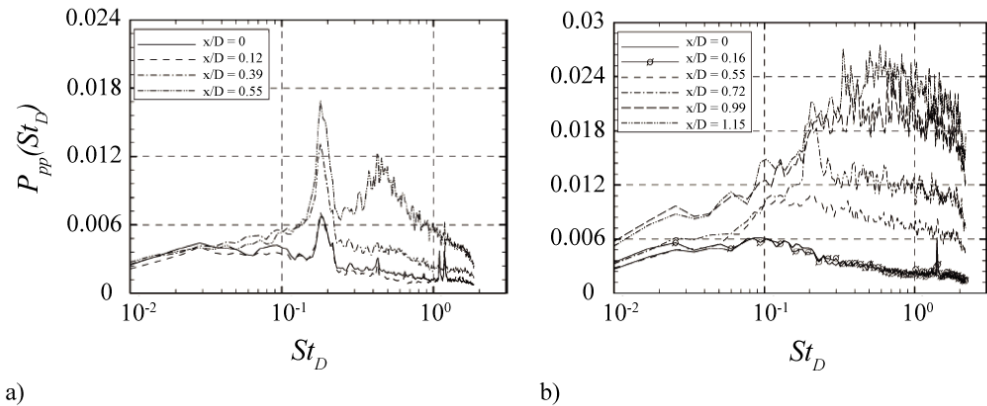


**Figure 2.12** Fluctuating pressure spectra on the wall of an afterbody at transonic speed.  $L/D = 0.6$  (a),  $L/D = 1.2$  (b).  $M_\infty = 0.702$ .  $Re_D \sim 10^6$ . Adapted from Dépres *et al* (2004).

### 2.2.3 Very-low-frequency backflow unsteadiness

Due to its practical relevance, the helical mode  $m = 1$  has been thoroughly investigated over the past years. However, the most recent investigations on the topic of turbulent axisymmetric wake flows focus on a further unsteady mechanism.

In particular, Rigas *et al* (2014) tracked the azimuthal-radial position of the center of pressure on the base of an ogive-cylinder model (Fig. 2.13) and could infer a continuous backflow precession about the symmetry axis of the body. Through modal decomposition and spectral analysis the authors showed that such an instability induces large-scale anti-symmetric fluctuations, similar to those caused by the vortex shedding, but occurring at frequencies in the order of  $St_D \sim 10^{-3}$ . These fluctuations were identified by the authors as being caused by the helical mode  $m = 1$  and linked to a *very-low-frequency* reorientation of the symmetry plane of vortex shedding (Fig. 2.13b).

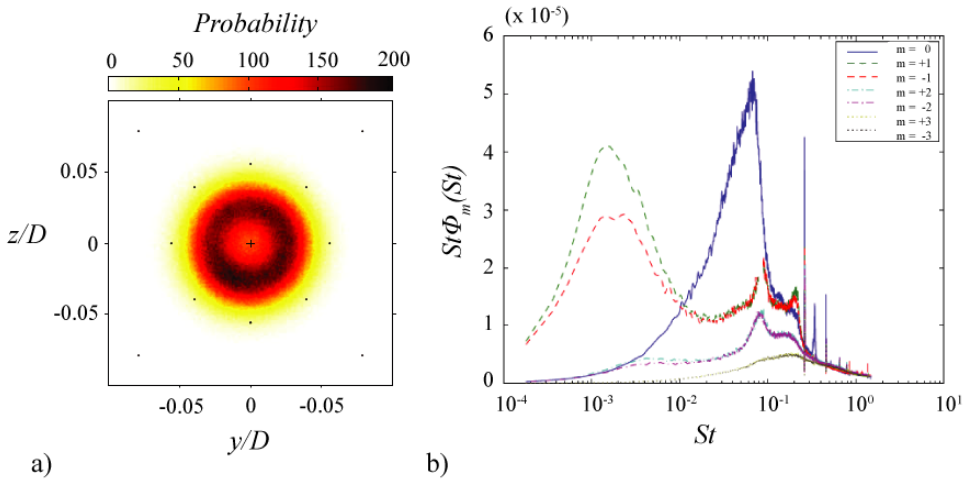


**Figure 2.13 Base pressure of a blunt-based cylinder. Two-dimensional probability distribution of the base pressure center (a). Spectra of the azimuthal modes of fluctuations.  $Re_D \sim 10^5$ . Adapted from Rigas *et al* (2014).**

Previous stereoscopic PIV experiments performed by Vanierschot and Van den Bulck (2011) showed that an analogous long-term instability also features the turbulent wake of an annular jet flow, by inducing a precession of the stagnation point at a characteristic frequency of  $St_D = 0.0025$ , based on the jet hydraulic diameter (Fig. 2.14).

Later experiments by Grandemange *et al* (2014) confirmed the occurrence of this backflow precession in the case of a sphere (Fig. 2.15). The authors had previously identified this unsteady mechanism in the wake of an ogive-cylinder geometry (Grandemange *et al* 2012a). However, due to the orientation of the measurement plane they interpreted it as a random switch between two asymmetric and seemingly equivalent wake topologies, rather than a consistent azimuthal motion. Furthermore, they showed that the boundary conditions, namely the symmetry of the mounting system and of the inflow conditions, strongly affect the orientation of the instantaneous backflow topology.

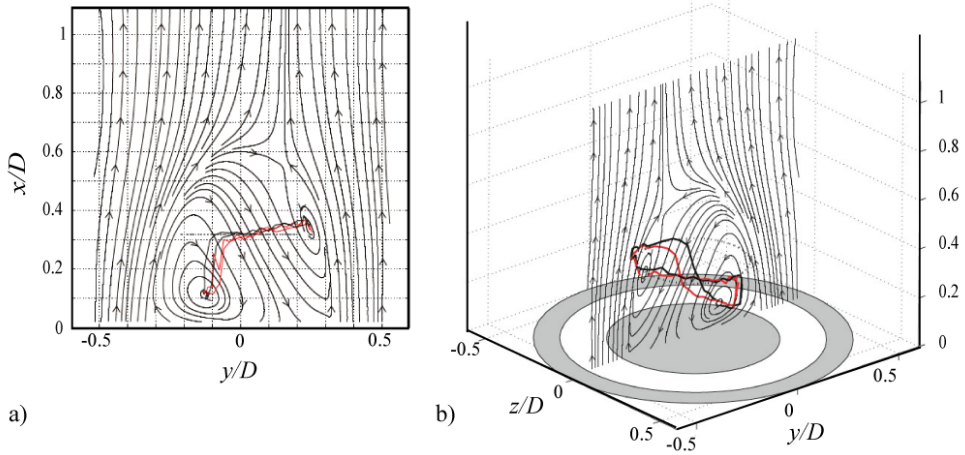


**Figure 2.14** Trace of the instantaneous motion of the stagnation point in the wake of an annular jet. Tri-dimensional view (a). Side-view (b).  $Re_D = 12,600$ . Adapted from Vanierschot and Van den Bulck (2011).

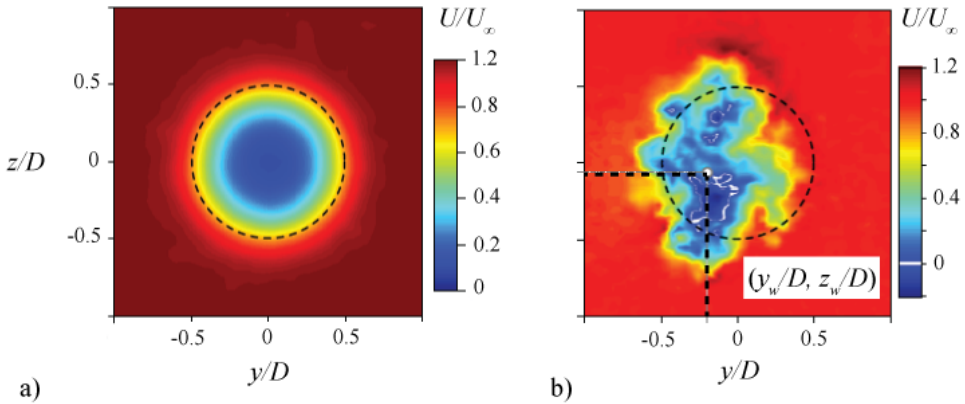


**Figure 2.15** Out-of-plane velocity field in the wake of a sphere. Time-averaged velocity contours (a). Instantaneous velocity contours (b).  $x = 0.93 D$ .  $Re_D = 19,000$ . Adapted from Grandemange *et al* (2014).

An analogous unsteadiness has been reported by the same authors occurring in the case of the Ahmed body geometry, with comparable characteristic frequencies (Grandemange *et al* 2012b). In the latter case the instability manifests as a switch between two mirrored asymmetric wake topologies and is ascribed to a *bistable* behavior of the backflow region.

The occurrence of a very-low-frequency reversed flow meandering reveals an inherent instability of the turbulent wake topology. In fact, the latter is found to evolve continuously over time, being always asymmetric. The above investigations

indicate that regardless of the specific base geometry, the wake is symmetric (or axisymmetric) only statistically, viz. as a result of a long-term equal exploration of different asymmetric topologies.

### 2.2.4 Base flow symmetry and experimental sensitivity

The identification of the very-low-frequency backflow unsteadiness essentially reveals that the axisymmetry of a turbulent wake is a merely statistical feature. In this respect, the long-term unsteadiness of the backflow region explains the pronounced turbulent base flow sensitivity, which was already documented in many experimental studies.

The occurrence of slight and unexpected asymmetries is frequently reported in the investigations dealing with turbulent near-wake flows (cf. Bourdon and Dutton 2008; Wolf *et al* 2012).

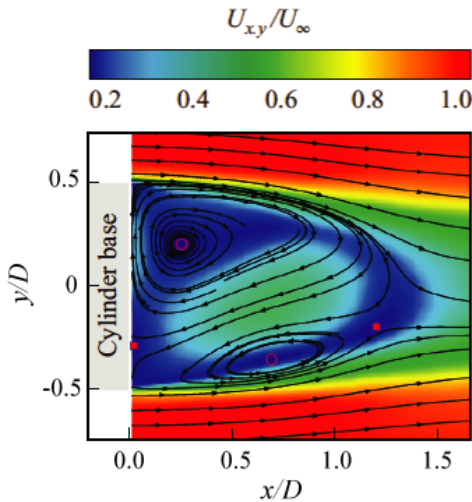


**Figure 2.16** Mean velocity color contours and streamlines past a truncated-base rocket model under a yaw angle of  $0.3^\circ$ .  $M_\infty = 0.2$ .  $Re_D \sim 10^5$ . Adapted from Wolf *et al* (2013).

Experimental sensitivity analyses conducted among others by Klei (2012) and Wolf *et al* (2013) show that the subsonic near-wake of a simple rocket model becomes asymmetric in presence of sideslip angles of the wind tunnel model with respect to the freestream flow as small as  $0.3^\circ$  (Fig. 2.16). Other studies pointed out that major asymmetries can be caused by the presence of the model support, which is found to introduce velocity defects in the order of 10% of the freestream velocity (Wolf *et al* 2010) and even preferred azimuthal periodicities in the near-wake flow (Grandemange *et al* 2012a).

While past researchers attributed such asymmetries exclusively to the accuracy of the experimental setup, the existence of a long-term instability poses a significant

constraint on the observation-time to adopt in the investigation of such flows. In particular, the latter should account for an equal exploration of all azimuths by the backflow region. As a result, the problem of the base flow sensitivity extends also to numerical investigations.

### 2.2.5 Bifurcations and symmetry breaking modes

The long-term variation of the turbulent wake topology is currently interpreted as a final chaotic state, which is attained by the wake after a series of transitions experienced from laminar to turbulent regime (Grandemange *et al* 2014; Rigas *et al* 2015). The latter are commonly referred to as *bifurcations* (Chomaz 2005) and reflect a global instability, which typically develops in axisymmetric wake flows for  $Re_D > 10^2$ . The occurrence of such bifurcations has been documented for a variety of geometries, ranging from spheres (Fabre *et al* 2008; Thompson *et al* 2001) and disks (Fabre *et al* 2008; Meliga *et al* 2009; Auguste *et al* 2010) to slender blunt-based bodies (Bohorquez *et al* 2011; Bury and Jardin 2012).

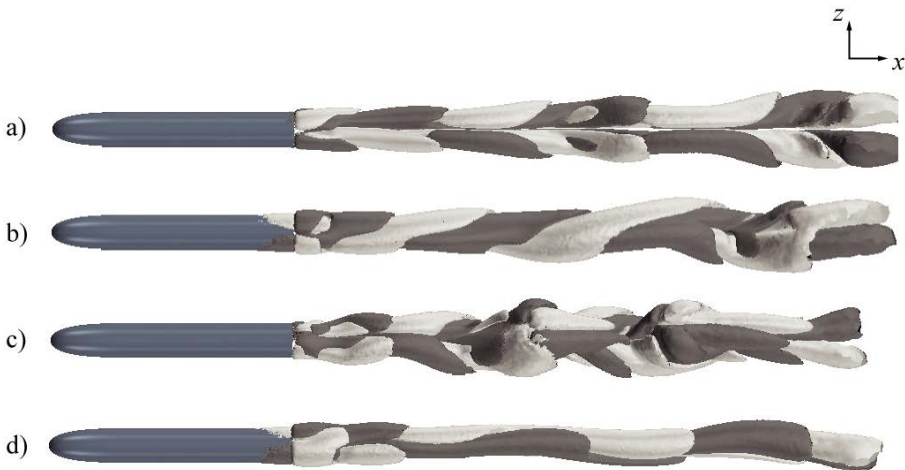


**Figure 2.17** Phases of the RSB mode past a truncated cylinder with elliptical nose. “Apparent” reflectional symmetry (a). Wake twisting (b). Reorientation of “apparent” reflectional symmetry (c). Wake stretching (d). Isosurfaces of streamwise vorticity  $\omega D/U_\infty = \pm 0.05$ .  $Re_D = 900$ . Adapted from Bury and Jardin (2012).

In the case of a slender cylinder with elliptical nose Bury and Jardin (2012) report of a first steady bifurcation at  $Re_D \sim 450$ , which identifies the transition from an axisymmetric wake topology with toroidal structure (*base flow*) to a streamwise oriented double-threaded wake. This second state is reflectionally symmetric with respect to a longitudinal and arbitrarily oriented plane and is referred to as *standing-wave* mode (SS). For  $Re_D = 600 - 800$  the authors identify a second bifurcation, corresponding to the appearance of an unsteady wake state. The latter is found to



feature a first phase of purely periodic shedding of thread vortices at a non-dimensional frequency  $St_D = 10^{-1}$  (*reflectional symmetry preserving*, RSP mode) and is followed by two subsequent phases of wake waving and twisting respectively, occurring with a characteristic non-dimensional frequency  $St_D \sim 10^{-2}$ . In the former studies of Brücker (2001) wake “modulations” with frequencies in the same order of magnitude were reported for both the sphere wake at  $Re_D = 500$  and the wake past a blunt-based cylinder with elliptical nose at  $Re_D = 700$ .

With further increasing the Reynolds number the studies of Bury and Jardin (2012) outline the appearance of broad-band fluctuations, reflecting the transition from the periodic and quasi-periodic states associated with the RSP mode to a fully chaotic state, denominated *reflectional symmetry breaking* (RSB) mode. The latter is shown to set in at  $Re_D = 900$  through a so-called *pitchfork* or *Hopf* bifurcation and features a markedly intermittent wake topology with alternating phases of “apparent” reflectional symmetry, wake twisting, reorientation of the “apparent” symmetry plane and stretching of the vorticity lobes (Fig. 2.17). For similar slender axisymmetric geometries at  $Re_D = 1000$  such intermittencies were also documented in the work of Scwarz *et al* (1994).

In the transition between the RSP and the RSB mode the wake topology becomes unsteady and recovers its planar reflectional symmetry only on average. The latter suggests a continuity with the very-low-frequency erratic azimuthal reorientations and associated statistical axisymmetry, which has been documented in the past few years for fully turbulent wake flows. In fact, these former results would promote the hypothesis that the long-term statistical symmetry of turbulent wake flows is reminiscent at turbulent regime of the RSB mode (Rigas *et al* 2014; Grandemange *et al* 2012, 2014).

Based on this hypothesis, Rigas *et al* (2015) recently proposed to model the turbulent wake dynamics by using a simply non-linear Langevin equation. Within such a model the wake dynamics is represented through a superposition of the first bifurcation leading to the SS mode, which is responsible for the loss of axial symmetry at laminar regime, with stochastic turbulent fluctuations. The latter stochastic model has been applied by the authors to the time-history of the center of pressure (CoP) on the base of a blunt-based slender axisymmetric body and proved successful in representing both the azimuthal meandering and the long-term saturation of the radial motion of the base pressure distribution (cf. Rigas *et al*, 2014). As such it has been adapted and applied to the present study case and will be discussed in chapter 6.

## **CHAPTER 3**

### **EXPERIMENTAL APPARATUS, MEASUREMENT TECHNIQUES AND DATA REDUCTION**

**Abstract** This chapter gives a description of the experimental apparatus and illustrates the main principles of the techniques used in the investigation. Details are provided of the wind tunnel facility and of the geometrical configurations used in the experiments. The working principles of PIV and stereoscopic PIV are illustrated. The main uncertainty contributions affecting the present results are discussed. The snapshot POD procedure adopted in the analysis of the wake large-scale fluctuations is outlined.

### 3.1 Experimental apparatus

#### 3.1.1 Flow facility

The data supporting the present work have been obtained in the low-speed open loop wind tunnel (W-Tunnel) operated within the Aerodynamics Laboratories of Delft University of Technology.



**Figure 3.1** Low-speed wind tunnel upstream of the test section and model installation.

The tunnel has a contraction ratio of 9:1 and features a square exit with  $0.4 \times 0.4 \text{ m}^2$  cross-section (see Fig. 3.1). The flow speed can be regulated by setting the revolutions of the centrifugal fan from 5 m/s up to a maximum of 35 m/s. In all the present experiments the tunnel was operated at a freestream velocity of 20 m/s in conditions of ambient pressure and temperature. The turbulence intensity of the tunnel in these conditions was measured to be approximately 0.5% (Michelis and Kotsonis 2014).

#### 3.1.2 Wind tunnel model

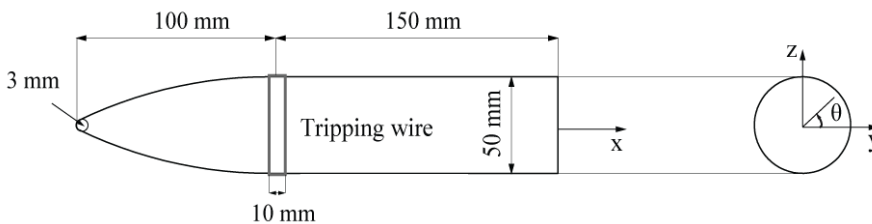


**Figure 3.2** Schematic side and end view of the wind tunnel model with dimensions and coordinate system.

The turbulent wake flow investigated in the present work was produced by an

Aluminum cylinder with blunt trailing edge featuring a spherically tangent ogival nose with 3 mm radius, ensuring smooth development of the boundary layer over the main body (Fig. 3.2). The aspect ratio of the model  $L/D$  was equal to 5, where  $L$  is the total length of the model and  $D$  is the base diameter. The nose section had a length of  $2D$ .

Transition of the boundary layer to turbulent regime was forced by means of a random distribution of carborundum particles with 0.8 mm mean diameter. This distribution was applied over a 10 mm wide adhesive patch, (Fig. 3.3) placed at the junction between the nose and the cylindrical main body.



**Figure 3.3 Carborundum roughness element.**

A flow stethoscope connected to a loudspeaker was used to verify the effectiveness of the transition device at the freestream speed hereby considered. The properties of the boundary layer were further quantified by means of dedicated PIV measurements carried out 5 mm upstream of the model trailing edge. The parameters characterizing the boundary layer prior to separation are provided in section 4.3 of the thesis.

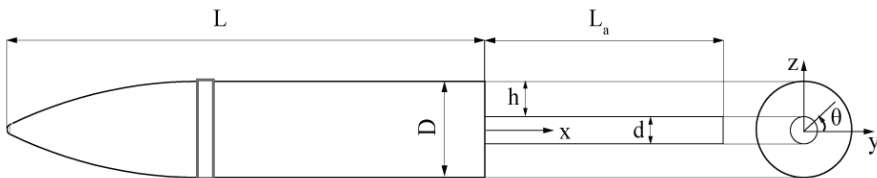


**Figure 3.4 Schematic side and end view of the wind tunnel model with afterbody with annotations and coordinate system.**

A cylindrical protrusion of smaller diameter  $d$ , herein often referred to as *afterbody* (Fig. 3.4), was added to the base of the model during the experiments addressing the influence of the base geometry on the near-wake flow behavior (cf. chapters 4 and 7). The extension of the afterbody with respect to the main body diameter was  $L_a/D = 2$  and was specifically designed to allow for reattachment of the separated shear layer on the afterbody according to Dépres *et al* (2004). Afterbodies of different diameters were

considered during the experiments, such to model axisymmetric BFS configurations with different step heights.

Additional data were acquired for a two-dimensional BFS flow configuration in order to establish a comparison between planar and axisymmetric flow reattachment behavior. The test configuration for these measurements was a 25 mm thick and 400 mm wide plate featuring an elliptical nose with 3:1 aspect ratio (Fig. 3.5).

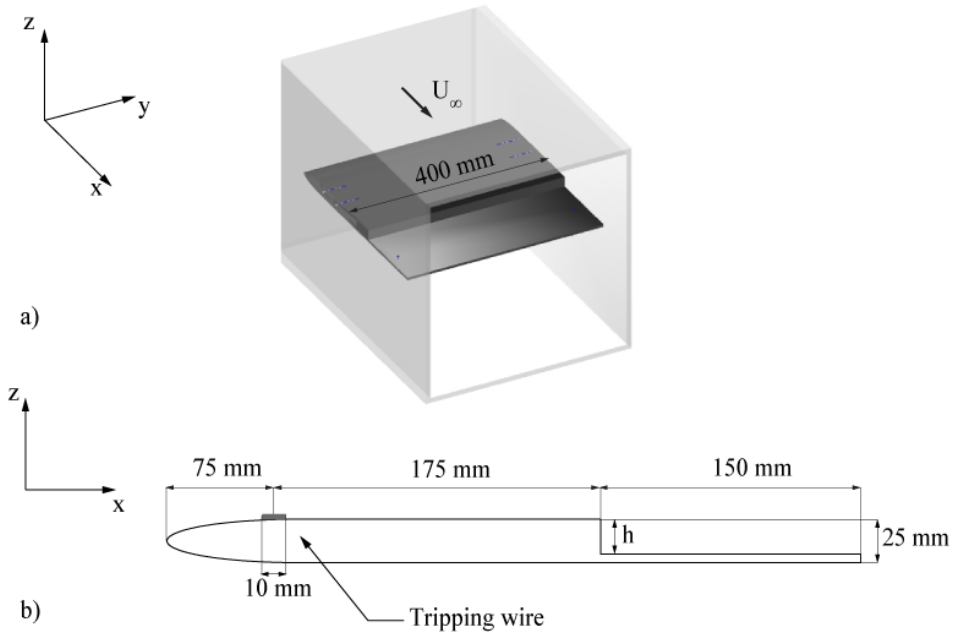


**Figure 3.5 Planar BFS model schematics with annotations and coordinate system. General view with Perspex test-section (a). Side view (b).**

The extension of the plate prior to separation ensured the same running length as in the axisymmetric model (cf. Fig. 3.4), whereas the extension of the step prevented downstream effects on the separated flow (Spazzini *et al* 2001). The step height could be varied by adding a plate on top of the extension of the step to match the non-dimensional step height values considered for the axisymmetric model.

The boundary layer was forced to the turbulent regime similarly to what was done for the axisymmetric model. The density of the roughness distribution ensured comparable conditions of the separating boundary layer in the planar and in the axisymmetric case. The latter was verified by means of PIV measurements performed upstream of the separation point (cf. chapter 4).

The two-dimensional model was installed in the side-walls of a Perspex elongation of the wind tunnel test section, whereas the axisymmetric model was held from the bottom by means of a 3 mm thick vertical Aluminum plate with sharp edges, which

allowed centering of the model with respect to the test-section (Fig. 3.6). The thickness of the vertical support was further reduced to 1.5 mm at the junction with the model to minimize the interferences with the boundary layer developing over the main body (Simpson 2001). The momentum deficit caused by the presence of the support plate was measured to be between 5% and 10% of the freestream velocity for streamwise stations between  $0.4 D$  and  $1.5 D$  downstream of the base.

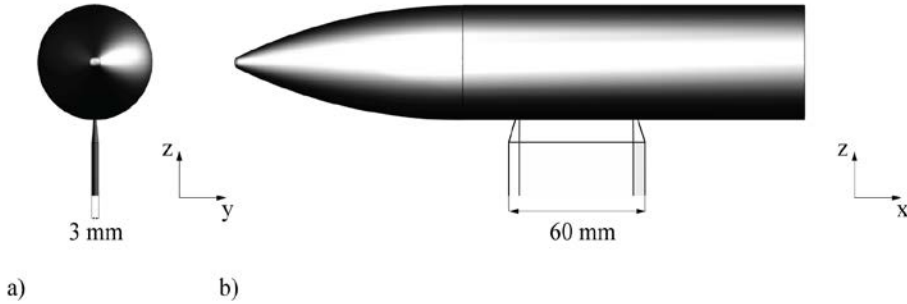


**Figure 3.6** Schematic views of the axisymmetric model with vertical support plate and coordinate system. Front view (a). Side view (b).

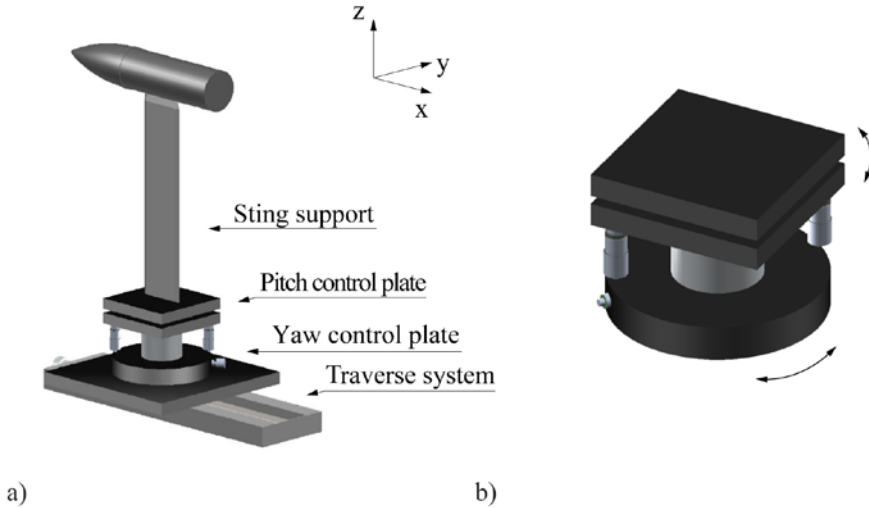


**Figure 3.7** Schematic of the wind tunnel model assembly (a). Yaw and pitch control plates (b).

Translation of the axisymmetric model in the streamwise direction was accomplished by means of a traverse system with 0.2 mm precision. The model was further installed on a support plate designed for fine tuning of pitch and yaw angles, with an accuracy of approximately  $0.1^\circ$  (Fig. 3.7). The precision on the pitch angle was improved to

0.05° in a later design of the support. A typical wind tunnel model setup for the present experiments is shown in Fig. 3.8.

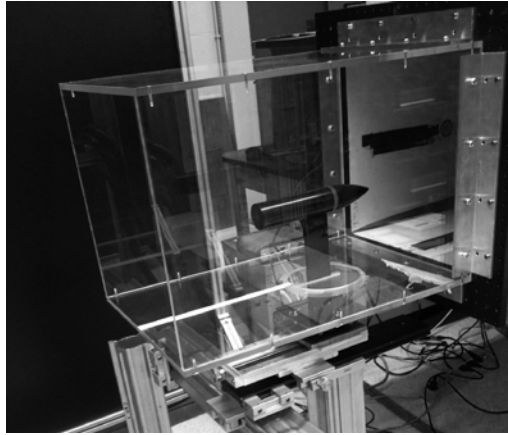


**Figure 3.8** View of the axisymmetric model (cf. Fig. 3.2) installed in a Perspex elongation of the wind tunnel test-section.

## **3.2 Particle Image Velocimetry**

### *3.2.1 Basic principles*

Particle Image Velocimetry (PIV) is a non-intrusive flow measurement technique, which allows both quantification of the velocity and flow visualization. Its working principle consists in measuring the displacement of small tracer particles carried by the flow over a short time-interval.

The measurements cover the flow field contained within a plane or a volume and do not require the use of probes. A typical PIV setup is schematically represented in Fig. 3.9. Particle tracers are injected in the flow and subsequently illuminated in a plane twice within a short time-interval using a pulsed light source (usually a laser). The light emitted by the laser is shaped into a thin light sheet by means of one or more optical elements. The position of the tracer particles is recorded in two subsequent exposures with a digital imaging device, such as a CCD camera, which is oriented perpendicular to the measurement plane. The digital images are subdivided into smaller areas, referred to as *interrogation windows*. For each of these areas a two-component velocity vector is determined by means of statistical operators using the values of particle displacement, pulse time-separation and image magnification.

Hereafter the main aspects of PIV are illustrated. For a comprehensive description of the technique the reader is referred to Raffel *et al* (2007) and Adrian and Westerweel (2011).

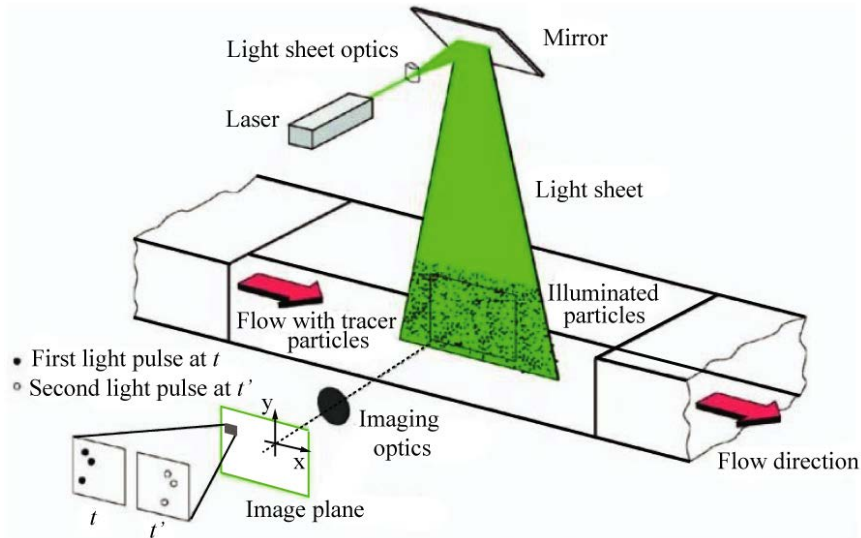


**Figure 3.9** Typical experimental arrangement for particle image velocimetry in a wind tunnel. Adapted from Raffel *et al* (2007).

### Flow seeding

In most applications the flow is seeded with tracer particles in concentrations between  $10^9$  to  $10^{12}$  particles/m<sup>3</sup>, depending on the spatial resolution.



**Figure 3.10** Safex fog generator.

The tracer particles are expected to accurately follow the air flow. A small velocity lag with respect to the fluid medium is referred to as *slip velocity*. Assuming spherical particles of diameter  $d_p$  moving with velocity  $U_p$  in a continuously accelerating fluid, the slip velocity is expressed as



$$U_s = d_p^2 \frac{(\rho_p - \rho)}{18\mu} \frac{dU_p}{dt} = \tau \frac{dU_p}{dt} \quad (3.1)$$

The parameter  $\tau$  in (3.1) is called *relaxation time* and it represents the particle response time to a sudden change in the fluid velocity (cf. Ragni *et al* 2010). Thus, it is often used to assess the fidelity of the flow tracers. For turbulent flows, where a large number of flow-scales is present, it is common to compare the particle relaxation time with the characteristic time-scale of the flow by means of the *Stokes number*

$$S_k = \frac{\tau_p}{\tau_{flow}} \quad (3.2)$$

In the current experiments the flow was seeded with micron sized droplets of glycol-water solution, which were uniformly dispersed in the flow by means of a SAFEX smoke generator (Fig. 3.10) at a typical concentration of 5 particles/mm<sup>3</sup>. For these particles, the Stokes number was estimated to be  $S_k \sim 0.01$ , based on the typical thickness of the separating boundary layer and the freestream velocity (cf. Table 4.3). This value is adequate for flow tracing with negligible errors due to particle slip (Samimy and Lele 1991).

Furthermore, tracer particles are chosen also based on their scattering efficiency. The latter should be as large as possible to ensure a good contrast with respect to the background and thus, facilitate the image evaluation process. Materials with an optimal combination of size, viz. diameter, and index of refraction relative to the fluid medium, viz.  $n/n_f$ , are typically sought for in order to maximize the scattering efficiency.

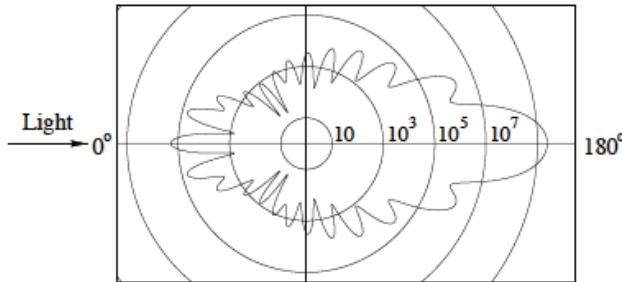


**Figure 3.11** Light scattering by a 1µm oil droplet in air. Raffel *et al* (2007).

The tracers typically used in PIV follow the *Mie scattering* theory. Thus, they scatter the light with maximum intensity in the forward direction and with significantly lower intensity to the side and in backward direction (Fig. 3.11). For those seeding materials the scattered light intensity features approximately  $q$  maxima over viewing angles between 0° and 180°,  $q > 1$  being the normalized diameter defined as

$$q = \pi \frac{d_p}{\lambda} \quad (3.3)$$

Ideally, the particle image intensity can be maximized by recording in the forward scattering direction. In practice however, the recordings are often conducted between the side and the backward scattering directions to cope with additional constraints related to the PIV technique. In the case of the present experiments for instance, the recordings were often performed in the side scattering direction such to limit the error on the out-of-plane component of the velocity.

### Illumination

Lasers are commonly employed in PIV applications, as they can provide pulsed, collimated monochromatic light, which can then be shaped into thin light sheets without chromatic aberration. This allows for illumination of the tracer particles twice in a finite time-interval  $\Delta t$ .

In the present experiments a high-speed laser was used for illumination in order to obtain time-resolved velocity data of the wake flow. In particular, a Quantronix Darwin Duo frequency-doubled Nd:YLF (Neodymium-doped Yttrium Lithium Fluoride) laser was used (Fig. 3.12), which allows for a measurement repetition rate between 1 and 10 kHz. This laser emits light with a wavelength  $\lambda = 532$  nm and with an energy per pulse  $E = 25$  mJ at 1 kHz and is characterized by a pulse duration, or *pulse width*,  $\delta t \sim 100$  ns. The time-interval between the two pulses  $\Delta t$  can be tuned based on the experimental conditions.



**Figure 3.12** Quantronix Darwin-Duo Laser. ([www.quantronix.com](http://www.quantronix.com)).

In the present measurements the laser beam was typically shaped in a 2 to 3 mm thick laser sheet. The pulse separation was set to approximately 20  $\mu$ s in order to keep the maximum out-of-plane particle displacement within approximately 1/3 of the laser sheet thickness in the case of cross-flow stereoscopic measurements

and within 1/4 of the final interrogation window size in the case of two-component PIV measurements (cf. Raffel *et al* 2007).

### Imaging

Spherical and cylindrical lenses are used to shape the laser beam in a sheet of few millimeters thickness (Fig. 3.13). The particles lying within this laser sheet are imaged on the surface of an image sensor with a magnification factor  $M$  defined as

$$M = \frac{d_i}{d_o} \quad (3.4)$$

wherein  $d_i$  and  $d_o$  represent the distance between the lens plane and the image plane, and the distance between the lens plane and the object plane identified with the laser sheet, respectively.

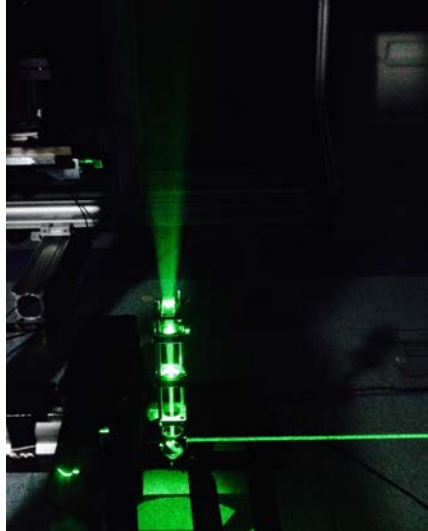


**Figure 3.13** Example of laser sheet formation by means of multiple lenses.

The imaged particle *geometrical diameter* associated with the image magnification can be estimated as

$$d_{geom} = M d_p \quad (3.5)$$

Additionally, due to diffraction effects each particle is imaged as a bright spot, called *Airy disc*, surrounded by rings of decreasing intensity. The finite diameter of this diffraction spot is called *diffraction diameter* and is defined as

$$d_{diff} = 2.44(1 + M)f_{\#}\lambda \quad (3.6)$$

This diameter depends on the wavelength of the incident light  $\lambda$ , on the image magnification  $M$  and furthermore, on the characteristics of the imaging system through the f- number  $f_{\#}$ , which is defined as

$$f_{\#} = \frac{f}{D_a} \quad (3.7)$$

wherein  $f$  and  $D_a$  in (3.7) are the lens focal length and aperture diameter respectively.

If the lens is sufficiently thin compared to its focal length, the following *thin lens equation* holds

$$\frac{1}{f} = \frac{1}{d_i} + \frac{1}{d_o} \quad (3.8)$$

The resulting imaged particle diameter can be thus estimated from (3.5) and (3.6) as follows

$$d_{\tau} = \sqrt{d^2_{geom} + d^2_{diff}} \quad (3.9)$$

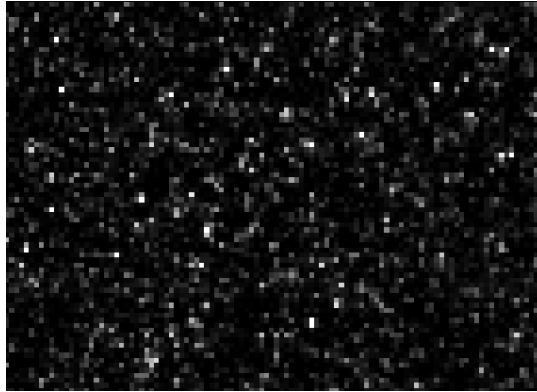


**Figure 3.14** 1  $\mu\text{m}$  particles recorded with a CMOS camera (Photron FastCAM SA1.1 CMOS, pixel pitch 20  $\mu\text{m}$ ).

In the current experimental conditions ( $d_p = 1 \mu\text{m}$ ,  $\lambda = 532 \text{ nm}$ , magnification factor  $M \sim 0.16$ ,  $f_{\#} = 5.6$ )  $d_{\tau} \sim 9 \mu\text{m}$ , which is approximately equal to the diffraction diameter. However, this value is still smaller than the pixel pitch of the sensors used in the experiments. In such conditions the imaged particle diameter is considered to be governed by the sensor pixel size.

Sharp particle images of small diameter ensure an adequate contrast with respect to the dark background (Fig. 3.14). In practice, given a certain light source and image

magnification the lens f- number is tuned so that all particles in the laser sheet are imaged in focus within the *depth of field*  $\delta z$

$$\delta z = 4.88 f_{\#}^2 \lambda \left( \frac{1 + M}{M} \right)^2 \quad (3.10)$$

A slight defocusing is often applied to ensure that the diameter of each imaged particle spans over approximately two to three pixels in order to avoid under-sampling issues due to *peak-locking* (Westerweel 1997).

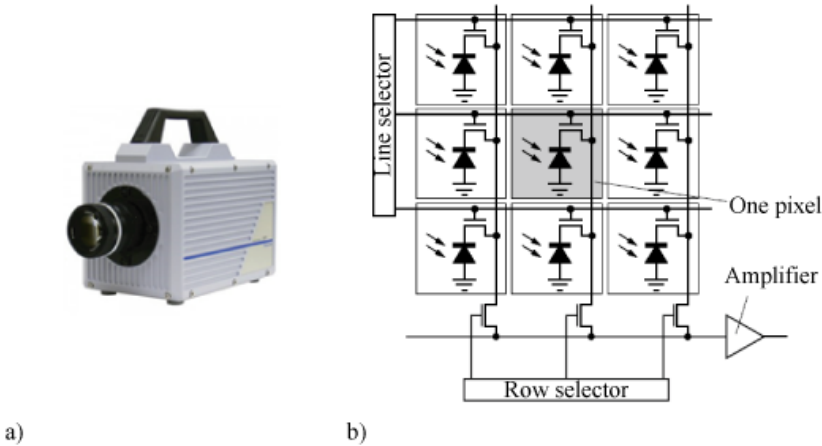


**Figure 3.15** High-speed Photron FASTCAM SA 1.1 camera (a), from [www.photron.com](http://www.photron.com). Schematics of a CMOS sensor (b), from Raffel *et al* (2007).

### Recording

The high-speed PIV recordings for the present experiments were performed by Photron FastCAM SA1.1 CMOS (Fig. 3.15a) operated at acquisition frequency between 50 Hz and 2 kHz. The architecture of these cameras feature an array of 1024 x 1024 pixels, with 20  $\mu\text{m}$  pixel size, whereby each pixel of the sensor collects the incident light (i.e. photons) in the form of electric charge (i.e. electrons) and converts it into a voltage by means of a dedicated amplifier (Fig. 3.15b).

### Synchronization

The particles illuminated during the two subsequent light pulses are imaged on the camera sensor during two distinct exposures and recorded as double-frame snapshots. This process requires the synchronization between the camera exposure and the light pulse. The timing diagram for the double-frame recordings performed in the present experiments is presented in Fig. 3.16.

In this acquisition mode the laser delivers two pulses, each of duration  $\delta t$ , separated by a time-interval  $\Delta t$ . The light scattered by the particles during each of the two pulses is

captured by the camera within two separate exposures, yielding double-frame recordings. The time-spacing between the double-frame recordings  $\Delta T$  depends on the hardware, viz. laser and camera, whereas the laser pulse-separation  $\Delta t$  is adjusted based on the experimental conditions (see preceding sections for details).

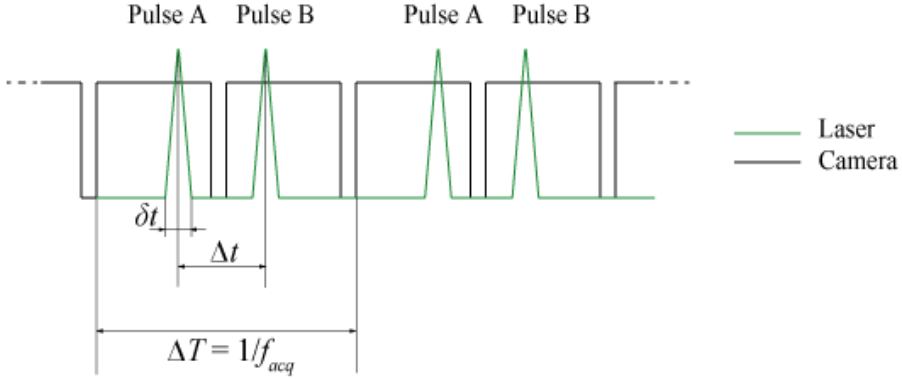


Figure 3.16 Timing diagram for a PIV double-frame recording.

### Image interrogation

The PIV recordings, or *snapshots*, are subdivided into smaller interrogation areas, or *windows*, and digitally evaluated. Fig. 3.17 schematically illustrates the cross-correlation procedure used in the evaluation of the PIV recordings. In particular, the intensity maps obtained for the two frames at integer pixel locations,  $I(i, j, t)$  and  $I'(i, j, t + \Delta t)$  respectively, are shifted one over the other by a finite amount  $(\delta x, \delta y)$ . The products of the intensity distributions are then summed up over the entire window size as follows

$$C(\delta x, \delta y) = \sum_{m=1}^M \sum_{n=1}^N [I(i, j) - \bar{I}] \cdot [I'(i + \delta x, j + \delta y) - \bar{I}'] \quad (3.11)$$

wherein  $M$  and  $N$  represent the number of pixels in the horizontal and vertical direction respectively.

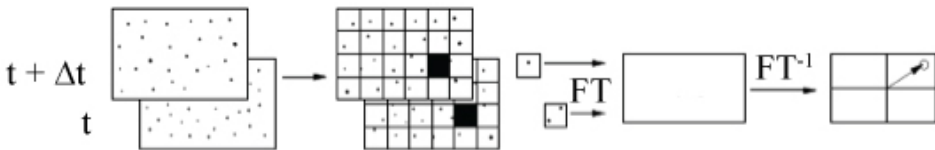


Figure 3.17 Schematics of typical digital PIV image analysis. Adapted from Raffel *et al* (2007).

The above operations provide the particle displacements approximated at the closest pixel shift, which are identified by the maxima in the cross-correlation maps. Further interpolating around these maxima yields the displacement value with subpixel accuracy. For this purpose a Gaussian peak fit is commonly used (cf. Raffel *et al* 2007).

The displacement resulting from this interpolation is then divided by the light pulse separation and multiplied by the image spatial resolution to obtain the velocity vector. The ratio between the two highest peaks in the cross-correlation map is called *signal-to-noise ratio* (SNR) and indicates the reliability of the cross-correlation result.

### Image pre-processing and data validation

In order to improve the result of the PIV image evaluation, especially in presence of background intensity or light reflections from solid surfaces, the PIV images are pre-processed prior to the interrogation phase. Typical pre-processing procedures consist in the subtraction of the minimum intensity of each pixel along the recording sequence, or in the normalization with respect to the average value along the sequence (Adrian and Westerweel 2011).

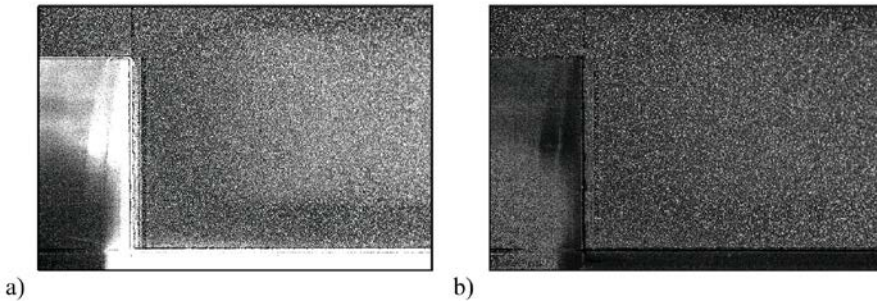


**Figure 3.18 Comparison of PIV images: before (a) and after (b) pre-processing.**

The latter procedure was adopted in the current experiments. Fig. 3.18 shows a PIV snapshot affected by light reflections at the wall and background intensity. The pre-processed image obtained from the normalization procedure eliminates most unwanted light reflections.

Even when pre-processing, the possible presence of residual light reflections or conditions of scarce illumination in some areas of the image, can lead to the computation of erroneous vectors during the interrogation phase. To avoid including unphysical data, these vectors, which are referred to as *outliers*, are detected and removed from the vector field by means of dedicated post-processing algorithms. The post-processing of the present measurements was accomplished using a median filter based on the universal outlier detection algorithm (Westerweel and Scarano 2005), which was applied up to three times to the vector fields.

### 3.2.2 Stereoscopic PIV

#### Basic principles

Recording the particle images with one camera perpendicular to the measurement plane only allows for measuring the projection of the actual flow velocity in the laser sheet plane, hereafter referred to as *object plane*.

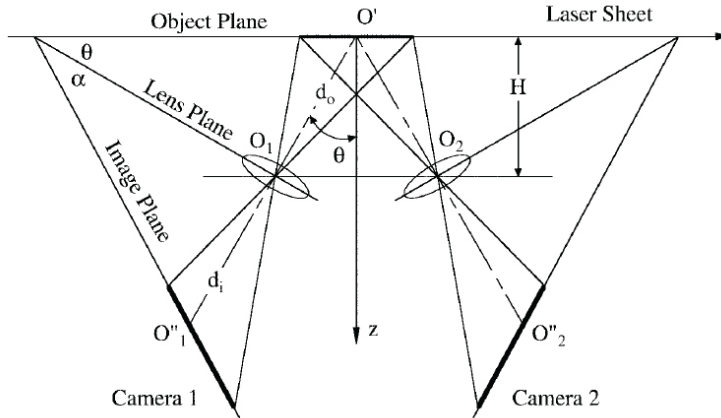


**Figure 3.19 Stereoscopic imaging configuration based on angular lens displacement with Scheimpflug condition. Prasad (2000).**

The perspective error affecting this measurement increases with increasing deviations of the camera from the normal to the laser sheet plane. This contribution could be significant in presence of large out-of-plane velocity components, which case applies to the wake flow currently investigated.

The most straightforward way of obtaining the out-of-plane velocity component from a planar PIV measurement consists of imaging the same FOV from two different viewing angles, similar to the binocular vision of the human eye. This technique is known as stereoscopic PIV and is typically implemented with two-cameras arranged in the so-called *angular displacement* imaging configuration (Fig. 3.19). Within this approach the cameras are rotated away from the normal to the laser sheet plane so that their lines of sight intersect the object plane at the system axis.

In order for the particles to be imaged in focus, image, lens and object plane must intersect on a single line (Prasad 2000). The latter is known as *Scheimpflug condition* and can be accomplished by tilting the lens objective towards the object plane by means of dedicated adapters (Fig. 3.20). The two oppositely distorted views are interpolated onto a common grid. To facilitate the interpolation it is usual to maximize the overlap between the two views. The out-of-plane component of the velocity can then be computed according to Raffel *et al* (2007).



$$W = \frac{U_1 - U_2}{\tan\theta_{x1} + \tan\theta_{x2}} = \frac{V_1 - V_2}{\tan\theta_{y1} + \tan\theta_{y2}} \quad (3.12)$$

wherein  $U$  and  $V$  represent the in-plane components of the velocity, while  $\theta_{x1}$ ,  $\theta_{x2}$  and  $\theta_{y1}$ ,  $\theta_{y2}$  are the angular deviations of the two cameras from the  $x$  and  $y$  axis respectively.



**Figure 3.20** Scheimpflug adapter mounted on a 105 mm Nikkor objective.

In general, the error on the out-of-plane component of the velocity decreases by increasing the viewing angle of the camera between 0 and 45° (Prasad 2000). However, additional constraints related for instance, to the optical access and to the depth of field, often limit the viewing angles to lower values, i.e. in the order of 30° for the present experiments.

### Image calibration and reconstruction

The image-pairs obtained from the two stereoscopic views are interrogated separately yielding displacement data on two distinct Cartesian grids. The latter are then mapped to the object plane, also called *world* plane, and further combined to give the three-dimensional velocity field. These operations comprise the process of *image reconstruction*, which is usually based on a calibration of the imaging system. This procedure requires the acquisition at different  $z$ -positions of one or more images of a calibration target, which is aligned with the measurement plane. The latter is provided with a precise and evenly spaced Cartesian grid of markers in order to identify the positions in the object plane. Precisely machined two-level plates featuring dotted markers of known spacing and number (Fig. 3.21) represent a standard choice for stereoscopic PIV experiments.



Figure 3.21 Lavisision Type 11 two-level calibration target with dotted grid ([www.lavisision.com](http://www.lavisision.com)).

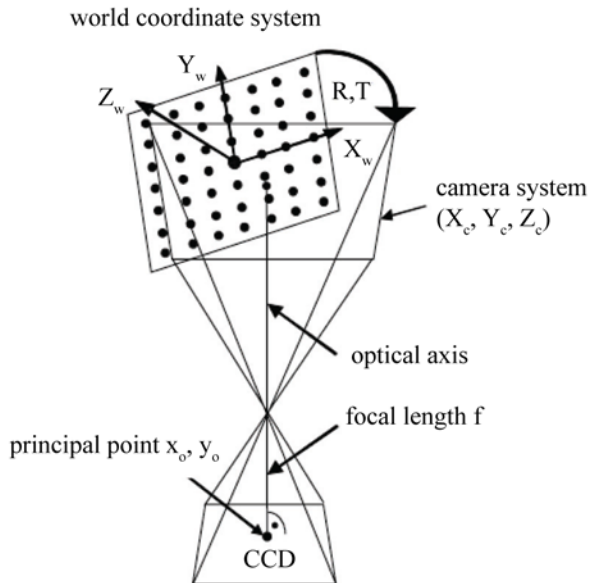
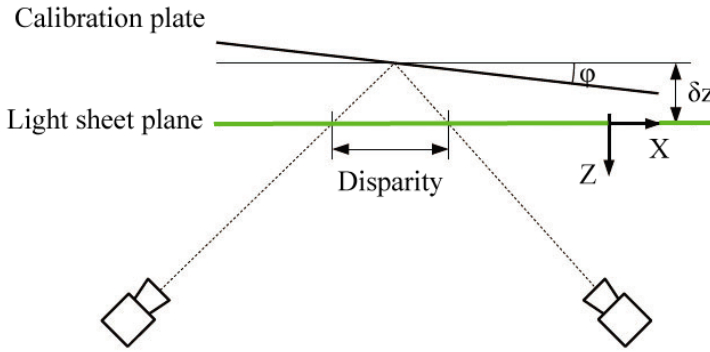


Figure 3.22 Schematic illustration of the camera pinhole model. Adapted from Wieneke (2005).

A common way of obtaining the mapping functions for the two stereoscopic views is based on a so-called *camera pinhole* model, schematically illustrated in Fig. 3.22. This model is based on the assumption that all rays going from the particles in the object plane to the image plane pass through a single point in space. From this kind of model the viewing angles at each point of the sensor can be retrieved with precisions in the order of  $0.1^\circ$ . Alternatively, the mapping functions can be obtained using a least-square third-order polynomial fit between the known markers positions on the calibration target and those recorded in the image plane (Soloff *et al* 1997).

The reliability of the calibration procedure strongly depends on the alignment of the calibration target with respect to the measurement plane identified by the laser sheet. In practice, misalignments are always present between the two (see Fig. 3.23). Therefore, a self-calibration procedure is usually applied to the PIV recordings (Wieneke 2005).

The latter consists in dewarping the instantaneous particle pattern from the two cameras at the laser sheet location ( $z = 0$ ) and cross-correlating them in order to obtain a so-called *disparity* map. This disparity map provides information on the misalignment of the calibration target with respect to the laser sheet plane and is used to improve the original calibration.



**Figure 3.23** Schematics of typical misalignment between calibration target and light sheet plane. Adapted from Raffel *et al* (2007).

### 3.3 Experimental uncertainty

Hereafter the main uncertainty contributions affecting the experimental data are evaluated in order to assess the accuracy of the present results. The discussion mainly deals with the evaluation of the uncertainty associated with the present flow facility and wind tunnel models, with the use of the PIV measurement technique, notably the digital image cross-correlation, and lastly with the size of the data ensembles used in the statistical evaluation of the flow properties.

#### Flow facility

This uncertainty contribution mainly affects the estimate of the freestream flow velocity set during the experiments. The latter was tuned using a digital barometer with a 0.03% of reading accuracy and thus, represents the uncertainty on the value of the freestream velocity  $U_\infty$  and on the diameter-based Reynolds number  $Re_D$ . These errors are considered negligible in the context of the present work.

### Wind-tunnel model

The alignment of the wind tunnel model with respect to the freestream flow is crucial in the analysis of the long-term turbulent wake dynamics. Thus, it is worthwhile estimating the uncertainty associated with the model angular positioning. The latter was evaluated by inspecting the long-time averaged position of the backflow centroid obtained from the stereoscopic PIV measurements or alternatively, the vertical position of the wake stagnation point on the base retrieved from the two-component PIV data. The sensitivity of the model with respect to angular misalignments was found to be of approximately  $0.5 D$  (i.e. 25 mm) per degree (cf. chapter 6).

The model was considered correctly aligned when the deviation of such points from the geometrical wake center was within  $0.025 D$  (i.e. 1.25 mm). This value corresponds to approximately 0.3 to 0.4 of the final interrogation window size used in the present measurements. The pitch and yaw angle of the model could be tuned with an accuracy of  $0.05^\circ$  and  $0.1^\circ$  respectively (cf. section 3.1.2). Both angles could be measured with a  $0.1^\circ$  precision.

### PIV uncertainty

Assuming a linear propagation of the error, the uncertainty on the measured velocity can be expressed as a function of the uncertainty affecting the measurement of the particle displacement  $\epsilon_{\Delta s}$  and the estimate of the time-interval  $\epsilon_{\Delta t}$  as follows

$$\epsilon_u = \sqrt{\left(\epsilon_{\Delta s} \frac{\partial u}{\partial \Delta s}\right)^2 + \left(\epsilon_{\Delta t} \frac{\partial u}{\partial \Delta t}\right)^2} \quad (3.13)$$

wherein  $\frac{\partial u}{\partial \Delta s}$  and  $\frac{\partial u}{\partial \Delta t}$  account for the influence of the individual uncertainties on the experimental results and are referred to as *sensitivity coefficients*.

In particular, the uncertainty on the pulse separation is identified with the pulse width  $\delta t$ . The latter is in the order of 100 ns and therefore is considered negligible in comparison with the pulse-separation  $\Delta t$ , which is in the order of tens of microseconds. The uncertainty on the displacement is attributed to the use of image correlation algorithms and is estimated to be as much as 0.1 pixels for planar measurements (Raffel *et al* 2007). Taken this into account, the uncertainty on the instantaneous velocity can be estimated as

$$\epsilon_u = \frac{\epsilon_{corr}}{k\Delta t} \quad (3.14)$$

wherein  $k$  is the digital spatial resolution and is expressed in pixels/mm. For the present measurements this contribution was estimated as being approximately 1% of the freestream velocity.

Statistical uncertainty

The statistical properties of the flow field are evaluated based on a finite number of measurement samples, i.e. PIV snapshots in the present case. The latter unavoidably affects the evaluation of the statistics, even if the observation-time is carefully chosen to account for the characteristic time-scales of the flow. Using the definitions of Benedict and Gould (1996) for a data ensemble comprising  $N$  uncorrelated samples, the uncertainty on the evaluation of the first order statistics, viz. the mean flow velocity, is estimated as

$$\epsilon_{\bar{u}} = \frac{\langle u' \rangle}{\sqrt{N}} \tag{3.15}$$

wherein  $\langle u' \rangle$  is the RMS of the fluctuating velocity. Similarly, the uncertainty on the second order statistics, viz. the statistical velocity fluctuations, is estimated as

$$\epsilon_{u'} = \frac{\langle u' \rangle}{\sqrt{2N}} \tag{3.16}$$

As an example, the value of the out-of-plane statistical fluctuations for one of the present test cases is plotted as a function of the data ensemble size in Fig. 3.24 and indicates that the statistical convergence is attained for approximately  $N \geq 500$ .

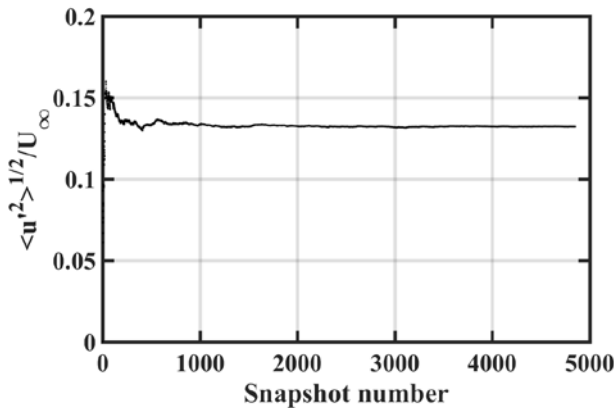


**Figure 3.24** RMS of the out-of-plane velocity fluctuations  $\langle u'^2 \rangle^{1/2}$  as a function of the data ensemble size.  $x = 0.3 D$ ,  $(z, y) = (0.1 D, 0.1 D)$ .  $Re_D = 67,000$ .

Lastly, the uncertainty on the Reynolds shear stress can be expressed as

$$\epsilon_{uv'} = \frac{\sqrt{1 + R_{uv}^2} \langle u' \rangle \langle v' \rangle}{\sqrt{N}} \quad (3.17)$$

wherein  $R_{uv}$  is a correlation coefficient defined as

$$R_{uv} = \frac{\overline{u'v'}}{\langle u' \rangle \langle v' \rangle} \quad (3.18)$$

From the above definitions it follows that the accuracy in the evaluation of the statistical properties tends to be lower in presence of high fluctuations, while it benefits from increasing the number of samples. Furthermore, the uncertainty on the evaluation of the Reynolds shear stress is also influenced by the degree of correlation of the velocity fluctuations in the different directions.

### 3.4 Proper Orthogonal Decomposition

POD is a well-established tool for statistical data analysis and reduction and is especially advantageous in the analysis of turbulent flows. Its earliest applications are by Lumley (1967) and follow from the discovery of organized motion in turbulence and the consequent introduction of the concept of *coherent structure* (Townsend 1956). Essentially, the POD method relies on the identification of such structures to distill the relevant information on the flow dynamics. The salient aspects of this procedure are briefly illustrated in the remainder of this section. The reader is referred to Berkooz *et al* (1993) for details on the mathematical background of POD. In the current thesis the coherent structures and the associated fluctuations dominating the near-wake dynamics are examined with the snapshot POD method (Sirovich 1987).

Within this approach the instantaneous velocity field retrieved from the PIV snapshots is preliminarily decomposed into a time-averaged velocity field  $\mathbf{U}(\mathbf{x})$  and a fluctuating velocity field  $\mathbf{u}'(\mathbf{x}, t)$  as follows

$$\mathbf{u}(\mathbf{x}, t) = \mathbf{U}(\mathbf{x}) + \mathbf{u}'(\mathbf{x}, t) \quad (3.19)$$

The fluctuating velocity thus obtained is spatio-temporally decomposed and expressed in terms of the following discrete sum

$$\mathbf{u}'(\mathbf{x}, t) = \sum_{k=1}^{N_s} \boldsymbol{\Phi}_k(\mathbf{x}) \cdot \mathbf{c}_k(t) \quad (3.20)$$

wherein  $N_s$  represents the number of available snapshots. The functions  $\Phi_k(\mathbf{x})$  are called eigenmodes or POD modes and account for the spatial organization of the turbulent fluctuations, whereas the coefficients  $\mathbf{c}_k(t)$  provide information on the characteristic time-scales of the modes.

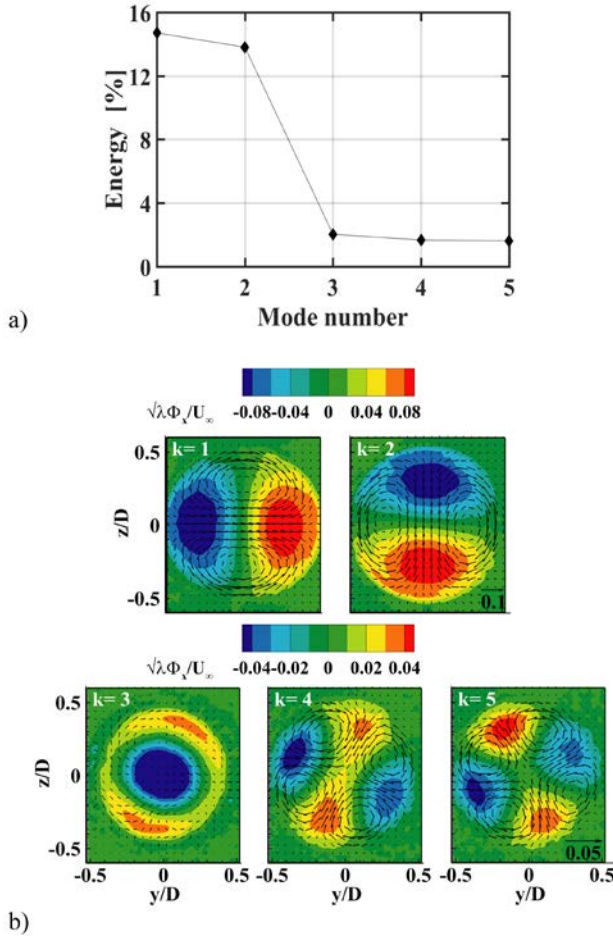


**Figure.3.25** Modes  $k = 1 - 5$  obtained from the snapshot POD decomposition of a turbulent axisymmetric near-wake. Energy distributions (a) and spatial eigenmodes (b). Colors in (b) coded out-of-plane component of the mode. Vectors plotted every 5th grid point represent in-plane mode components  $\sqrt{\lambda_k} \Phi_{k,y} / U_\infty$  and  $\sqrt{\lambda_k} \Phi_{k,z} / U_\infty$ .  $x/D = 0.3$ .  $Re_D = 67,000$ .

This decomposition is the most efficient in terms of kinetic energy contained in the flow. The associated eigenvalues  $\lambda_k$  represent the contributions of the single modes to the turbulent kinetic energy of the flow. As a result of the SVD, they are sorted in a decreasing order, i.e. the first POD modes account for the dominant fluctuations.

Lastly, the time-coefficients  $\mathbf{c}_k(t)$  are obtained from the projection of the fluctuating velocity field  $\mathbf{u}'(\mathbf{x}, t)$  onto the basis of the orthonormal spatial functions  $\Phi_k(\mathbf{x})$  as follows

$$\mathbf{c}_k(t) = \mathbf{u}'(\mathbf{x}, t) \otimes \Phi_k(\mathbf{x}) \quad (3.22)$$

The so-called *coherent fluctuations* can be identified by this procedure with the first  $M$  most energetic POD modes. Based on those modes the velocity field can be reconstructed as follows

$$\mathbf{u}'(t, t) = \mathbf{U}(\mathbf{x}) + \sum_{k=1}^M \Phi_k(\mathbf{x}) \cdot \mathbf{c}_k(t) \quad (3.23)$$

This spatial coherence tends to halve for the two modes  $k = 3$  and  $k = 4$ , which represent smaller-scale wake fluctuations. The corresponding ROM reconstruction of the velocity field based on the first two modes and shown in Fig. 3.26 only retains the large-scale wake fluctuations, while filtering out the smaller-scale ones.

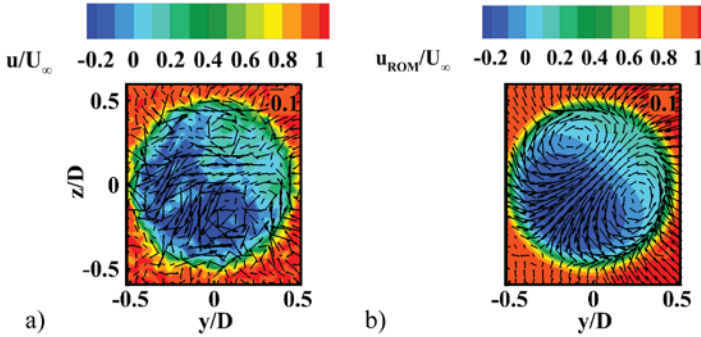


**Figure 3.26** Instantaneous velocity snapshot and corresponding ROM reconstruction based on the POD modes  $k = 1$  and  $k = 2$ . Colors coded out-of-plane component. Vectors plotted every 5th grid point represent in-plane components.  $x/D = 0.3$ .  $Re_D = 67,000$ .





## CHAPTER 4

*“You tackle a stairway face on,  
for if you try it backwards or sideways,  
it ends up being particularly uncomfortable.”*  
Julio Cortázar, *Cronopios and Famas*

### AFTERBODY EFFECTS ON AXISYMMETRIC BASE FLOWS

**Abstract** This chapter investigates the behavior of the turbulent separated flow over an axisymmetric backward facing step (BFS) towards variations in the step height  $h$ . Two-component PIV measurements are conducted in the near-wake of an ogive-cylinder with afterbody for a diameter-based Reynolds number  $Re_D = 67,000$ . The step height is varied during the measurements by increasing the afterbody diameter starting from a reference truncated-base configuration (i.e. without afterbody) to a maximum diameter ratio  $d/D = 0.8$ . For the same step height additional measurements are conducted on planar BFS geometries. The mean reattachment distance is found to vary between  $2h$  and  $4h$  with increasing afterbody diameters, while the size of the velocity defect shrinks from  $1.2D$  to  $0.4D$ . For sufficiently small values of the step height, viz.  $h/D \leq 0.2$ , the reattachment behavior appears comparable to what observed for the corresponding planar configurations, thus suggesting an important influence of the base axisymmetry on the development of the separated flow. The distribution of the vorticity thickness along the reattachment length gives no evidence of afterbody effects on the shear layer growth rate. Instead, the streamwise distributions of the turbulence statistics, especially in the vertical directions, reveal a marked influence of the base geometry on the flow unsteadiness. Snapshot POD analysis of the fluctuations shows the inhibition of the shear layer *flapping* mode for diameter ratios  $d/D \geq 0.4$ .

The current results promote the hypothesis that the size of the afterbody and geometry, viz. planar versus axisymmetric, plays a crucial role in the development of a turbulent separated flow, by influencing the reattachment location and strongly interfering with the large-scale fluctuations.\*

---

\*This work has been published in Gentile *et al* (2016) AIAA Journal **54**(8):2285-2294.

## 4.1 Introduction

Turbulent separated flows past axisymmetric objects are often encountered in the engineering applications involving aerospace vehicles. Such flows result from the abrupt changes in the rear geometry of so-called bluff bodies and feature the development of a free shear layer bounding an inner region of low-speed recirculating flow. The flow field establishing downstream of the trailing edge, commonly referred to as *near-wake*, has been widely investigated in literature (cf. chapter 2).

Past experimental studies conducted over the entire subsonic flow regime (cf. Merz *et al* 1978 and Merz 1979) showed that the recirculation region in the turbulent near-wake behind a cylinder is characterized by strong pressure fluctuations, whose frequency is inversely proportional to the incoming flow speed. More recent experiments conducted in the subsonic regime by Wolf *et al* (2012) on a blunt-based rocket model showed a significant reduction of the near-wake fluctuations when adding an afterbody to the truncated base. The latter configuration is often regarded in literature as an axisymmetric backward facing step (BFS) and is widely investigated in the transonic regime as a generic geometric model of the afterbody configuration of modern space launcher vehicles. Wall-pressure measurements conducted by Dépres *et al* (2004) revealed that depending on the length of the afterbody with respect to the main body diameter, i.e.  $L/D$ , such flows could either feature impingement of the separated shear layer onto the surface of the afterbody, i.e. *solid reattachment*, or convergence of the separation streamlines with formation of a stagnation point away from the base, i.e. *fluidic reattachment*.

In the case of planar BFS flows Eaton and Johnston (1981) and Jovic and Driver (1994) identified the step height  $h$  and the thickness of the separating boundary layer as main governing parameters of the reattachment length  $x_r$ . Experiments conducted by Hudy *et al* (2005) on an axisymmetric BFS geometry showed a downstream shift of the reattachment position with increasing step height-based Reynolds numbers  $Re_h$ . Furthermore evidence was given in both the axisymmetric and the planar case, of a cyclical variation of the reattachment point due to the unsteady nature of the separated flow (Le *et al* 1997; Spazzini *et al* 2001; Deck and Thorigny 2007).

Despite the similarities of planar and axisymmetric BFS flows, especially within the first half of the reattachment region (Eaton and Johnston 1981), the comparison between the available data reveals some major differences, which can be mainly ascribed to three-dimensionality effects.

The present study focuses on the influence of the base geometry on the behavior of separating and reattaching turbulent flows with particular emphasis on the scaling of the reattachment length. The main objective is to determine to what extent the three-dimensionality of the base makes the axisymmetric reattachment process deviate from the planar case. Further goal of the investigation is to assess the influence of the step height on the separated flow topology and on the development of the large-scale unsteadiness.

Two-component PIV measurements are carried out on an axisymmetric BFS geometry

consisting of an ogive-cylinder with afterbody. The step height is varied by changing the afterbody diameter. Additional measurements are performed on equivalent planar BFS geometries to compare the scaling of the reattachment distance in the axisymmetric and in the two-dimensional case. The mean flow topology, turbulence statistics, and shear-layer development are characterized. Lastly, the effect of the base geometry on the large-scale fluctuations is analyzed using the snapshot POD method (Sirovich 1987).

## 4.2 Experimental setup

### 4.2.1 Flow facility and wind tunnel model

The measurements were conducted in the low-speed wind tunnel (W-Tunnel) operated at the Aerodynamics Laboratories of Delft University of Technology.

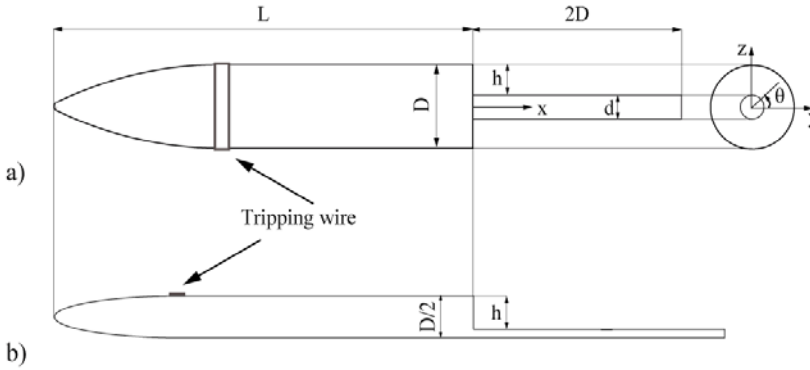


**Figure 4.1** Schematics of the experimental geometries. Side and end view of the axisymmetric BFS model (a). Side view of the planar BFS model (b).

The model was an axisymmetric BFS comprising an ogive-cylinder of total aspect ratio  $L/D = 5$  with blunt trailing edge equipped with a cylindrical afterbody of smaller diameter  $d$  (Fig. 4.1a). The afterbody length ensured reattachment of the shear layer on the wall for all experimental conditions (Dépres *et al* 2004). A 10 mm wide roughness element was placed just downstream of the nose-to-body junction in order to ensure a fully turbulent boundary layer at the trailing edge. The model was supported from the bottom by a thin vertical plate with sharp trailing and leading edges. This support was further installed on a mounting system allowing for translations in the streamwise direction and adjustment of the yaw and the pitch angle, in view of the reported sensitivity of the turbulent axisymmetric wake towards angular misalignments (Klei 2012; Wolf *et al* 2013). The model was placed within an extension of the test section featuring Plexiglas walls, which allowed full optical access.

The afterbody to main body diameter ratio was varied during the experiments in the range  $d/D = \{0; 0.2; 0.4; 0.6; 0.8\}$ , yielding a non-dimensional step height range

$h/D = \{0.5; 0.4; 0.3; 0.2; 0.1\}$ . The resulting step-height-based Reynolds number  $Re_h$  was between 6,700 and 33,000.

**Table 4.I** Experimental test cases overview

Geometry	$U_\infty$ [m/s]	$d/D$	$h/D$	$Re_h$
Axisymmetric	20	0.0	0.5	33,000
Axisymmetric	20	0.2	0.4	27,000
Axisymmetric	20	0.4	0.3	20,000
Axisymmetric	20	0.6	0.2	13,000
Axisymmetric	20	0.8	0.1	6,700
Planar	20	-	0.4	27,000
Planar	20	-	0.3	20,000
Planar	20	-	0.1	6,700

For the comparison between axisymmetric and planar case, additional measurements were performed on a planar BFS plate featuring an elliptical nose with 3:1 aspect ratio (Fig. 4.1b). The step height was varied during the experiments in order to account for non-dimensional step heights between  $h/D = 0.1$  and  $h/D = 0.4$ ,  $D$  indicating the axisymmetric model base diameter. The reader is referred to section 3.1 of the present dissertation for a detailed description of the flow facility and wind tunnel models. An overview of the present experimental test cases is provided in Table 4.I.

#### 4.2.2 Measurement apparatus and procedure

Two-component PIV measurements were performed in a plane aligned with the freestream flow and containing the model symmetry axis. The region of interest spanned from 1 cm upstream of the separation point up to approximately 1.5 cm downstream of the largest reattachment distance found in the present study.

The flow was seeded by a SAFEX smoke generator with droplet tracers of  $1 \mu\text{m}$  diameter at a uniform concentration of approximately  $5 \text{ particles/mm}^3$ . Illumination was provided by a Quantronix Darwin Duo Nd-YLF laser ( $2 \times 25 \text{ mJ/pulse}$  at  $1 \text{ kHz}$ ). Two Photron FastCAM SA1.1 CMOS cameras (maximum resolution  $1024 \times 1024$  pixels,  $20 \mu\text{m}$  pixel pitch) each one equipped with  $105 \text{ mm}$  Nikkor objective were used to record the light scattered by the tracer particles (Fig. 4.2). The data were recorded at each streamwise station at two distinct frequencies, viz.  $100 \text{ Hz}$  and  $2 \text{ kHz}$ , in order to retrieve statistically converged information on the separated flow field and capture the characteristic time-scales of the large-scale fluctuations.

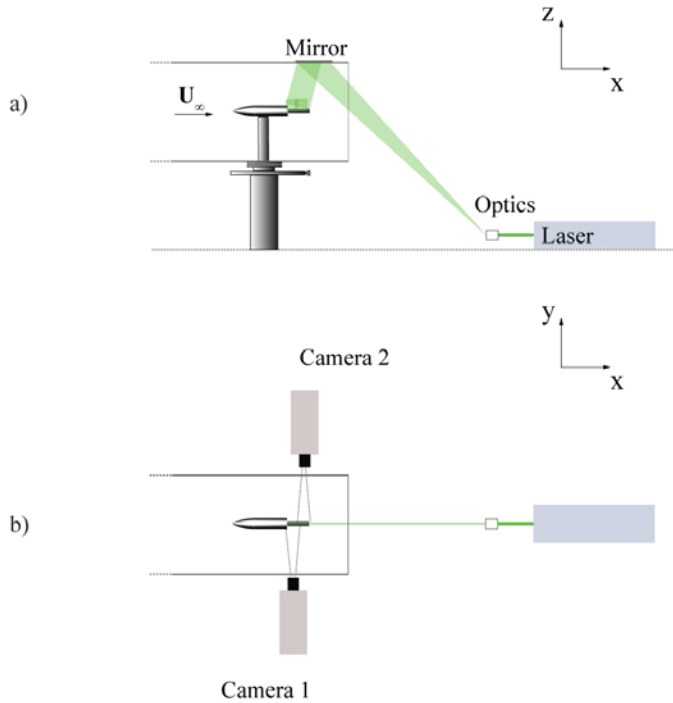


**Figure 4.2** Wind tunnel model and PIV illumination and imaging setup for the measurements on the axisymmetric configurations. Side view (a). Top view (b).

**Table 4.II** Main PIV measurement settings

Diameter-based Reynolds number $Re_D$	67,000
Laser sheet thickness $t$	2 mm
Laser pulse separation $\Delta t$	25 $\mu$ s
Objective f- number $f_\#$	2.8
FOV size	55 x 55 mm <sup>2</sup>
Image magnification $M$	0.33
Vector pitch	0.24 mm
Acquisition frequency $f_{acq}$	100 – 2000 Hz
Data ensemble size $N$	2000
Measurement duration $T$	1 - 20 s

Considering the wake flow sensitivity towards small misalignments (cf. section 3.3), preliminary experiments were conducted on the truncated-base configuration such to verify the alignment of the model with respect to the

freestream flow. An overview of the main PIV measurement parameters is provided in Table 4.II.

### 4.2.3 Data processing and assessment

The recorded images were pre-processed to reduce the effects of light reflections from the model surface and background intensity. An iterative multigrid spatial cross-correlation algorithm based on window deformation (Scarano and Riethmuller 1999) was used for image interrogation. Spurious vectors were removed from the resulting vector fields by use of a median filter (Westerweel and Scarano 2005). For further details on the data processing the reader is referred to subsection 3.2.1.

**Table 4.III Overview of the main uncertainty contributions**

Uncertainty on wall-location $\Delta h$	0.1 - 0.2 mm
Cross-correlation uncertainty $\epsilon_{cc}$	0.1 pixels
Instantaneous velocity uncertainty $\epsilon_{u'}/U_\infty$	1.5%
Statistical uncertainty $\epsilon_{\bar{u}}/U_\infty$	0.8%
Velocity fluctuations uncertainty $\epsilon_{u'}/\langle u' \rangle_{max}$	2.0%
Reynolds shear stress uncertainty $\epsilon_{u'v'}/\langle u'v' \rangle_{max}$	7.0%

The average cross-correlation signal-to-noise (SNR) was estimated to be above 3 for the present measurements. The main uncertainty contributions are listed in Table 4.III. Details on the evaluation of such contributions are provided in section 3.3.

## 4.3 Results

### 4.3.1 Boundary layer properties

The mean boundary profile was examined 5 mm upstream of the trailing edge in order to assess the conditions of the separated shear layer. The sum of correlation approach (Meinhart *et al* 1999) was used to enhance the spatial resolution in proximity of the wall. Valid velocity data could be obtained up to  $z = 0.3$  mm above the wall (i.e.  $z/\delta_{95} = 0.06$ ), where the streamwise component of the velocity was approximately 33% of the freestream value. Below this ordinate the boundary layer properties were obtained with a linear extrapolation of the velocity profile to the wall.

**Table 4.IV Boundary layer properties**

$U_\infty$ [m/s]	$\delta_{95}$ [mm]	$\delta^*$ [mm]	$\theta$ [mm]	$H$	$Re_\theta$
20	$4.8 \pm 0.12$	$1.1 \pm 0.10$	$0.68 \pm 0.01$	$1.7 \pm 0.10$	$900 \pm 20$

The thickness of the boundary layer is herein identified with the  $z$ -position where the velocity reaches 95% of the freestream value and was estimated to be  $\delta_{95} = 4.8$  mm. The resulting boundary layer integral parameters are provided in Table 4.IV along with the uncertainty values associated with the wall identification error.

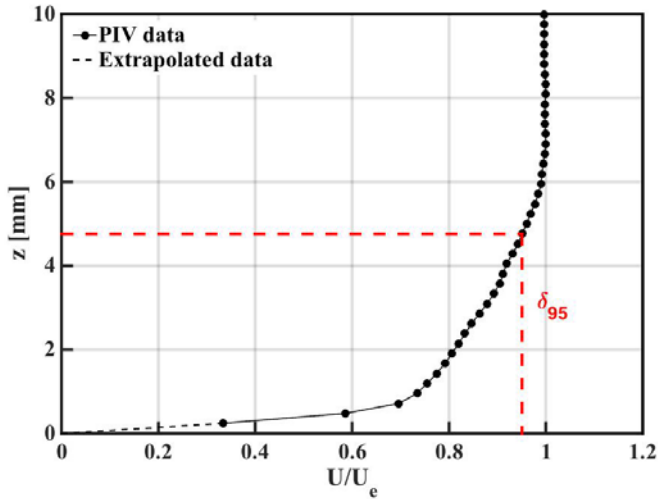


**Figure 4.3** Mean boundary layer velocity profile 5 mm upstream of separation.

### 4.3.2 Mean flow field

Axisymmetric and planar BFS flows are examined hereafter for various values of the step height  $h$ . Throughout the discussion the main body diameter  $D$  is used as a scaling parameter for the spatial coordinates  $(x, z)$ , whereas the freestream velocity  $U_\infty$  is used to normalize the velocity components  $(u, w)$ . The different test cases are identified using either the diameter ratio  $d/D$  or the non-dimensional step height  $h/D$ .

The mean flow field found for the different axisymmetric configurations is presented in Fig. 4.4. The backflow region is highlighted by a white contour line to ease visualization. The color contours of the longitudinal velocity define the development of the velocity defect downstream of the trailing edge. The latter features thickening of the shear layer in the streamwise direction and reduction of the inner reversed-flow region. In absence of rear-protrusion (i.e.  $h/D = 0.5$  or  $d/D = 0$ ) the end of the separated region is identified with the rear-stagnation point located at  $x/D = 1.2$  and is referred to as point of fluidic reattachment. In presence of an afterbody instead, the end of the separated region is identified as the first location along the afterbody wall where the longitudinal velocity changes from negative to positive.

For  $d/D = 0$  (Fig. 4.4a) the mean streamlines define a torus-like vortex region with foci in the  $xz$ -plane at  $(x/D, r/D) = (0.60, 0.37)$  surrounding the backflow



region. The velocity of the reversed flow is found to attain a maximum of  $0.3 U_\infty$  downstream of the vortex core at  $x/D = 0.7$ , which point is located at approximately 60% of the rear-stagnation point.

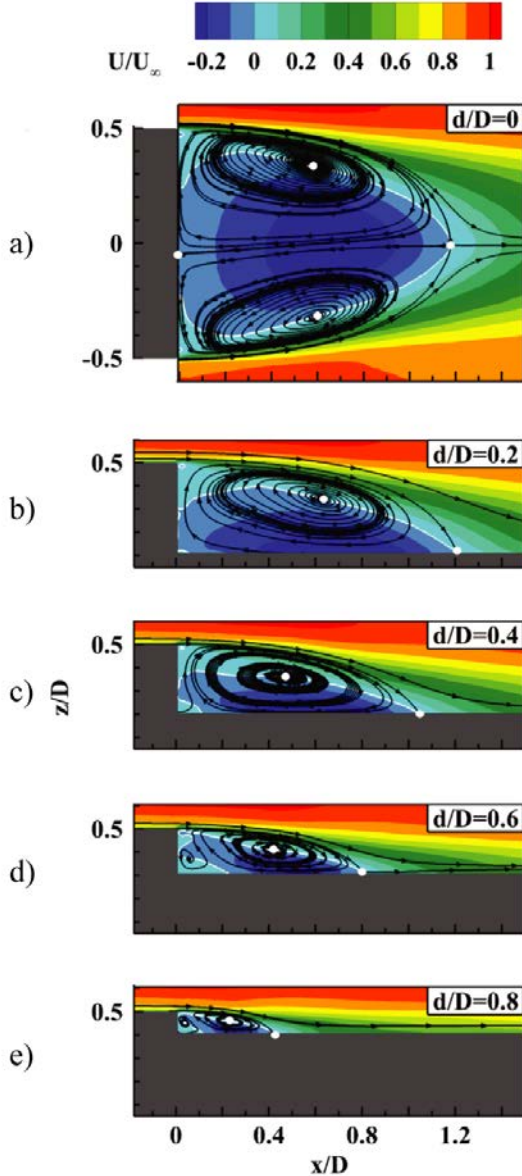


Figure 4.4 Time-averaged velocity field for increasing  $d/D$ . Color coded longitudinal velocity. White contour line indicating backflow region. White dots indicating foci and reattachment points. Model in gray.

A good agreement is found with the experimental results of Wolf *et al* (2012) for a similar configuration, which identified the rear-stagnation point at  $x/D = 1.25$  and documented a maximum backflow velocity of  $0.32 U_\infty$  at  $x/D = 0.75$ .

The topology of the streamlines returning from the rear-stagnation point towards the base shows a small degree of asymmetry, reflecting the presence of a residual misalignment of the model with respect to the freestream flow. The surveys of Klei (2012) and Wolf *et al* (2013) give evidence of substantial asymmetries in the mean topology of the wake for misalignment angles in the order of  $\pm 0.3^\circ$ . In the current measurements such misalignments were estimated to be below  $0.1^\circ$ .

**Table 4.V Reattachment length  $x_r$ , for increasing  $d/D$**

Author	$d/D$	$h/D$	$x_r/D$	$x_r/h$	$Re_h$	$\theta/h$
Current axi	0.0	0.5	1.2	2.4	33,000	0.03
Current axi	0.2	0.4	1.2	3.0	27,000	0.03
Current axi	0.4	0.3	1.0	3.5	20,000	0.05
Current axi	0.6	0.2	0.8	4.1	13,000	0.07
Current axi	0.8	0.1	0.4	4.2	6,700	0.14
Wolf <i>et al</i> (2012)	0.0	0.5	1.3	2.5	$2.5 \cdot 10^5$	-
Wolf <i>et al</i> (2012)	0.4	0.3	1.1	3.7	$1.5 \cdot 10^5$	-
Hudy <i>et al</i> (2005)	0.8	0.1	0.4	5.0	32,327	0.15
Hudy <i>et al</i> (2005)	0.8	0.1	0.4	4.3	5,980	0.10
Current 2D	-	0.4	2.4	5.9	27,000	0.03
Current 2D	-	0.3	1.8	5.9	20,000	0.05
Current 2D	-	0.1	0.5	5.1	6,700	0.15
Spazzini <i>et al</i> (2001)	-	-	-	6.5	16,000	-
Spazzini <i>et al</i> (2001)	-	-	-	6.1	10,000	-
Spazzini <i>et al</i> (2001)	-	-	-	5.4	5,100	-

Adding an afterbody of relatively small diameter, viz.  $d/D = 0.2$ , to the truncated base does not seem to alter the mean near-wake topology substantially in terms of vortex core location and reattachment distance (Fig. 4.4b). However, the reattachment distance progressively reduces up to  $0.4 D$  when further increasing the afterbody diameter ratio to  $d/D = 0.8$ , yielding a corresponding reduction of the shear layer curvature and shrinking of the backflow region (Fig. 4.4c-e). The process above is accompanied by the appearance of a secondary (counter-rotating) recirculation region near the junction between the main body and the afterbody. This secondary vortex grows with decreasing step heights, becoming almost as large as the main recirculation region for  $d/D = 0.8$ . The development of a similar secondary vortex region has been reported for axisymmetric (Deck and Thorigny, 2007; Wolf *et al* 2012; Hudy *et al* 2005) as

well as planar (Spazzini *et al* 2001) BFS flows and displays a cyclical process of growth-decay up to length-scales in the order of the step-height  $h$ .

The reattachment lengths  $x_r$  found for the test cases above are provided in Table 4.V. The values obtained for the equivalent planar geometries as well as values extracted from former studies (Spazzini *et al* 2001; Hudy *et al* 2005; Wolf *et al* 2012) are reported for comparison.

The reattachment length scaled with the step height,  $x_r/h$ , is shown in Fig. 4.5 as a function of the diameter ratio  $d/D$ . Despite of the progressive shrinking of the separated region shown in Fig. 4.4, the reattachment distance is found to increase from  $2.4 h$  to  $4.2 h$  with increasing diameter ratios. The data of Wolf *et al* (2012) show the same trend with a good quantitative agreement. The results of Hudy *et al* (2005) suggest an important influence of the Reynolds number, which in that study was varied by changing the flow speed while leaving the step height unchanged. This then also changes the boundary layer properties at the location where the flow separates.

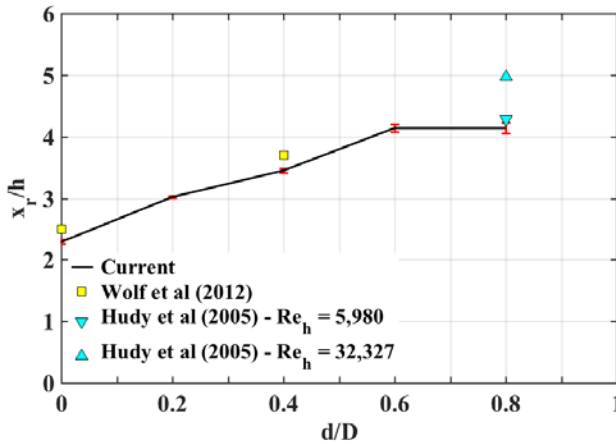


**Figure 4.5** Non-dimensional reattachment length as a function of  $d/D$ . The error bars represent the uncertainty  $\Delta x_r$  in the identification of the reattachment location.

A comparison between planar and axisymmetric flow reattachment is presented in Fig. 4.6, where the reattachment distance is displayed as a function of the Reynolds number  $Re_h$ . For the present experiments, larger values of  $Re_h$ . (i.e. larger step heights) are found to promote the reattachment in the axisymmetric case, while delaying it in the planar case.

For step heights below a certain value (i.e.  $h/D \leq 0.2$  or  $d/D \geq 0.6$ ) the reattachment lengths of planar and axisymmetric configurations appear to scale similarly, thus reflecting a diminishing influence of the axial symmetry of the base geometry.

The data extracted from Hudy *et al* (2005) outline a behavior which shares more similarities with the planar geometries considered in both the present investigation and the study of Spazzini *et al* (2001). This seeming discrepancy reflects the circumstance that in the study of Hudy *et al* (2005) the  $Re_h$  is increased by increasing the flow speed. Thus, for a planar geometry, as well as for an axisymmetric one with constant diameter ratio, the scaling of the reattachment length is governed by the Reynolds number, with consequent reduction of the thickness of the separating boundary layer and increase of the reattachment distance (Eaton and Johnston 1981). The present axisymmetric data on the other hand, were achieved at a constant flow speed and varying afterbody-to-base diameter ratio, and are hence dominated by geometry effects.

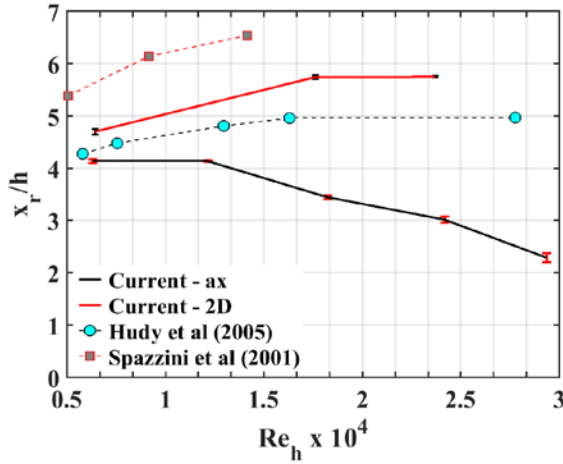


**Figure 4.6** Non-dimensional reattachment length as a function of  $Re_h$ . Error bars represent the uncertainty  $\Delta x_r$  in the identification of the reattachment location.

### 4.3.3 Shear layer development

The effects of the base geometry on the shear layer development over the axisymmetric BFS are discussed based on the time-averaged velocity data. For this purpose the streamwise evolution of the vorticity thickness is examined. The latter is computed according to the definition by Smits and Dussauge (2006)

$$\delta_\omega(x) = \frac{\Delta U(x)}{\max_z \left( \left| \frac{\partial U(x,z)}{\partial z} \right| \right)} \quad (4.1)$$

wherein  $\Delta U$  is the maximum velocity difference across the shear layer and  $\frac{\partial U(x,z)}{\partial z}$  is the velocity gradient at a given station.

The vorticity thickness increases at an approximately linear rate in the streamwise direction and saturates in proximity of the reattachment point, where a plateau is attained (Fig. 4.7). The shear layer development displays no sensitivity towards the base geometry. In fact, the rate of increase of the vorticity thickness is found to be  $d\delta_\omega/dx \sim 0.27$  for all configurations examined. At transonic speed Schrijer *et al* (2014) and Deck and Thorigny (2007) reported a slightly lower value, viz.  $d\delta_\omega/dx \sim 0.2$ , for a similar afterbody configuration with  $d/D = 0.4$ . This discrepancy is attributed to compressibility effects (Slessor *et al* 2000).

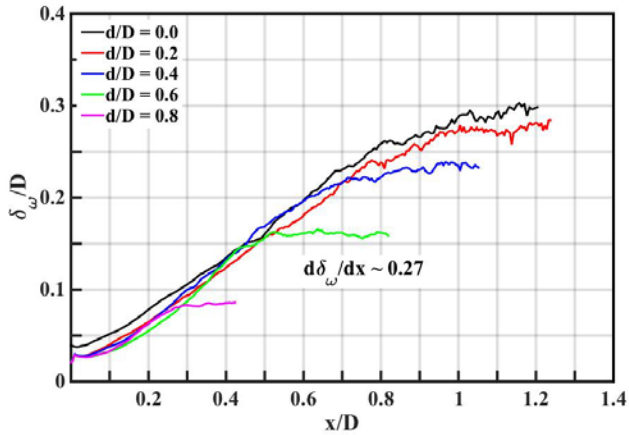


**Figure 4.7** Streamwise evolution of the vorticity thickness for increasing afterbody diameter ratios  $d/D$ .

#### 4.3.4 Turbulence statistics

The spatial distributions of the Reynolds normal and shear stresses are examined in relation to the flow unsteadiness. The color contour plots of the normal stresses in the longitudinal direction  $\langle u'^2 \rangle^{1/2}$  and in the vertical direction  $\langle w'^2 \rangle^{1/2}$  are shown in Fig. 4.8 and 4.9 respectively.

The color contours show the intensification of the longitudinal fluctuations along the mixing layer. The peak values are found to reduce from  $0.18 U_\infty$  to  $0.13 U_\infty$  with increasing afterbody diameters. The vertical fluctuations intensify in proximity of the reattachment in a region, which is located close to the wake axis in the truncated-base case and close to the wall in presence of the afterbody. The peak values of the vertical fluctuations are found to reduce from  $0.19 U_\infty$  to  $0.10 U_\infty$  with increasing afterbody diameters, thus revealing a pronounced sensitivity towards the base geometry. This behavior is ascribed to the obstruction by the afterbody towards the radial motion of the shear layer.

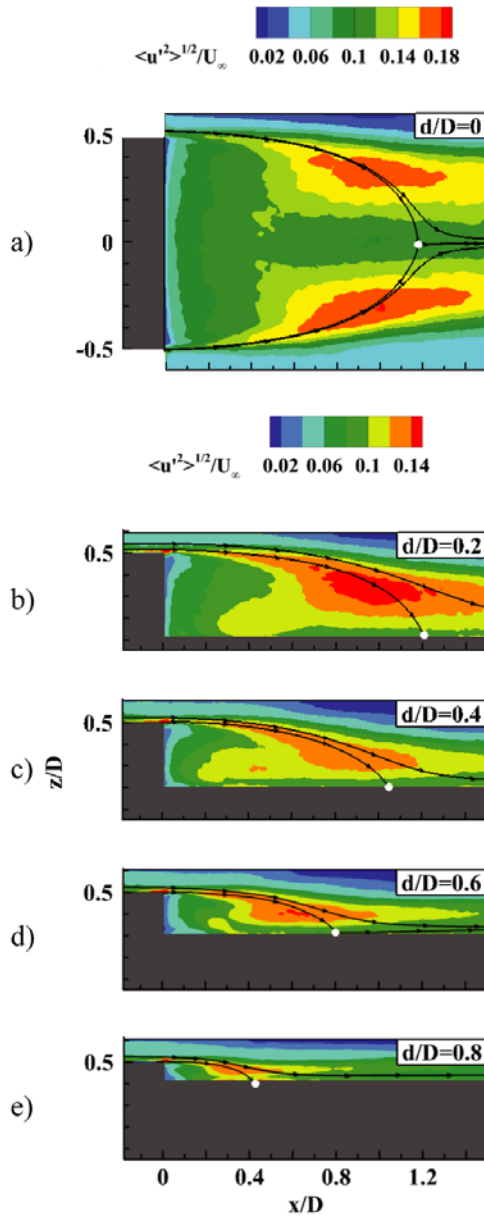


Figure 4.8 RMS of the longitudinal velocity fluctuations for increasing  $d/D$ . Mean reattaching streamline in black. White dots indicating foci and reattachment points. Model in gray.

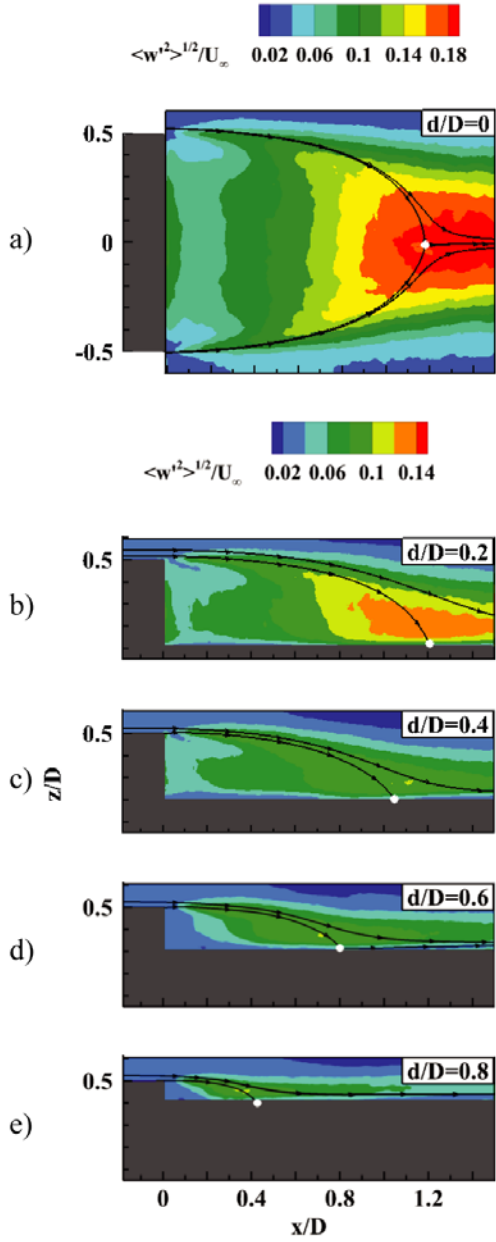
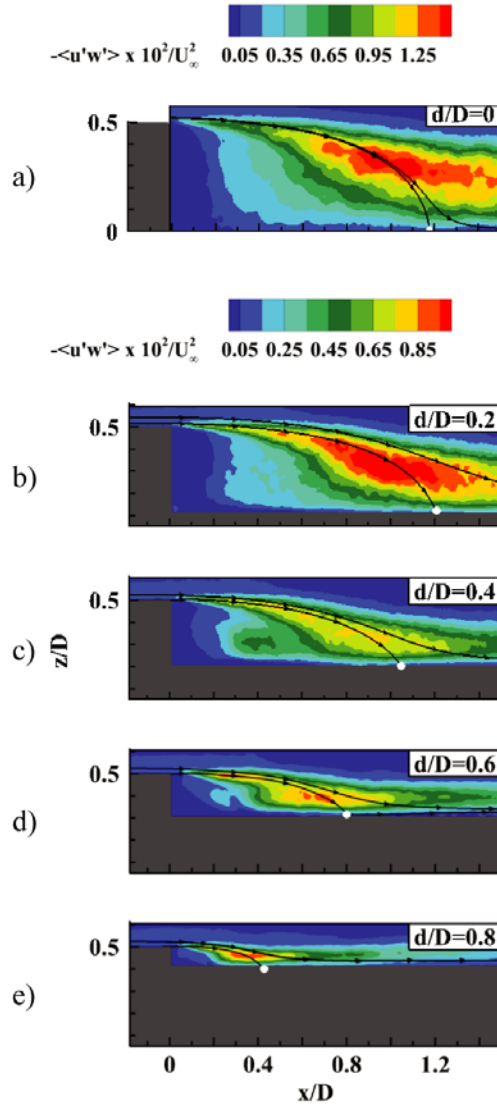


Figure 4.9 RMS of the vertical velocity fluctuations for increasing  $d/D$ . Mean reattaching streamline in black. White dots indicating foci and reattachment points. Model in gray.



**Figure 4.10 Reynolds stresses for increasing  $d/D$ . Mean reattaching streamline in black. White dots indicating foci and reattachment points. Model in gray.**

The current results are in good agreement with the studies of Wolf *et al* (2012) who investigated a similar truncated-base rocket configuration. These authors in particular, reported a reduction by approximately 25% in the turbulence intensity upon addition of an afterbody with  $d/D = 0.4$ .

The current results are in good agreement with the studies of Wolf *et al* (2012) who investigated a similar truncated-base rocket configuration. These authors in particular,



reported a reduction by approximately 25% in the turbulence intensity upon addition of an afterbody with  $d/D = 0.4$ . The peak values found for the fluctuations in both directions are comparable to the values reported in Wolf *et al* (2010), wherein the fluctuations attained maxima of approximately  $0.19 U_\infty$  in both the longitudinal and vertical direction in a region between  $x/D = 0.75$  and  $x/D = 1.75$ .

Fig. 4.10 shows the distributions of the Reynolds shear stresses  $\langle -u'w' \rangle$  obtained for increasing afterbody diameters. To ease the comparison only the half-plane  $z/D \geq 0$  is displayed for the bluff-based case (i.e.  $d/D = 0$ ). The peak values are concentrated in the mixing layer and are found to reduce from  $0.016 U_\infty^2$  to  $0.009 U_\infty^2$  with increasing diameter ratios.

### 4.3.5 Proper Orthogonal Decomposition

Snapshot POD analysis of the velocity fluctuations (Sirovich 1987) was conducted in order to examine the near-wake large-scale fluctuations. Details on the adopted mathematical procedure are provided in section 3.4 of the present dissertation.

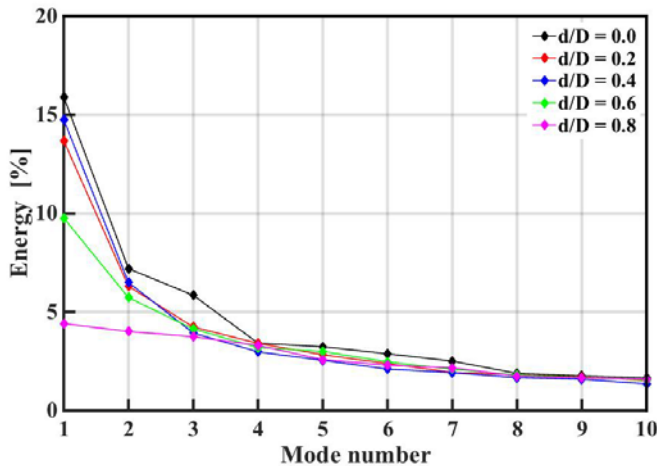


Figure 4.11 Energy distribution over the POD modes.

To ensure a comparison of the different cases on domains of equal size, the analysis of the truncated-base case was restricted to the half-plane  $z/D \geq 0$ . Thus, the domain of analysis spanned over approximately  $1.5 D$  in the streamwise direction and  $0.6 D$  in the vertical direction for all cases considered. The relative contributions of the first 10 POD modes to the flow turbulent kinetic energy are shown in Fig. 4.11.

The spectra outline a progressive decrease in the importance of the low-order modes with increasing afterbody diameters (i.e. smaller step heights). Such a

behavior is indicative of a decreasing large-scale organization from the scale of the afterbody diameter to that of the step height. In particular, in absence of a central protrusion mode  $k = 1$  captures almost 16% of the total turbulent kinetic energy of the flow, whereas its contribution reduces to 4.5% as the afterbody diameter is increased up to  $d/D = 0.8$ .

For this latter case no dominant mode can be identified in the spectrum, thus indicating the absence of a large-scale organization in the flow. An overview of the energy contributions of the first three modes is given in Table 4.VI.

**Table 4.VI**      **Relative energy content of the first three POD modes**

Author	$d/D$	$h/D$	$Re_h$	$\lambda_1$ [%]	$\lambda_2$ [%]	$\lambda_3$ [%]
Current axi	0.0	0.5	33,000	15.9	7.1	5.9
Current axi	0.2	0.4	27,000	13.8	6.3	4.3
Current axi	0.4	0.3	20,000	14.8	6.5	3.9
Current axi	0.6	0.2	13,000	9.9	5.8	4.2
Current axi	0.8	0.1	6,700	4.5	4.1	3.9
Wolf <i>et al</i> (2012)	0.0	0.5	$2.5 \cdot 10^5$	14.5	5.8	4.0
Wolf <i>et al</i> (2012)	0.4	0.3	$1.5 \cdot 10^5$	8.8	6.9	3.5
Schrijer <i>et al</i> (2014)	0.4	0.3	$3.2 \cdot 10^4$	16.0	9.0	6.0

The spatial distribution of the first POD mode  $k = 1$  is shown in Figure 4.12. The color contours of the longitudinal component of the mode define a region of intense fluctuations, with peaks attained in proximity of the reattachment. The in-plane vectors indicate the occurrence of a nearly vertical upward motion close to the wall. Such a concentration of streamwise momentum is commonly associated with a flapping motion of the shear layer (Wolf *et al* 2012; Schrijer *et al* 2014). The energy contribution of the first mode is found to reduce with increasing afterbody diameters. This fact reflects the inhibition of the radial fluctuations of the shear layer due to the presence of the afterbody.

The spatial distributions of the modes  $k = 2$  and  $k = 3$  are reported in Fig. 4.13 and 4.14 respectively. The two modes feature a succession of high and low streamwise momentum regions, whose extension increases with increasing step heights. The alternating of upward and downward motions outlined by the in-plane vectors is associated with shear layer undulation. Based on their relatively similar energy contributions, particularly for large diameter ratios (cf. Fig. 4.11), their combination can be identified with a convective mode. A similar interpretation is provided for  $d/D = 0.4$  by Schrijer *et al* (2014).

The present analysis is concluded by examining the frequencies involved in the most energetic fluctuation modes, as identified with the POD. For this purpose low and high repetition rate measurements are combined.

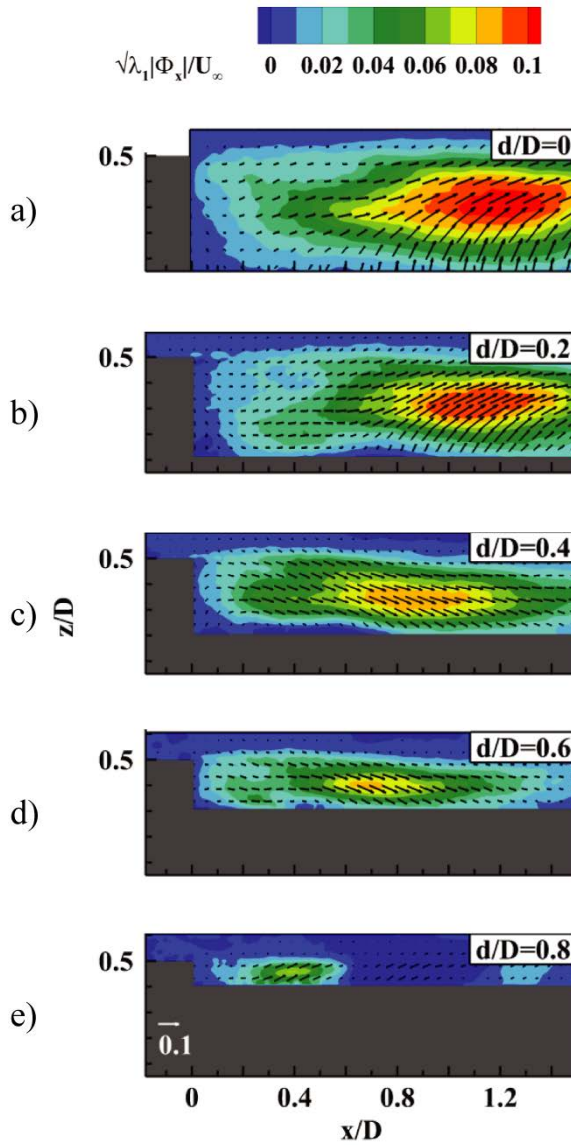


Figure 4.12 POD mode  $k=1$ . Color coded longitudinal component. In-plane vectors plotted every 10th grid point represent in-plane components  $\sqrt{\lambda_1} \Phi_{1,x} / U_\infty$  and  $\sqrt{\lambda_1} \Phi_{1,z} / U_\infty$ .

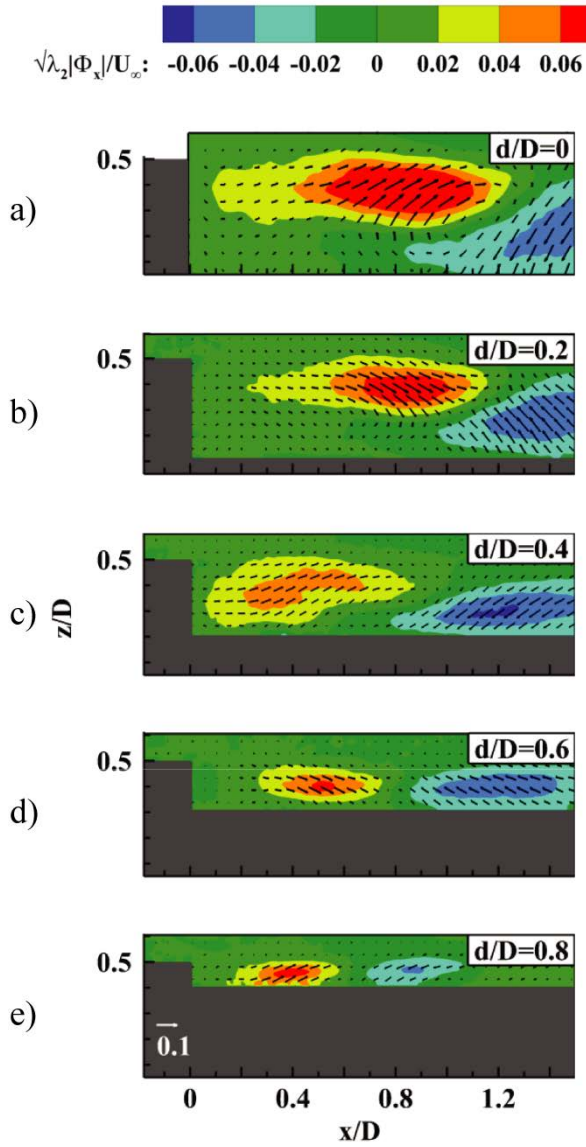


Figure 4.13 POD mode  $k=2$ . Color coded longitudinal component. In-plane vectors plotted every 10th grid point represent in-plane components  $\sqrt{\lambda_2}\Phi_{2,x}/U_\infty$  and  $\sqrt{\lambda_2}\Phi_{2,z}/U_\infty$ .

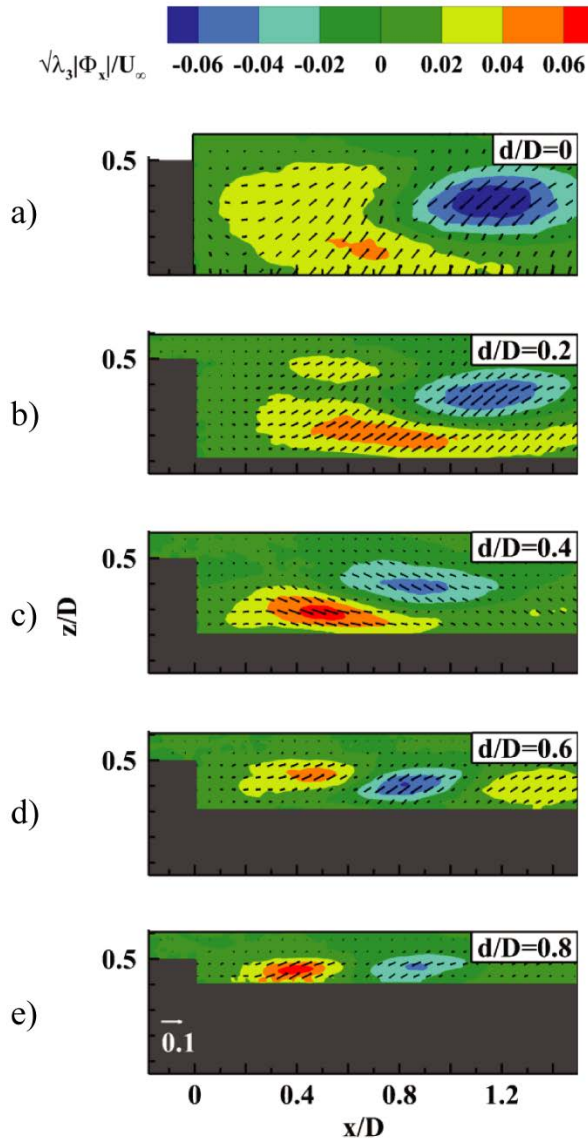
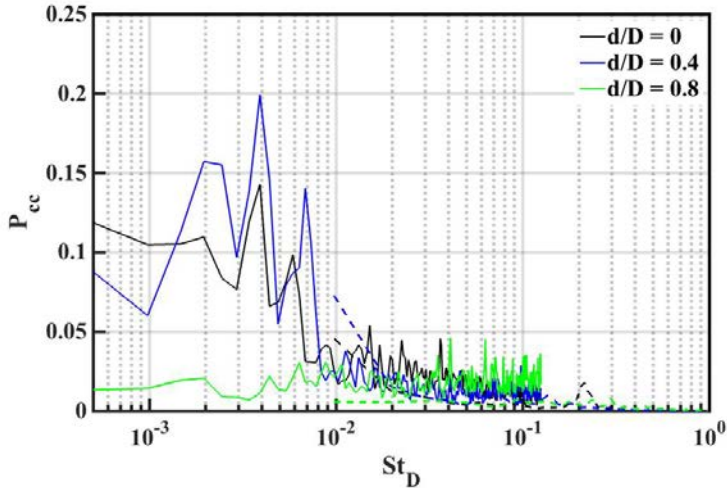


Figure 4.14 POD mode  $k = 3$ . Color coded longitudinal component. In-plane vectors plotted every 10th point represent in-plane components  $\sqrt{\lambda_3}\Phi_{3,x}/U_\infty$  and  $\sqrt{\lambda_3}\Phi_{3,z}/U_\infty$ .

The power spectral density distributions of the first mode  $k = 1$  associated with the shear layer flapping  $c_1(t)$  are presented in Fig. 4.15. For conciseness and clarity, the analysis is restricted to three representative configurations, namely  $d/D = 0, 0.4$  and  $0.8$ . A significant contribution is displayed for  $d/D \leq 0.4$  in the very-low-frequency range corresponding to  $St_D = 10^{-3} - 10^{-2}$ , which can be identified with the inner backflow unsteadiness (Rigas *et al* 2014; Grandemange *et al* 2014; Gentile *et al* 2016a). Due to the orientation of the measurement plane this instability cannot be captured in the present study, as it occurs in the azimuthal-radial plane of the wake. However, the results of additional measurements conducted in this plane show the occurrence of a backflow motion for diameter ratios  $d/D \leq 0.4$  (Gentile *et al* 2016c). The truncated-base configuration also features a peak in the low-frequency range corresponding to  $St_D = 0.2$ , which is traditionally attributed to the vortex shedding. The latter disappears in presence of the afterbody due to its interference with the shear layer radial motion.



**Figure 4.15** Power spectral density of POD time coefficient  $c_1(t)$  for different values of  $d/D$ . Solid line represents low-repetition rate data. Dashed line represents high-repetition rate data.

## 4.4 Conclusions

The influence of the base geometry on the behavior of the turbulent separated flow over an axisymmetric BFS was investigated at a diameter-based Reynolds number  $Re_D = 67,000$ .

Two-component Particle Image Velocimetry measurements were conducted for different values of the step height  $h$  by varying the afterbody diameter from a reference truncated-base configuration, viz. without afterbody, up to a value

comparable to the main body base diameter. The mean velocity field showed that increasing the afterbody cross-section reduces the extension of the separated region and induces the growth of a secondary counter-rotating vortex at the junction between base and afterbody. Using the step height as a scaling parameter however, outlined an increase in the reattachment distance between  $2.5 h$  and  $4.2 h$ . The comparison with the data obtained for equivalent planar BFS flows revealed an opposite trend, whereby the reattachment distance increased from  $5 h$  to  $6 h$  with increasing step heights. The two configurations were found to feature similar reattachment distances for sufficiently small values of the step height, viz.  $h/D \leq 0.2$ , reflecting a decreasing influence of the axial symmetry on the behavior of the separated flow.

The normal and Reynolds shear stress distributions outlined a substantial weakening of the turbulent fluctuations associated with the shear layer development, particularly along the vertical direction, which reflected the inhibition of the radial motion of the shear layer due to the afterbody. POD analysis gave further evidence of a progressive inhibition of the shear layer flapping mode  $k = 1$  for increasing diameter ratios. A convective mode associated with shear layer undulation could be identified with a mode-pair  $k = 2, 3$  for  $d/D \leq 0.4$ . In the latter case the frequency spectra of the first POD time-coefficient highlighted a significant contribution of the flapping mode in the non-dimensional frequency range  $St_D = 10^{-3} - 10^{-2}$ , which was ascribed to the very-low-frequency instability of the backflow region occurring in the azimuthal plane. The truncated-base configuration displayed a second contribution at the shedding frequency  $St_D = 0.2$ .

Based on the present data it could be argued that both the flow organization and the low-frequency unsteadiness associated with the shear-layer development are significantly influenced by changes in the afterbody geometry, although the separated flow preserves its major features in the presence of a central protrusion for  $d/D < 0.4$ .

## CHAPTER 5

“The one who is happy stands still.”  
Thomas Mann, *The Buddenbrooks*

### LOW-FREQUENCY BEHAVIOR OF THE TURBULENT AXISYMMETRIC NEAR-WAKE

**Abstract** This chapter surveys the low-frequency unsteadiness dominating the dynamics of the near-wake of an ogive-cylinder. Time-resolved stereoscopic PIV measurements are carried for a Reynolds number  $Re_D = 67,000$  in different azimuthal-radial planes downstream of the trailing edge. The long-time averaged velocity field renders a toroidal wake topology characterized by an annular shear layer bounding an inner region of recirculating flow. The most intense backflow is found occurring at approximately 60% of the rear-stagnation point location (cf. chapter 4). Inspection of instantaneous PIV snapshots reveals the occurrence of an azimuthal meandering of the reversed-flow region, characterized by a significant radial offset with respect to the mean position. The latter appears dominating the near-wake dynamics in proximity of the base, whereas the fluctuations associated with the shear layer development become dominant closer to the rear-stagnation point. The time-history of the backflow centroid position allows this motion to be identified with a precession about the model symmetry axis, occurring with exceptionally long time-scales, viz. in the order of  $10^3 D/U_\infty$  or higher, and characterized by a strong erratic character. Three major modes of fluctuations are identified by snapshot POD of the velocity fluctuations. A dominant mode  $m = 1$  is linked with anti-symmetric radial displacement of the inner backflow region close to the base, viz.  $x = 0.375 D$ , which evolves into a global wake displacement closer to the rear-stagnation point, viz.  $x \geq 0.75 D$ . At these stations an anti-symmetric mode  $m = 2$  can be identified with smaller-scale shear layer fluctuations, which induce a wake *ovalization*. An axisymmetric mode  $m = 0$  linked with streamwise pulsation of the backflow region is further identified at  $x = 0.375 D$ . Inspection of the spatial eigenmodes and analysis of the frequency spectra of the associated time-coefficients indicate that close to the base the anti-symmetric mode  $m = 1$  causes a backflow radial displacement at characteristic frequencies in the range  $St_D = 10^{-4} - 10^{-3}$ . For  $x \geq 0.75 D$  instead, it is found to induce a global wake displacement with characteristic frequency  $St = 10^{-1}$ .

It is shown that the low-frequency dynamics of the axisymmetric turbulent wake is dominated by the inner backflow meandering in proximity of the separation point



and by the fluctuations associated with the shear layer development closer to the rear-stagnation point.\*

---

\*This work has been published in Gentile *et al* (2016) *Physics of Fluids* **28**(6):065102.

## 5.1 Introduction

Turbulent wake flows past bluff bodies of revolution are of relevance for a variety of engineering systems, particularly in the context of transport industry, and have been the subject of numerous investigations (cf. Oertel 1990). A dominant feature of these flows is the large-scale shear layer unsteadiness arising at Reynolds numbers  $Re_D > 10^2$  as a result of growing unstable modes (Chomaz 2005). Notwithstanding the technical relevance of these axisymmetric wake configurations, notably for the high-Reynolds number turbulent regime, they appear to have received much less attention in comparison to nominally 2D configurations, such as the canonical case of the circular cylinder wake (Williamson 1996).

Experiments conducted on the turbulent wake flow behind a cylinder aligned with the freestream (Merz *et al* 1978 and Merz 1979) showed that the recirculating flow produces strong pressure fluctuations at the base. From further studies of Fuchs *et al* (1979) it emerged that such fluctuations are especially intense in the low-frequency regime corresponding to a diameter-based Strouhal number  $St_D \approx 0.2$  and appear in the form of large-scale anti-symmetric oscillations reflecting vortex shedding from alternating sides of the body. Such anti-symmetric oscillations have been later found to be a major feature of the wake of other more complex configurations, such as truncated cylinders with afterbody (Dépres *et al* 2004; Deck and Thorigny 2007).

Recent experimental studies conducted by Rigas *et al* (2014) on the turbulent wake of a slender blunt-based body of revolution revealed the existence of an additional important contribution of this anti-symmetric mode  $m = 1$  occurring at a significantly lower frequency of  $St_D \approx 0.002$  and reflecting a slow reorientation of the shedding plane and of the inner backflow region. This so-called *very-low-frequency* instability renders the wake topology asymmetric at all times, the axial symmetry being only restored upon sufficiently long-term averaging. Spheres (Grandemange *et al* 2014) and three-dimensional rectilinear bodies such as Ahmed bodies (Grandemange *et al* 2012b), have been shown to feature an analogous backflow behavior, whereby in the latter case it manifests as an irregular shift of the recirculation bubble between two preferred anti-symmetric states. Similarly, the stagnation point in the wake of turbulent annular jets is found to experience a large-scale precession motion with comparable characteristic time-scales (Vanierschot and Van den Bulck 2011).

The occurrence of such a backflow unsteadiness has been linked to the persistence in the fully turbulent regime of the symmetry-breaking mode (Grandemange *et al* 2014; Vanierschot and Van den Bulck 2011), with the prescribed symmetry plane continuously changing its orientation in view of its sensitivity to external perturbations (Grandemange *et al* 2012a; Rigas *et al* 2015). Asymmetries in the near-wake flows of axisymmetric bodies have been amply documented in literature (cf. Wolf *et al* 2012) and have been mainly ascribed to imperfect boundary conditions such as misalignments between wind tunnel model and freestream flow. Parametric studies conducted on truncated-base rocket models (Klei 2012; Wolf *et al* 2013) showed that the mean near-wake topology can be significantly

distorted by angular misalignments as small as  $0.3^\circ$ . While these results highlight the importance of a careful experimental setup in the investigation of such flows, the occurrence of a *very-low-frequency* backflow unsteadiness also imposes important constraints on the minimum required observation-time or computation-time in the context of numerical investigations.

The effects of the backflow unsteadiness on mean, instantaneous and fluctuating flow field have been documented for three-dimensional (Grandemange *et al* 2012b) as well as axisymmetric configurations (Rigas *et al* 2014; Grandemange *et al* 2014). To date, the influence of this instability on the azimuthal-radial wake topology has been discussed based on either pressure measurements performed on the base (Rigas *et al* 2014) or PIV measurements (Grandemange *et al* 2014) conducted in proximity of the rear-stagnation point. As a result, the streamwise evolution of the low-frequency unsteadiness of the wake has not been fully characterized yet.

The current study investigates the spatio-temporal dynamics of a turbulent axisymmetric wake in different azimuthal-radial planes. Wind tunnel experiments are conducted on the near-wake flow produced by an ogive-cylinder aligned with the freestream flow, for a Reynolds number  $Re_D = 67,000$ , based on the model diameter. Stereoscopic PIV measurements are performed in cross-flow planes evenly distributed in the streamwise direction such to encompass the near-wake development from the separation point until beyond the reattachment location. Snapshot POD (Sirovich 1987) analysis is conducted in order to examine the large-scale fluctuations dominating the near-wake dynamics.

## 5.2 Experimental setup

### 5.2.1 Flow facility and wind tunnel model

Experiments were conducted on the turbulent wake flow behind an ogive-cylinder geometry (Fig. 5.1) at a Reynolds number  $Re_D = 67,000$ , based on the model diameter. A detailed description of the flow facility and wind tunnel model can be found in section 3.1.

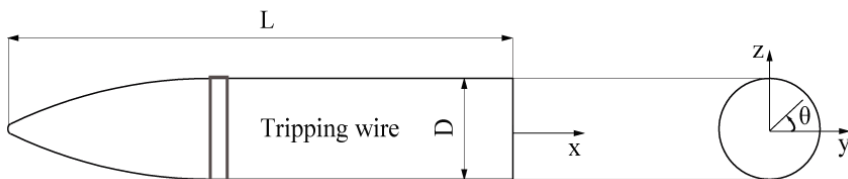
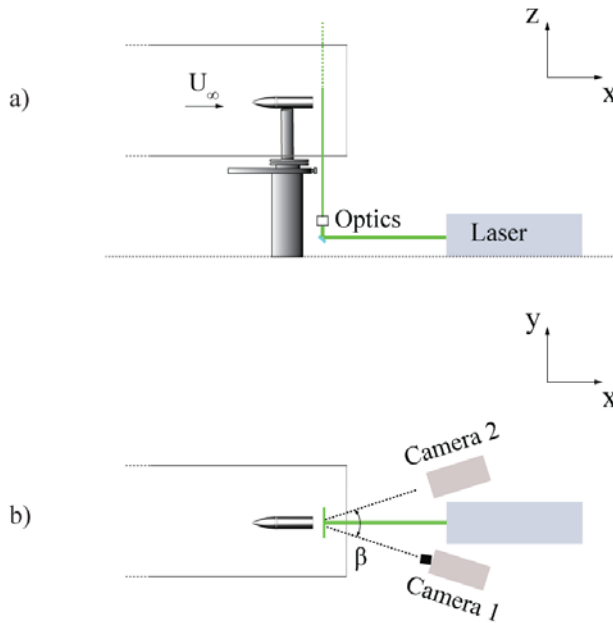


Figure 5.1 Schematic side and back view of the model with coordinate system.

### 5.2.2 Measurement apparatus and procedure

Stereoscopic PIV measurements were performed in azimuthal-radial planes located at  $x/D = \{0.375, 0.75, 1.125, 1.5\}$  such to encompass the near-wake development, based on a rear-stagnation point location  $x/D = 1.2$  (cf. chapter 4).



**Figure 5.2** Schematic layout of the experimental setup with illumination and imaging configuration. Side (a) and top view (b).

A Quantronix Darwin Duo Nd-YLF laser was used for illumination, whereas the recordings were performed with two Photron FastCAM SA1.1 CMOS cameras. The illumination and imaging setup are schematically illustrated in Fig. 5.2 below.

### 5.2.3 Data processing and assessment

An intensity normalization procedure (Adrian and Westerweel 2011) was applied to the images in order to reduce background intensity and reflections from the model surface. An iterative multi-grid cross correlation analysis based on window deformation (Scarano and Riethmuller 1999) was used for image interrogation, whereas spurious vectors were detected by means of a median filter (Westerweel and Scarano 2005). For further details on the data processing the reader is referred to subsection 3.2.1.

The average cross-correlation signal-to-noise ratio (SNR) was measured to be higher than 4 inside the wake, with a minimum of 1.5 in the shear layer region. Based on the latter values and on the relative size of the interrogation window, the

present measurements are considered suitable for the description of the large-scale wake dynamics, but not for the analysis of the shear layer fine-scale turbulence.

**Table 5.I Main stereoscopic PIV measurement settings**

Freestream velocity $U_\infty$	20 m/s
Diameter-based Reynolds number $Re_D$	67,000
Streamwise measurement planes $x/D$	0.375, 0.75, 1.125, 1.5
Laser sheet thickness $t$	3 mm
Laser pulse separation $\Delta t$	25 $\mu$ s
Cameras viewing angle $\beta$	35°
Objective f- number $f_\#$	2.8
FOV size	75 x 75 mm <sup>2</sup>
Image magnification $M$	0.16
Vector pitch	0.7 mm
Acquisition frequency $f_{acq}$	100 – 2000 Hz
Data ensemble size $N$	5000
Measurement duration $T$	2.5 - 50 s

An overview of the measurement uncertainty contributions affecting the present measurements is given in Table 5.II. For details on their mathematical definition the reader is referred to section 3.3.

**Table 5.II Overview of the main uncertainty contributions**

Instantaneous velocity uncertainty $\epsilon_{u'}/U_\infty$	1%
Statistical uncertainty $\epsilon_{\bar{u}}/U_\infty$	0.9%
Velocity fluctuations uncertainty $\epsilon_{u'}/\langle u' \rangle_{max}$	0.6%
Out-of-plane to in-plane velocity uncertainty (Prasad 2000)	3

### 5.3 Results

The present analysis is carried out for azimuthal-radial planes located at different streamwise stations along the model symmetry axis. Throughout the discussion model base diameter  $D$ , freestream velocity  $U_\infty$  and convective-time  $D/U_\infty$  are used as scaling parameters for spatial coordinates, velocities and time units respectively.

### 5.3.1 Flow Field Statistics

As a reference for the following discussion the statistical wake properties are first discussed in the longitudinal plane  $y = 0$ .

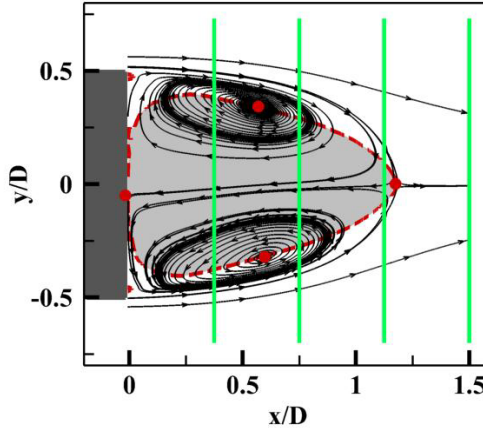


**Figure 5.3** Time-averaged streamlines in the plane  $y = 0$  (cf. Gentile *et al* 2016b). Foci and stagnation points in red. Backflow region in gray. PIV measurement planes in green.

The time-averaged streamlines obtained from the experiments discussed in chapter 4 (cf. Gentile *et al* 2016b) are shown Fig. 5.3 and define the separated region downstream of the trailing edge with a rear (or primary) stagnation point located approximately  $1.2 D$  away from the base and a secondary stagnation point located on the base close to the model axis. The separated flow features a toroidal recirculation region with foci at  $(x/D, r/D) = (0.60, 0.33)$ .

The mean velocity profiles obtained in this longitudinal plane at the stations of interest (Fig. 5.4a) give evidence of the streamwise thickening of the separated shear layer and of the concurrent shrinking of the reversed-flow region. Intense longitudinal and radial velocity fluctuations (Fig. 5.4b) are observed close to the separation point, which are associated with the turbulence of the separating shear layer. Moving away from separation the longitudinal fluctuations further develop with maxima along the mixing layer, reflecting the growth of the shear layer structures. The radial fluctuations instead, tend to intensify in the innermost region close to the model symmetry axis, reflecting the global instability of the inner backflow.

The streamwise development of the longitudinal velocity shows a good agreement with the literature (Merz *et al* 1978; Wolf *et al* 2012) in terms of both mean and RMS values. The backflow velocity is observed attaining a maximum of  $0.3 U_\infty$  at  $x/D = 0.7$ , which point corresponds to approximately 60% of the rear-stagnation point location (Fig. 5.5). Wolf (2012) and Wolf *et al* (2012) reported a slightly higher backflow peak (i.e.  $0.32 U_\infty$ ) at the same station, while Merz *et al* (1978) reported a

peak of  $0.35 U_\infty$ . The longitudinal fluctuations intensify moving away from the base and attain a maximum of  $0.18 U_\infty$  at  $x/D = 1$ .

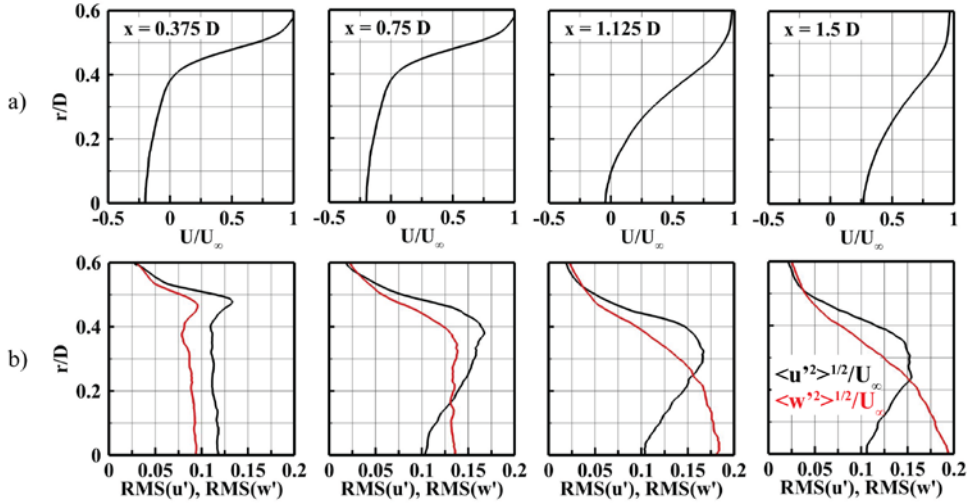


Figure 5.4 Radial velocity profiles at the measurement stations. Time-averaged longitudinal velocity (a). RMS of the fluctuating velocity (b).

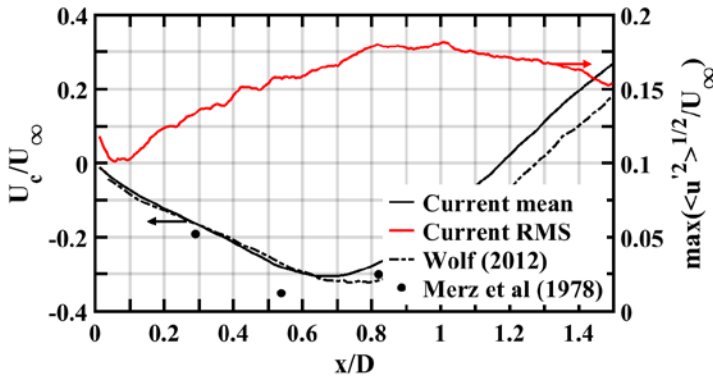
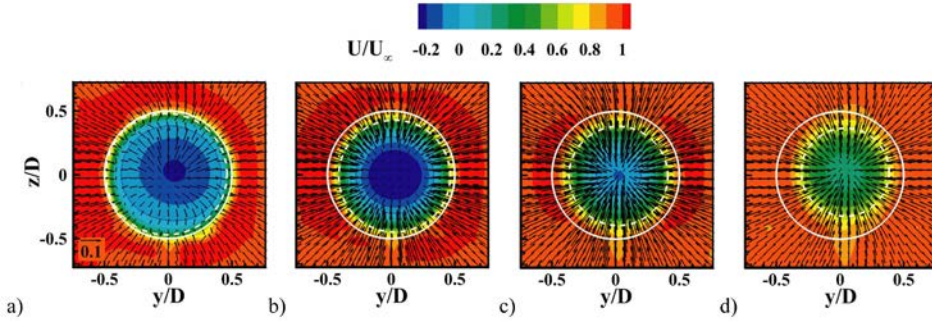


Figure 5.5 Streamwise distribution of the longitudinal velocity: mean centerline velocity (black) and maximum longitudinal RMS (red).

Fig. 5.6 shows the mean velocity field in the four azimuthal-radial measurement planes ( $y, z$ ). As a further evidence of the streamwise development of the near-wake, the mean radial location of the shear layer is super-imposed onto the color contours. The latter is obtained from projection of the point of inflection of the longitudinal velocity profiles on the azimuthal-radial plane (cf. Fig. 5.4a).

The contours of the mean out-of-plane velocity show a toroidal wake organization characterized by a circular shear layer bounding an inner region of reversed flow.

The in-plane velocity gives evidence of a source-like pattern at  $x/D = 0.375$  associated with the outward motion of the reverse flow in proximity of the stagnation point on the base. For  $x/D \geq 0.75$  instead, the convergence of the external streamlines gives rise to a sink-like pattern. As it will be discussed in the remainder of this chapter and as reported in recent investigations (Rigas *et al* 2014; Grandemange *et al* 2014), such zero-net vorticity patterns are typical of the current flow configuration and reflect an equal exploration over time of different asymmetric wake topologies by the backflow region. The center of the distribution features a slight shift towards the right, revealing the presence of residual misalignments and giving further evidence of their strong influence on the selection of the instantaneous wake orientation. The trace of the shear layer axis is found to move inwards from  $r/D = 0.48$  at  $x/D = 0.375$ , to  $r/D = 0.34$  at  $x/D = 1.5$ , reflecting the convergence of the outer streamlines towards the model axis and the consequent contraction of the wake cross-section.



**Figure 5.6** Time-averaged velocity field in the plane  $(y, z)$ .  $x = 0.375 D$  (a),  $x = 0.75 D$  (b),  $x = 1.125 D$  (c) and  $x = 1.5$  (d). Color coded out-of-plane component. Vectors plotted every 5th grid-point represent in-plane components  $V/U_\infty$  and  $W/U_\infty$ . Model edge in solid white. Mean shear layer axis in dashed white. Total observation-time is  $20,000 D/U_\infty$ .

A velocity defect between 5% and 10% of the freestream velocity, depending on the measurement location, can be observed in the lower hemisphere of the separated region and is ascribed to the presence of the model mounting. Velocity defects up to  $0.15 U_\infty$  are reported in literature to be associated with significant wake asymmetries (Wolf *et al* 2010; Wolf 2012) and have been linked with the onset of preferred azimuthal periodicities (Grandemange *et al* 2012).

The spatial distributions of the normalized turbulence intensity defined as

$$\frac{TI}{U_\infty} = \frac{1}{U_\infty} \sqrt{\frac{\langle u'^2 \rangle + \langle v'^2 \rangle + \langle w'^2 \rangle}{2}} \quad (5.1)$$

and presented in Fig. 5.7 further show the streamwise increase in the turbulent fluctuations associated with the shear layer development. Asymmetries can be appreciated in the distributions, which appear more pronounced than those observed in the previous



mean velocity distributions (cf. Fig. 5.6). The latter are regarded here as a further evidence of the effects of the long-term backflow meandering on the mean wake topology and further hint at a minor model misalignment with respect to the incoming flow.

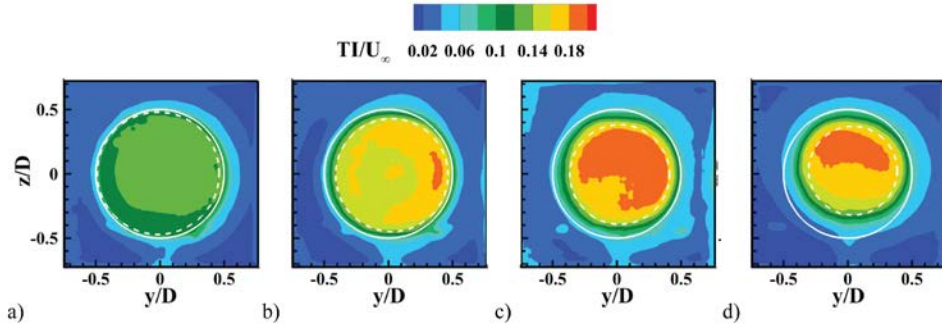


**Figure 5.7** Turbulence intensity distribution in the plane  $(y, z)$ .  $x = 0.375 D$  (a),  $x = 0.75 D$  (b),  $x = 1.125 D$  (c) and  $x = 1.5$  (d). Color coded out-of-plane component. Model edge in solid white. Mean shear layer axis in dashed white. Total observation-time is  $20,000 D/U_\infty$ .

### 5.3.2 Instantaneous flow field analysis

Sets of PIV snapshots are herein inspected to retrieve information on the temporal evolution of the near-wake flow. As the backflow behavior is of particular interest, the discussion is herein restricted to time-uncorrelated snapshots obtained upstream of the rear-stagnation point, namely at  $x/D = 0.375$ ,  $x/D = 0.75$  and  $x/D = 1.125$ .

At the most upstream station, viz.  $x/D = 0.375$  (Fig. 5.8a), the instantaneous velocity field renders a nearly circular wake topology, with minor corrugations of the external perimeter being ascribed to the turbulence of the separating boundary layer. This is reflected in the shear layer axis being almost coincident with the trace of the model base. The flow outside the wake appears unperturbed with respect to the freestream conditions. In contrast, the inner backflow region is observed experiencing vigorous fluctuations involving azimuthal meandering over time and substantial radial offset (i.e. approximately half a base radius) from the mean wake axis. The in-plane velocity vectors indicate a correlation between outwards in-plane motion and maximum backflow intensity. This fluctuating pattern reflects the instability of the stagnation point on the base, whose tendency is to be located away from the wake axis (the reader is referred to Fig. 5.14 for a schematic illustration of the latter situation). Given the axial symmetry of the problem, a stable condition is not expected to depend upon the specific azimuthal position, which fact explains the azimuthal meandering of the backflow observed in the snapshots.

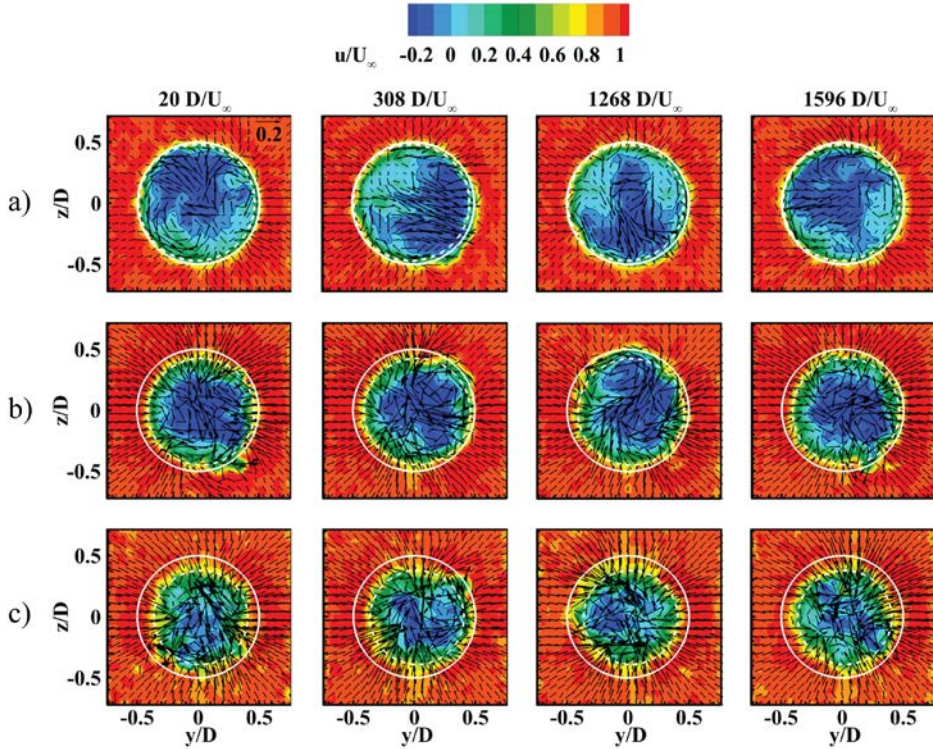


**Figure 5.8** Instantaneous velocity field in the plane  $(y, z)$ .  $x = 0.375 D$  (a),  $x = 0.75 D$  (b),  $x = 1.125 D$  (c). Color coded out-of-plane component. Vectors plotted every 5th grid-point represent in-plane components  $v/U_\infty$  and  $w/U_\infty$ . Model edge in solid white. Mean shear layer axis in dashed white. Cf. Gentile *et al* (2016a) for corresponding animations.

More significant corrugations of the external wake perimeter are observed moving downstream at  $x/D = 0.75 D$  (Fig. 5.8b). Such corrugations are attributed to the interactions between the flow inside and outside the separated region. Those interactions emerge from the in-plane flow pattern and involve localized intrusions of high-speed fluid from outside the wake and eruptions of low-speed fluid from inside the wake, which also involve the inner backflow region. Fluctuations of the backflow region along the azimuth are still observable. However, the motion appears confined in proximity of the wake geometric center, reflecting the vanishing effect of the adverse pressure gradient away from the base region. In proximity of the rear-stagnation point, viz. at  $x/D = 1.125$  (Fig. 5.8c), the distortion of the wake perimeter becomes more pronounced as the interaction between wake and outer flow tends to involve almost the entire wake perimeter.

The azimuthal backflow meandering emerges from the previous discussion as a large-scale mode of fluctuation, which displaces the backflow region with respect to the so-called nominal axisymmetric position (cf. Fig. 5.6). This mode has been documented

for a similar configuration by Rigas *et al* (2014) based on base pressure measurements. In the present work it is discussed by examining the instantaneous position of the backflow centroid in relation to the wake topology, following the same approach shown in Grandemange *et al* (2012b). In order to examine the backflow centroid position in relation to the near-wake topology, a sliding-average operation is applied over a time-interval of  $40 D/U_\infty$  (i.e. 0.1 s, corresponding to 10 snapshots acquired at 100 Hz).

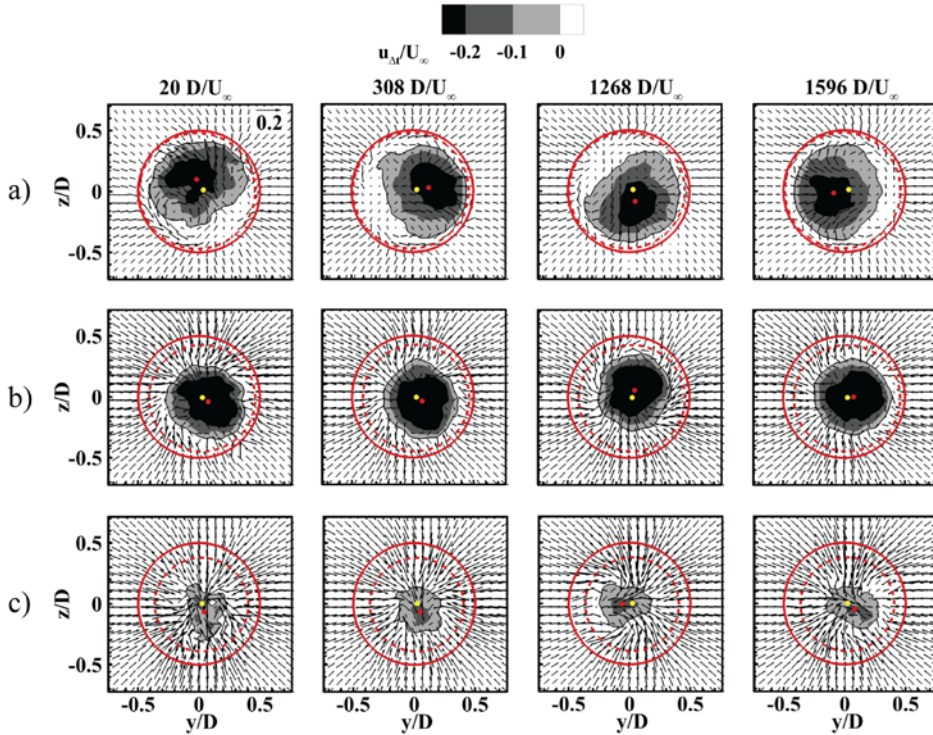


**Figure 5.9** Short-time-averaged ( $\Delta t = 40 D/U_\infty$ ) velocity field in the plane  $(y, z)$ .  $x = 0.375 D$  (a),  $x = 0.75 D$  (b),  $x = 1.125 D$  (c). Gray level coded out-of-plane component. Vectors plotted every 5th grid-point represent in-plane components  $v/U_\infty$  and  $w/U_\infty$ . Model edge in solid red. Mean shear layer axis in dashed red. Short-time averaged backflow centroid in red. Long-time averaged backflow centroid in yellow. Cf. Gentile *et al* (2016a) for corresponding animations.

This operation allows for filtering the small-scale fluctuations, while capturing the characteristic time-scales of the global mode (i.e.  $10^3 D/U_\infty$  according to Rigas *et al* 2014). Following the approach of Grandemange *et al* (2012b) the instantaneous position of the backflow centroid is extracted from the sliding-averaged velocity field as

$$y_c = \frac{\iint u^-(y, z) \cdot z dy dz}{\iint u^-(y, z) dy dz} \quad (5.2)$$

$$z_c = \frac{\iint u^-(y, z) \cdot y dy dz}{\iint u^-(y, z) dy dz} \quad (5.3)$$

The short-time averaged position of the backflow centroid thus obtained is superimposed onto the backflow velocity contours in Fig. 5.9 (red dot) along with the reference time-averaged position (yellow dot). The low-pass filtering of the small-scale turbulence to which the minor corrugations of the wake perimeter were previously ascribed (cf. Fig. 5.8a) returns a smoother velocity field and further highlights the radial offset between the instantaneous and the long-time-averaged position of the backflow centroid.

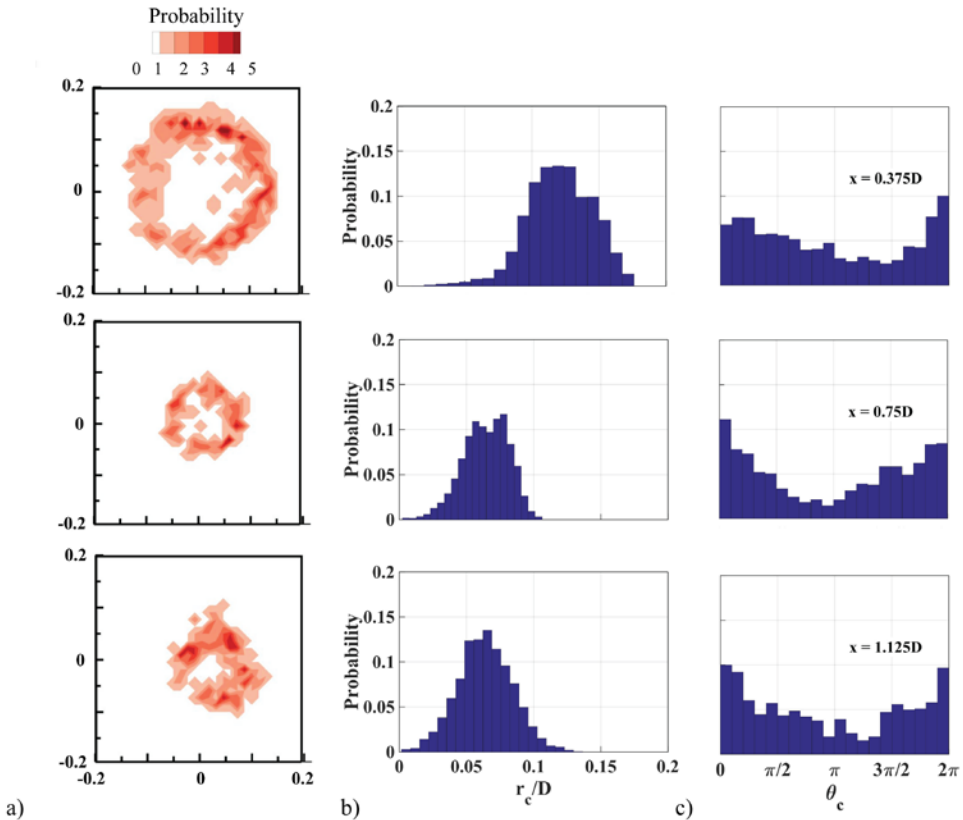


**Figure 5.10** Probability distributions of the backflow centroid position. Two-dimensional distributions in the azimuthal plane (a). One-dimensional distributions in the radial direction (b) and in the azimuthal direction (c). Total observation-time is  $20,000 D/U_\infty$ .

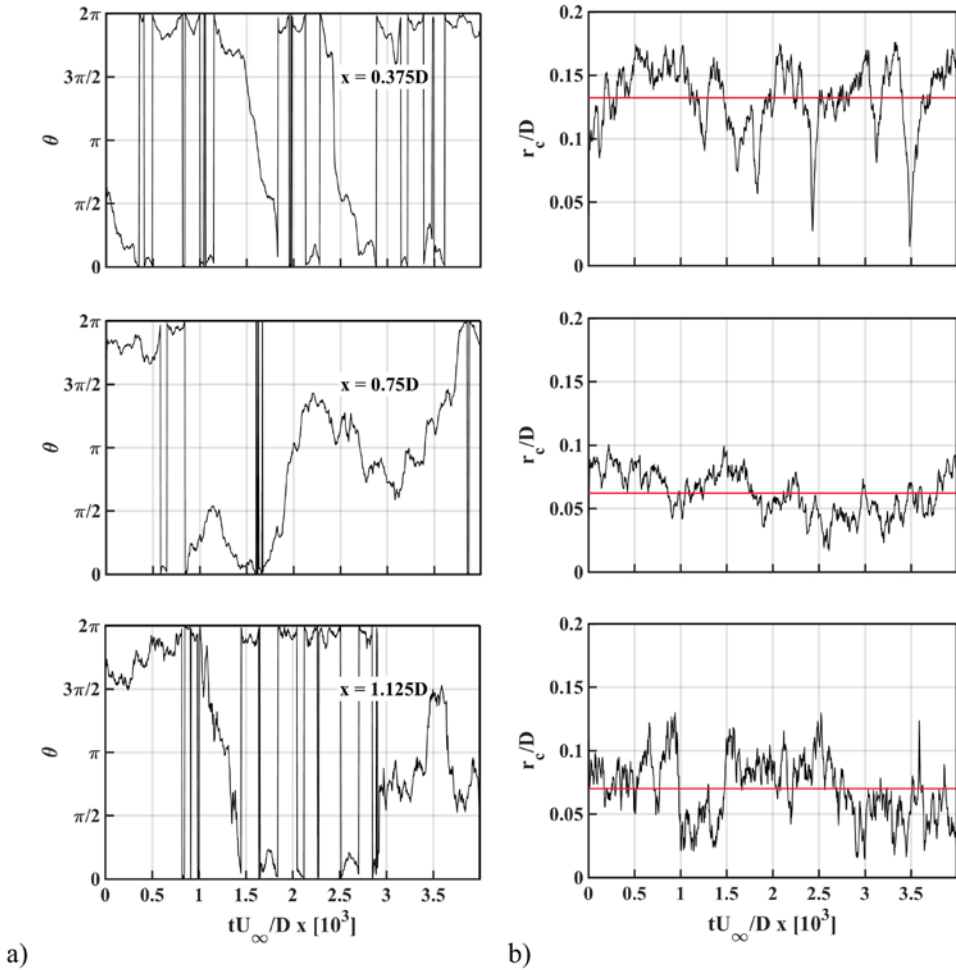


**Figure 5.11** Time-history of the backflow centroid position. Azimuthal coordinate (a). Radial coordinate (b). Total observation-time is  $4,000 D/U_\infty$ .

The radial offset between short-time averaged and long-time averaged backflow centroid appears to be approximately constant over time at all streamwise positions, whereas the azimuth varies over time. The radial offset is observed decreasing from a maximum of  $0.13 D$  at  $x/D = 0.375$  to a minimum of  $0.05 D$  attained at  $x/D = 0.75$ , which location is associated with the maximum backflow intensity in the current study, and to slightly increase again to  $0.08 D$  in proximity of the rear-stagnation point, viz. at  $x/D = 1.125$ . The in-plane velocity vectors indicate that the azimuthal backflow meandering is associated with lateral fluid motions inside the wake. In particular, at the most upstream position of  $x/D = 0.375$ , the region of maximum backflow exhibits consistently an outward motion, corresponding to positive radial

velocity and two weak circulatory regions with little to no backflow. Moving downstream to  $x/D \geq 0.75$  the inner backflow appears less coherently organized and no clear correlation between backflow position and in-plane velocity pattern can be inferred.

The two-dimensional probability distributions of the backflow centroid position over an observation-time  $20,000 D/U_\infty$  (i.e. 50 s) define an approximately circular pattern, reflecting the azimuthal meandering of the recirculation bubble (Fig. 5.10). The occurrences over the azimuth are rather uniform, yielding a long-time averaged axisymmetric pattern (cf. Fig. 5.6). This result is in good agreement with the works of Rigas *et al* (2014) and Grandemange *et al* (2014), who report the axisymmetry of the near-wake topology as a mere long-term statistical property of the turbulent wake. The one-dimensional probability distributions outline a shift of the most probable radial coordinate from  $0.12 D$  at  $x/D = 0.375$  to  $0.08 D$  and  $0.07 D$  at  $x/D = 0.75$  and  $x/D = 1.125$ , respectively. This shift indicates that the backflow precession motion reduces in amplitude and coherence while moving away from the base, while the shear layer development tends to dominate the near-wake dynamics. The higher probability value observed at  $\theta = 0$  appears to correlate with the offset previously observed in Fig. 5.6, thus being attributed to a small model misalignment with respect to the freestream flow.

The time-history of the backflow centroid over a portion of the available observation-time corresponding to  $4,000 D/U_\infty$  (i.e. 10 s) is presented in Fig. 5.11. The time-evolution of the radial coordinate at  $x/D = 0.375$  gives evidence of a pronounced intermittency of the backflow motion, which is characterized by excursions about the average radial offset of  $0.12 D$ . Similar fluctuations are also observed in proximity of the reattachment, viz. at  $x/D = 1.125$ , in which case the average radial offset reduces to about  $0.07 D$ . While at the most upstream station this erratic character reflects the instability of the reversed flow, in proximity of the reattachment it is rather to be ascribed to the global wake distortion associated with the shear layer large-scale fluctuations (cf. Figg. 5.8c and 5.9c).

The time-history of the azimuthal coordinate outlines a quasi-periodic motion at  $x/D = 0.375$ , characterized by time-scales of approximately  $1,000 D/U_\infty$ , corresponding to non-dimensional frequencies in the order of  $St \sim 10^{-3}$ . Although less regular, an analogous azimuthal motion can be also observed at  $x/D = 0.75$ , with even longer characteristic time-scales (i.e.  $3,000 D/U_\infty$ ), corresponding to frequencies in the order of  $St \sim 3 \cdot 10^{-4}$ . No evidence of such semi-periodic fluctuations is given at  $x/D = 1.125$ , which further shows the vanishing coherence of the backflow fluctuations.

### 5.3.3 Proper orthogonal decomposition

The large-scale velocity fluctuations dominating the near-wake dynamics are examined based on snapshot POD analysis (Sirovich 1987). Details on the adopted mathematical procedure are provided in section 3.4 of the present dissertation.

The spectra illustrating the individual energy contributions obtained from the decomposition (Fig. 5.12) indicate that typically between 40% to 50% of the turbulent kinetic energy

of the flow is captured within the first 10 modes, depending on the streamwise station, with a notably faster energy convergence at the most upstream station (i.e.  $x/D = 0.375$ ).

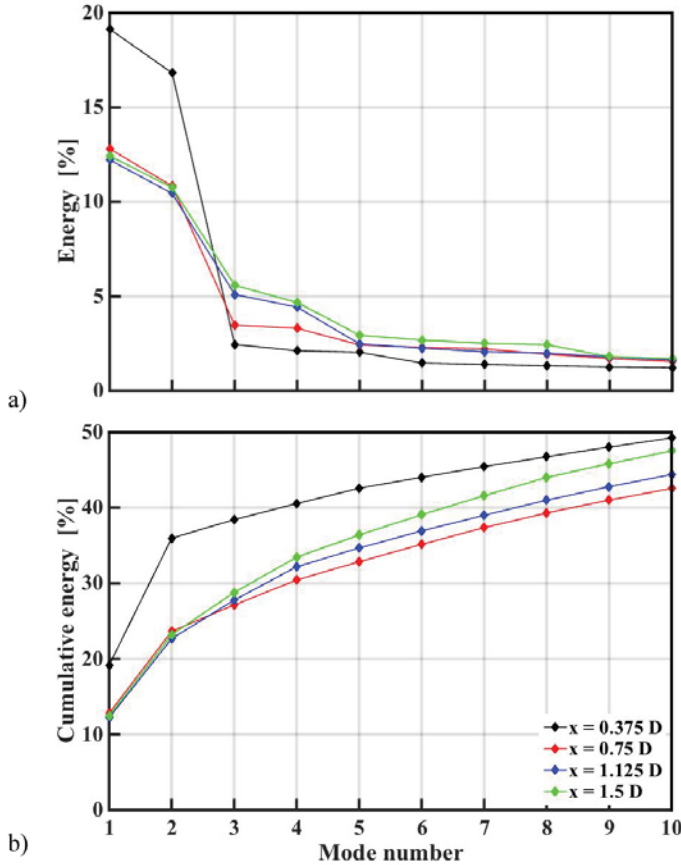


**Figure 5.12** Energy distribution over the POD modes. Individual energy contributions (a). Cumulative energy contributions (b).

More specifically, the cumulative energy contribution of the first two POD modes  $k = 1$  and  $k = 2$  varies between 37% and 23% when moving away from the model base. The energy contributions as well as the spatial distributions of the two modes, which are found to be in azimuthal phase quadrature (cf. Fig. 5.13), suggest that they are dynamically paired. A further mode pair can be identified at  $x \geq 0.75 D$  with modes  $k = 3$  and  $k = 4$ , each capturing between 4% and 6% of the energy, depending on the measurement location (cf. Fig. 5.12). The latter contributions in particular, are found to grow in importance when moving in the downstream direction reflecting the decreasing large-scale organization of the flow.

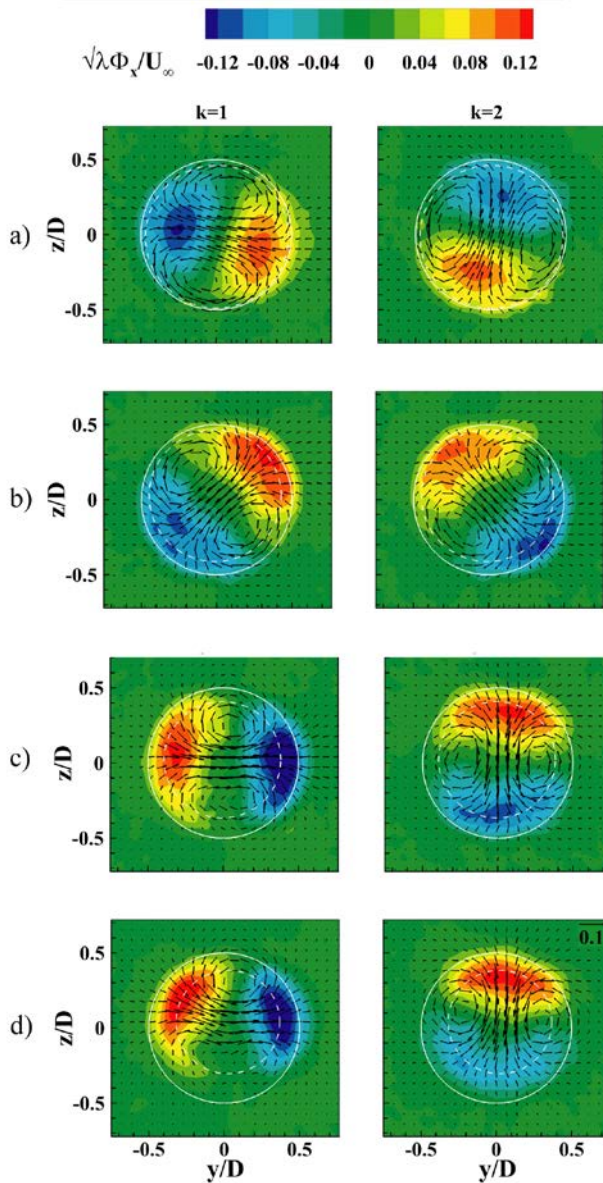


Figure 5.13 POD modes  $k = 1$  and  $k = 2$ .  $x = 0.375 D$  (a),  $x = 0.75 D$  (b),  $x = 1.125 D$  (c) and  $x = 1.5$  (d). Color coded out-of-plane component. In-plane vectors plotted every 5th grid point represent in-plane components  $\sqrt{\lambda_k} \Phi_{k,y} / U_\infty$  and  $\sqrt{\lambda_k} \Phi_{k,z} / U_\infty$ . Base edge in solid white. Mean shear layer axis in dashed white.

This mode pair is not identifiable at the most upstream station  $x = 0.375 D$  where instead, three modes, namely  $k = 3, 4$ , and  $5$  are found to capture similar amounts of



energy, viz. about 3% of the flow energy budget. A more detailed discussion of the higher order modes will follow later in the text.

The spatial distribution of the first two POD eigenfunctions is examined to assess the spatial coherence of the most energetic fluctuations occurring in the near-wake. The contours shown in Fig. 5.13 define a *dipole* distribution comprising two diametrically opposite regions of excess and defect of streamwise momentum respectively, whereby the linear combination of the two modes represents a radial displacement of the backflow region in any azimuthal direction.

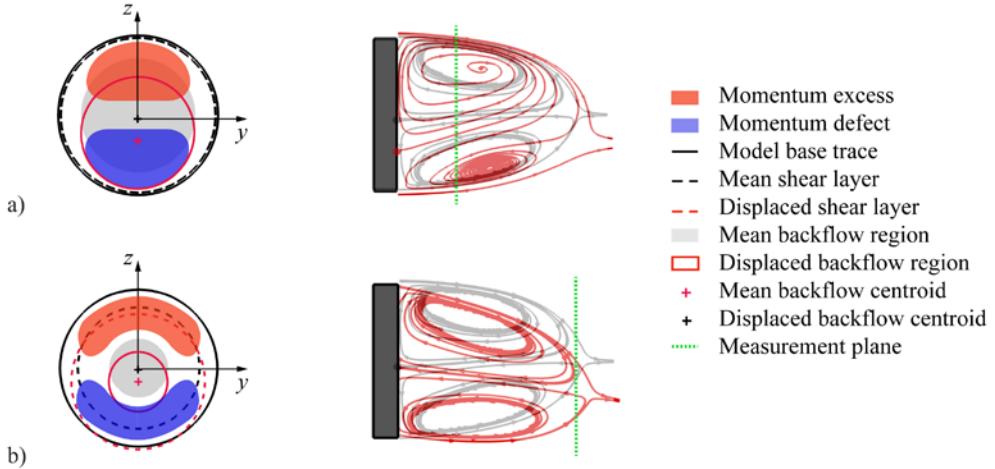


**Figure 5.14** Schematic interpretation of modes  $k = 1$  and  $k = 2$ . Inner backflow displacement close to the base (a). Global wake displacement close to the rear-stagnation point (b).

Such a dipolar organization has been identified by Rigas *et al* (2014) as an anti-symmetric mode of azimuthal wave-number  $m = 1$ . At  $x/D = 0.375$  the highest fluctuations are observed in the innermost portion of the wake and can be ascribed to the precession of the backflow region, whereas more downstream the maxima are attained along the mixing layer region and reflect the localized inrush of the outer high momentum flow towards the separated region, which was previously inferred from Fig. 5.8b-c. It can be argued that the anti-symmetric mode  $m = 1$  evolves in the streamwise direction reflecting radial displacement of the backflow region close to the separation point and of the entire wake closer to the reattachment.

These two situations are schematically depicted in Fig. 5.14. In particular, the former one (Fig.5.14a) is herein interpreted as a radial displacement of the backflow region with respect to the time-averaged position in the azimuthal-radial plane (left), which distorts the flow pattern in the longitudinal plane (right) without affecting the outer wake perimeter. The second situation (Fig. 5.14b) instead, is depicted as a global radial displacement of the wake, which involves both the shear layer axis and the backflow region in the azimuthal-radial plane and can be visualized as a vertical

displacement of the entire wake in the longitudinal plane. In both cases, two diametrically opposite regions of defect and excess of streamwise momentum are created (cf. Fig. 5.13). The literature has widely reported the second situation, which is commonly referred to as shear layer *flapping mode* (cf. Wolf *et al* 2012; Schrijer *et al* 2014), whereas the first one has been only recently identified with a significant contribution of the anti-symmetric mode  $m = 1$  (Rigas *et al* 2014).

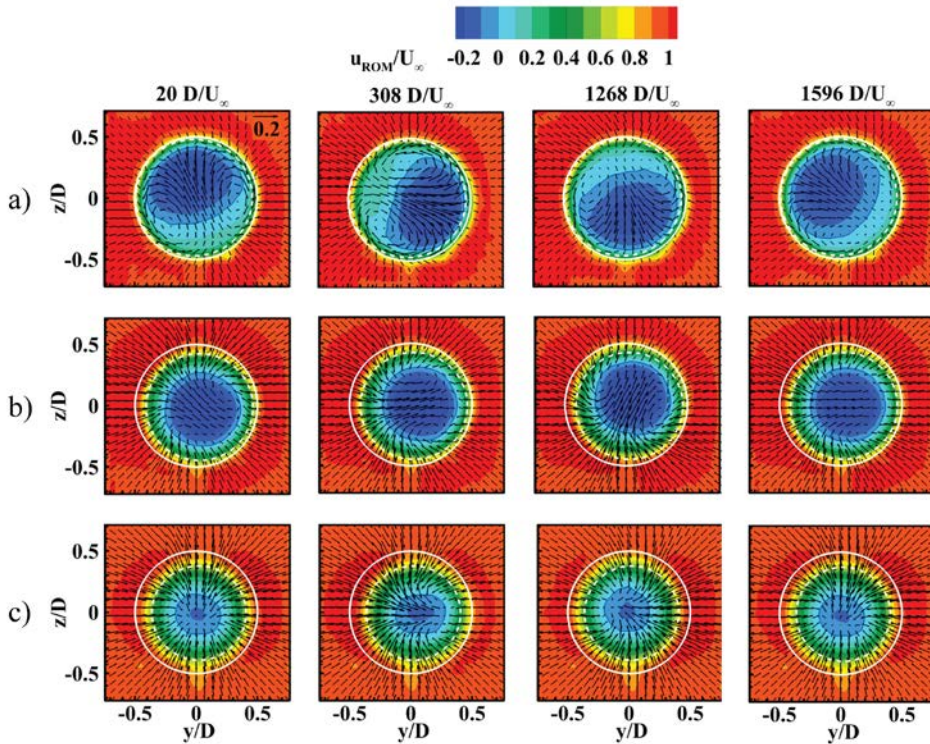


**Figure 5.15** ROM of the velocity field based on POD modes  $k = 1$  and  $k = 2$ .  $x = 0.375 D$  (a),  $x = 0.75 D$  (b) and  $x = 1.125 D$  (c). Color coded out-of-plane component. Vectors plotted every 5th grid-point represent in-plane components  $v_{ROM}/U_\infty$  and  $w_{ROM}/U_\infty$ . Base edge in solid white. Mean shear layer axis in dashed white. Cf. Gentile *et al* (2016a) for corresponding animations.

The low-order reconstruction of the velocity field based on the first two modes  $k = 1, 2$  is presented in Fig. 5.15 for the stations  $x/D = 0.375$ ,  $x/D = 0.75$  and  $x/D = 1.125$ . The low-order reconstruction has been derived according to the methodology illustrated in section 3.4 of the current dissertation. The snapshots refer to the same time-instants previously considered in Figs. 5.8 and 5.9. The reconstructed velocity field gives evidence of the purely displacing effect of the anti-symmetric mode  $m = 1$  acting on the inner backflow region at  $x/D = 0.375$  and on the whole separated region for  $x/D \geq 0.75$ . At this location, the in-plane vectors outline the interaction between the flow inside and outside the wake. It can be

noticed that both the POD spatial eigenfunctions and the reconstructed velocity fields feature the presence of in-plane vortical structures, which are identified as the trace of streamwise vortices. Recent studies (Grandemange *et al* 2014) have linked the latter with the thread vortices ensuing from the symmetry-breaking mode.

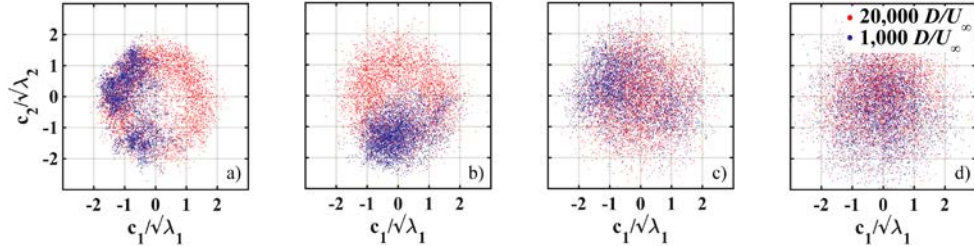


**Figure 5.16** Scatter plot of the POD time-coefficients  $c_1(t)$  and  $c_2(t)$ .  $x = 0.375 D$  (a),  $x = 0.75 D$  (b),  $x = 1.125 D$  (c) and  $x = 1.5 D$  (d). Red dots represent data acquired over  $20,000 D/U_\infty$ . Blue dots represent data acquired over  $1,000 D/U_\infty$ .

The temporal information on the characteristic time-scales of modes  $k = 1$  and  $k = 2$  is retrieved through analysis of the associated POD time-coefficients. Figure 5.16 shows the scatter plots of first and second POD time-coefficients obtained at the different measurement planes. Both low and high-repetition rate measurements are shown in order to highlight the influence of the time-scales of the unsteadiness on the wake topology. A remarkable difference can be appreciated between the distributions obtained over the long and the short observation-time,  $20,000 D/U_\infty$  (i.e. 50 s) and  $1,000 D/U_\infty$  (i.e. 2.5 s) respectively. The visible anisotropy of the short-term distributions (blue) reflects the dominance of the long-term meandering at  $x/D \leq 0.75$ , whereas the more diffused symmetrical pattern observed in proximity of the rear-stagnation point documents the shorter time-scales of the wake dynamics, which are also averaged-out in the short-term statistics.

The power spectral density distributions of the first two POD time-coefficients are presented in Fig. 5.17. Low and high-repetition rate measurements are combined, thus covering approximately four decades of the frequency spectrum. The spectra obtained at  $x/D = 0.375$  are dominated by a large contribution in the frequency range  $St_D = 0.0003 - 0.0005$ , which appears gradually decreasing when moving downstream.

This main *very-low-frequency* peak is representative of the backflow centroid dynamics. Its time-scales are consistent with those previously inferred from Fig. 5.11 and are in good agreement with the characteristic frequencies identified by Rigas *et al* (2014) and Grandemange *et al* (2012b). A second less significant contribution is displayed at  $St_D = 0.001$  and is found to be present at all measurement locations. A comparatively smaller contribution associated with vortex shedding is present at  $St_D = 0.2$  and is found to become more important while moving in the downstream direction, reflecting the shear layer growth.

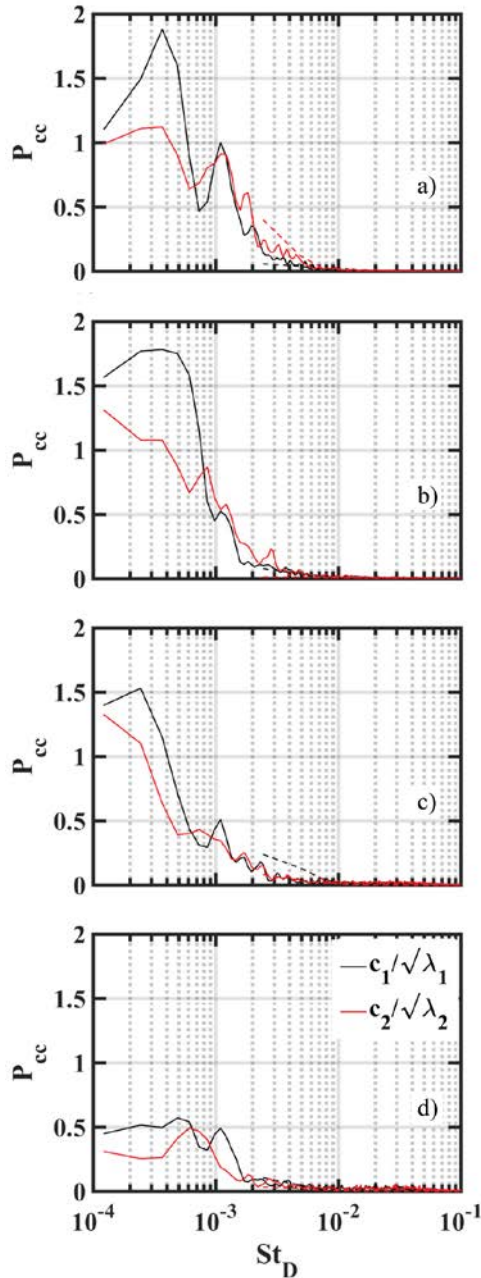
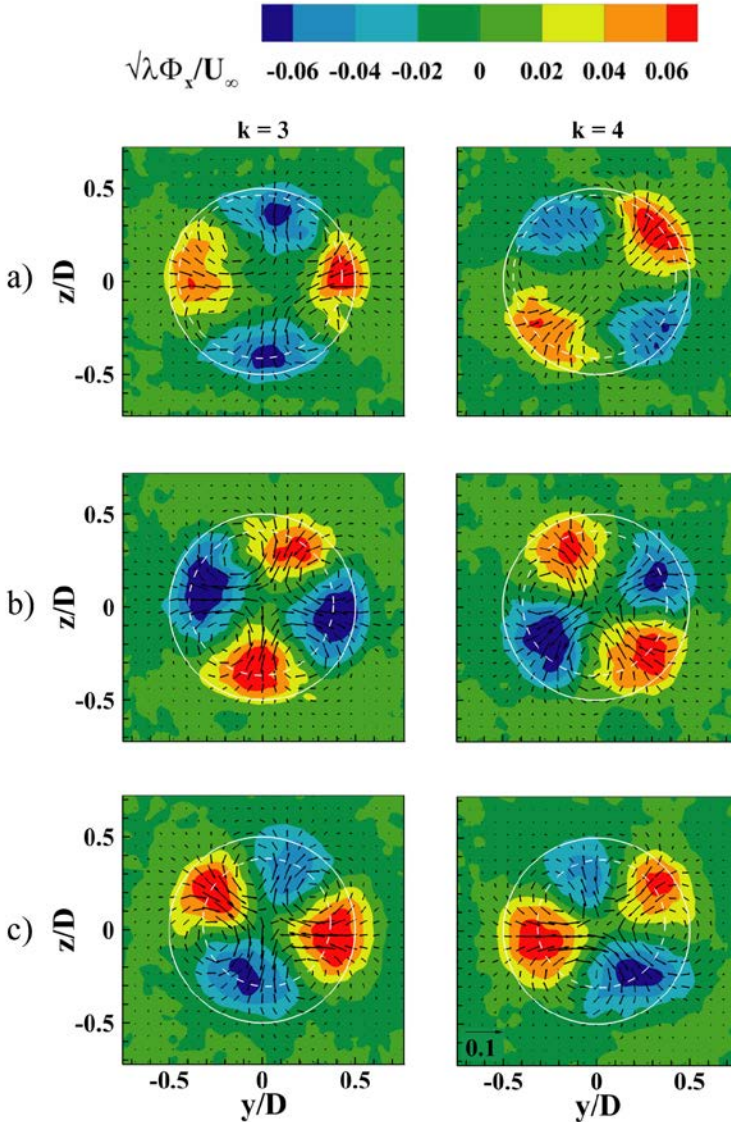
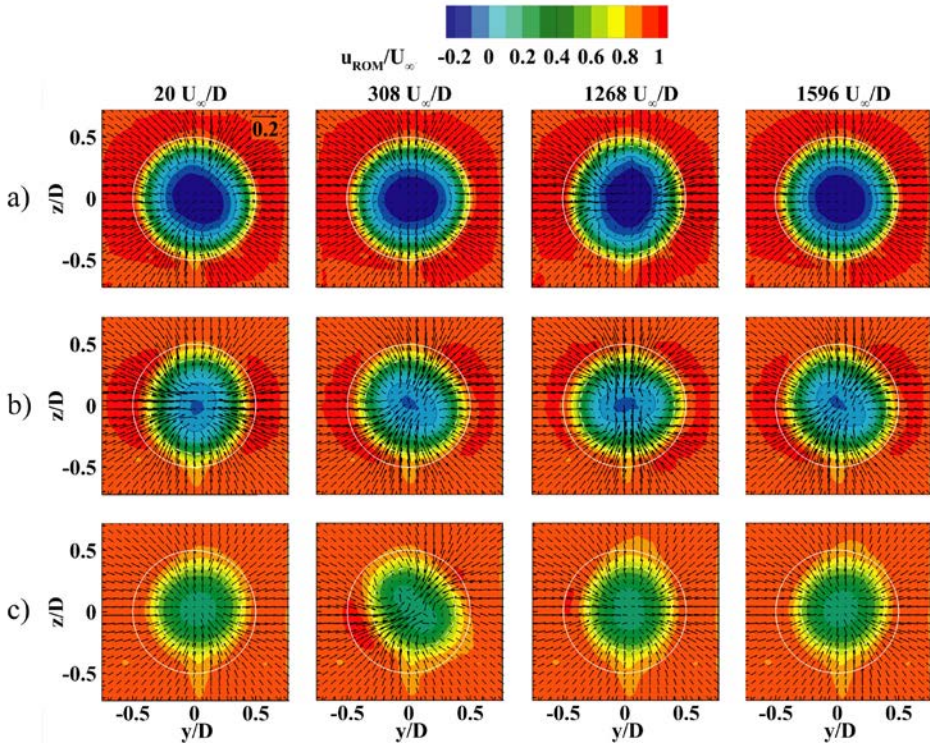


Figure 5.17 Power spectral density distributions of the POD time-coefficients  $c_1(t)$  and  $c_2(t)$ .  $x = 0.375 D$  (a),  $x = 0.75 D$  (b),  $x = 1.125 D$  (c) and  $x = 1.5 D$  (d). Solid line indicates data acquired at 100 Hz. Dashed line indicates data acquired at 2 kHz.

The analysis is concluded with the discussion of the higher order modes with  $k \geq 3$ . The spatial distributions in Fig. 5.18 indicate dynamical pairing of modes  $k = 3$  and  $k = 4$  at  $x/D \geq 0.75$ . Their linear combination allows for a rotation of the pattern in all azimuthal directions.



**Figure 5.18** POD modes  $k = 3$  and  $k = 4$ .  $x = 0.75 D$  (a),  $x = 1.125 D$  (b) and  $x = 1.5$  (c). Color coded out-of-plane component. In-plane vectors plotted every 5th grid point represent in-plane components  $\sqrt{\lambda_k} \Phi_{k,y} / U_\infty$  and  $\sqrt{\lambda_k} \Phi_{k,z} / U_\infty$ . Base edge in solid white. Mean shear layer axis in dashed white.



**Figure 5.19** ROM of the velocity field based on POD modes  $k = 3$  and  $k = 4$ .  $x = 0.75 D$  (a),  $x = 1.125 D$  (b) and  $x = 1.5 D$  (c). Color coded out-of-plane component. Vectors plotted every 5th grid-point represent in-plane components  $v_{ROM}/U_\infty$  and  $w_{ROM}/U_\infty$ . Base edge in solid white. Mean shear layer axis in dashed white. Cf. Gentile *et al* (2016a) for corresponding animations.

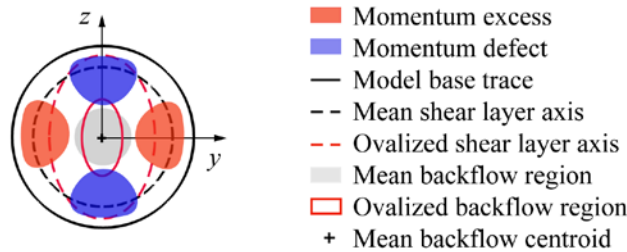


**Figure 5.20** Schematic interpretation of modes  $k = 3$  and  $k = 4$  at  $x \geq 0.75 D$ .

The two modes feature four regions of excess and defect of streamwise momentum. These regions are distributed along the external wake perimeter in a *quadrupolar* fashion. The in-plane vectors connecting the centers of the red and blue lobes define four in-plane vortical structures with a central saddle point. This alternating inward and outward in-plane pattern can be linked with a wake ovalization. The maxima are

attained along the mixing layer and an increase in coherence can be observed departing from the base, which suggests that modes  $k = 3$  and  $k = 4$  can be identified with a higher order mode of fluctuation of the shear layer.

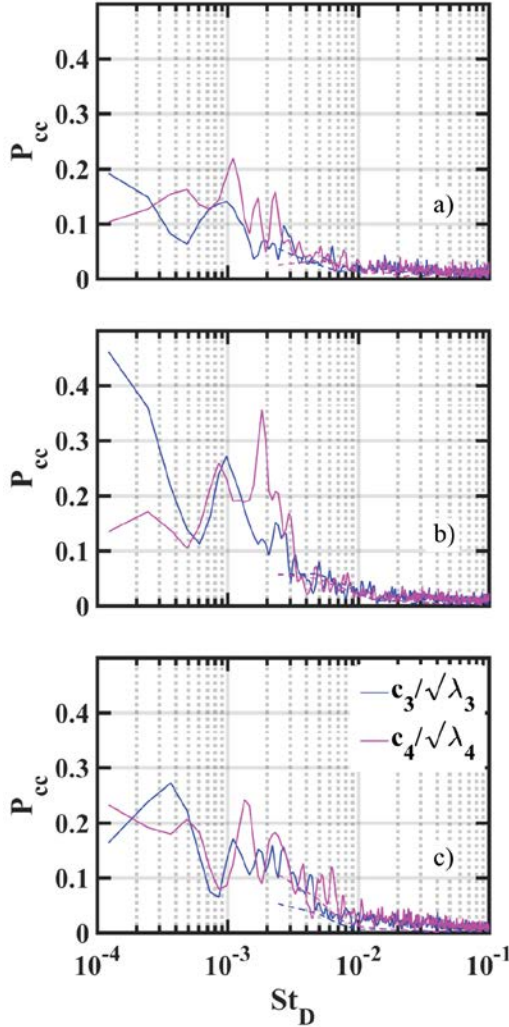


**Figure 5.21** Power spectral density distributions of the POD time-coefficients  $c_3(t)$  and  $c_4(t)$ .  $x = 0.75 D$  (a),  $x = 1.125 D$  (b), and  $x = 1.5 D$  (c). Solid line indicates data acquired at 100 Hz. Dashed line indicates data acquired at 2 kHz.

A similar spatial organization has been identified by Rigas *et al* (2014) as a mode of azimuthal wave-number  $m = 2$ . In the present investigation such a mode is attributed to the wake interaction with the outer flow, which entails inrush of high momentum fluid from two opposite sides of the wake and causes an outward motion

of low-momentum fluid in the orthogonal direction with creation of a saddle region in the center.

The low-order reconstructions of the velocity field based on third and fourth modes, namely  $k = 3$  and  $4$  are presented in Fig. 5.19 for  $x/D \geq 0.75$ . The reconstructed velocity field renders a visibly elongated wake perimeter compared to the axisymmetric time-averaged velocity field (cf. Fig. 5.6). The principal axes of the distorted wake are coherent with the inrush and ejection regions, whose combination represents four streamwise vortices. A schematic illustration of the effects of this second mode pair on the wake is shown in Fig. 5.20. The power spectral density distributions of third and fourth time-coefficients are shown in Fig. 5.21. Despite the larger data scatter with respect to the spectra associated with the first mode pair, a maximum can still be identified in the low-frequency regime at  $St_D \sim 10^{-3}$ .

The distributions of the spatial eigenmodes  $k = 3, 4$ , and  $5$  identified at the most upstream plane  $x/D = 0.375$  are presented in Fig. 5.22. The color contours of mode  $k = 4$  define a *quadrupole*, which shows some analogy with the structure of the second mode pair identified at  $x/D \geq 0.75$ . Unlike the latter case however, the peaks are observed within the shear layer axis, thus suggesting the occurrence of an ovalization involving the inner backflow region. Both modes  $k = 3$  and  $k = 5$  exhibit a central region of excess (defect) of streamwise momentum and two outer and diametrically opposite lobes of defect (excess) of streamwise momentum.

The central region can be linked to a streamwise pulsation of the inner backflow region, so-called bubble pumping. This distribution can be identified with an axisymmetric mode of azimuthal wave number  $m = 0$ , in analogy to what previously reported by Rigas *et al* (2014). The outer lobes of the two modes however, exhibit a phase quadrature relation, suggesting that the dynamics of this mode also features an additional contribution of ovalization.

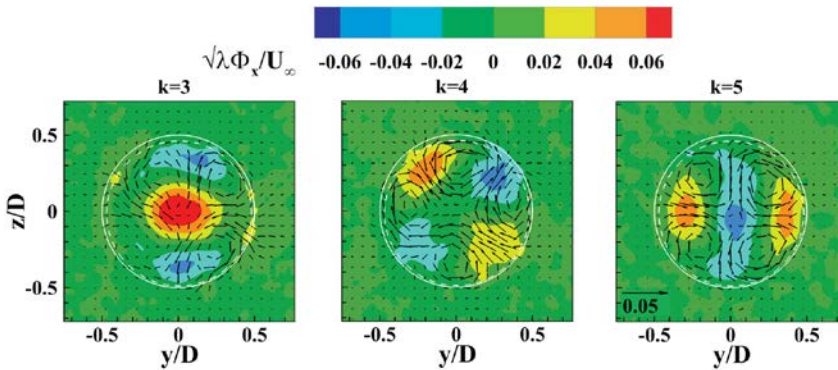


**Figure 5.22** POD modes  $k = 3$ ,  $k = 4$  and  $k = 5$  at  $x = 0.375D$ . Color coded out-of-plane component. In-plane vectors plotted every 5th grid point represent in-plane components  $\sqrt{\lambda_k} \Phi_{k,y} / U_\infty$  and  $\sqrt{\lambda_k} \Phi_{k,z} / U_\infty$ . Base edge in solid white. Mean shear layer axis in dashed white.



## 5.4 Conclusions

The turbulent near-wake flow behind an ogive-cylinder was spatio-temporally characterized based on time-resolved stereoscopic PIV measurements conducted at different azimuthal-radial planes downstream of the base. Analysis of the time-averaged velocity field indicated reverse flow velocities up to  $0.3 U_\infty$  at approximately 60% of the rear-stagnation point location (i.e.  $x/D = 1.2$ ) and turbulent fluctuations with peaks of approximately  $0.18 - 0.19 U_\infty$  in the reattachment region.

The instantaneous velocity fields in proximity of the base revealed a pronounced radial offset of the reversed-flow region from the wake axis. The centroid of the backflow region was found to undergo a precession motion about the model symmetry axis characterized by time-scales in the order of  $10^3 D/U_\infty$ . This precession appeared to vanish when moving downstream towards the rear-stagnation point. Based on the time-history of the backflow centroid position, the characteristic time-scales of this motion were found to be in the order of  $10^3 D/U_\infty$  or higher.

Proper orthogonal decomposition of the velocity fluctuations allowed for identifying a dominant mode pair  $k = 1, 2$  active at all stations and with particularly high contribution at  $x/D = 0.375$ . The associated spatial eigenmodes returned an anti-symmetric radial displacement of azimuthal wave-number  $m = 1$  along a varying azimuthal direction. While close to the base this radial displacement could be entirely ascribed to the backflow azimuthal meandering, in proximity of the rear-stagnation point it appeared to reflect a global wake displacement caused by the wake interaction with the outer flow in the form of an inrush of high momentum flow from outside the separated region. The frequency spectra of the POD time-coefficients displayed peaks in the very-low-frequency range  $St_D = 0.0003 - 0.0005$ , which reduced along the streamwise direction. A higher order mode reflecting an axisymmetric pulsation of the reversed-flow region could be identified at  $x/D = 0.375$  and was linked with a mode of azimuthal wave-number  $m = 0$  (bubble pumping). Smaller-scale shear layer fluctuations could be identified at  $x/D \geq 0.75$  with a mode of azimuthal wave-number  $m = 2$  and were linked with a wake ovalization.

The present data show that the axisymmetric near-wake dynamics is dominated by the very-low-frequency backflow fluctuations in proximity of the base, whereas instead, closer to the rear-stagnation point it is dominated by the fluctuations associated with the shear layer development.

## CHAPTER 6

### THE INFLUENCE OF FLOW SYMMETRY ON THE LONG-TERM BACKFLOW UNSTEADINESS

**Abstract** This chapter examines the effects of angular misalignments on the very-low-frequency backflow meandering of the turbulent wake. Stereoscopic PIV measurements are conducted in the near-wake of an ogive-cylinder in pitch for a Reynolds number  $Re_D = 67,000$ , based on the model diameter. The behavior of the backflow region is examined in the azimuthal-radial plane of the wake for pitch angles between  $0^\circ$  and  $1^\circ$ . The long-time averaged data show a progressive displacement of the inner backflow region from the model symmetry axis with increasing pitch angles and a contextual reduction of its fluctuations about the mean position. This increasing backflow displacement is accompanied by a transformation of the in-plane flow pattern reflecting the emergence of a preferred wake orientation. The time-history of the backflow centroid coordinates gives evidence of a progressive confinement of the backflow fluctuations about the mean off-center position. Modeling the backflow centroid motion based on a stochastically forced Landau equation endorses the hypothesis that misalignments above  $0.1^\circ$  inhibit the erratic behavior of the backflow region and introduce a preferred azimuthal orientation in the wake topology. Snapshot POD analysis of the velocity fluctuations over the angular range considered shows a dramatic reduction in the coherence of the anti-symmetric mode pair  $k = 1-2$ , typically linked with backflow meandering. For pitch angles above  $0.1^\circ$  no evidence is given of the contribution of these modes at the very-low-frequency of  $St_D \sim 10^{-3}$ .

The current results show that the turbulent near-wake features a very-low-frequency backflow unsteadiness only within small deviations from axisymmetric inflow conditions.\*

---

\*This work has been published in Gentile *et al* (2017) Journal of Fluid Mechanics **813**:R3.

## 6.1 Introduction

### 6.1.1 Very-low-frequency wake behavior

For a variety of axisymmetric geometries such as spheres (Fabre *et al* 2008; Thompson *et al* 2001), circular disks (Fabre *et al* 2008; Meliga *et al* 2009; Auguste *et al* 2010) and slender blunt-based bodies (Bohorquez *et al* 2011; Bury and Jardin 2012), the global wake instabilities developing for  $Re_D > 10^2$  follow comparable bifurcation scenarios. This involves successive transitions of the wake topology from a steady axisymmetric state with a toroidal vortex structure, through a steady asymmetric state featuring streamwise oriented (so-called threaded) vortices, to an unsteady periodic asymmetric state where hairpin vortices are alternatively shed off the body at a non-dimensional frequency  $St_D \sim 10^{-1}$ . In both the latter states the wake topology is reflectionally symmetric with respect to a longitudinal plane, also referred to as *shedding plane*, whose orientation is shown to be highly sensitive to both boundary and initial conditions. In the fully turbulent regime, the shedding plane is found to slowly reorient in an erratic fashion along with the inner reversed-flow region, so that over a sufficiently long period of time all orientations are explored with equal probability and the axisymmetry is restored in a long-term statistical sense (cf. subsection 2.2.5). This wake behavior has been documented in several experimental investigations (Riga *et al* 2014; Grandemange *et al* 2014; Gentile *et al* 2016a) and is identified with an anti-symmetric mode of azimuthal wavenumber  $m = 1$  with a very low characteristic frequency of  $St_D \sim 10^{-3}$ . Interestingly, a similar erratic behavior has been observed occurring in the reversed-flow region of annular jets at comparable long time-scales, viz. characteristic frequencies in the order of  $St_D \sim 0.0025$  (Vanierschot and Van den Bulck 2011).

As the statistical wake axisymmetry results from the long-time average of an infinite number of equally probable wake orientations, its existence is strongly connected to the axial symmetry of the inflow conditions, which seldom apply to practical situations. For these reasons, the above very-low-frequency symmetry-restoring mode has been linked with the high sensitivity of the turbulent wake mean topology towards the presence of geometrical imperfections or angular offset with respect to the incoming flow. In particular, Grandemange *et al* (2014) showed that the circumferential probability of the orientation of the sphere wake could be modulated by introducing small disturbances. Previous results of Del Taglia *et al* (2004) indicate that the existence of a symmetry breaking mode is linked to asymmetries of the recirculation region also for the case of thin annular jet flows.

The parametric studies performed by Klei (2012) and Wolf *et al* (2013) on a slender blunt-based body documented a pronounced sensitivity of the time-averaged wake flow towards the presence of sideslip angles, whereby angles as small as  $0.3^\circ$  were shown to displace the stagnation point on the base by as much as  $0.3 D$ .

However, these studies made no connection to the wake dynamics. The experimental investigations conducted by Grandemange *et al* (2012a) on a similar blunt-based model documented a low-frequency switching of the reversed-flow region between two asymmetric topologies and further showed that small angles (not quantified) could suppress such a switch, thus inducing an asymmetric mean topology. In the case of annular jet flows similar asymmetries have been attributed to a high sensitivity of the symmetry breaking mode towards external perturbations.

The present work investigates the relation between the very-low-frequency unsteadiness of the axisymmetric turbulent wake and its sensitivity towards angular misalignments. For this purpose the wake dynamics of an elongated blunt-based axisymmetric body is characterized under conditions of controlled pitch angle. It is hypothesized that the erratic azimuthal meandering of the backflow region observed in nominal, i.e. axisymmetric, inflow conditions tends to be progressively inhibited by increasing misalignments. The investigation is based on time-resolved stereoscopic PIV measurements performed in the near-wake of the model. The angular range where the low-frequency behavior persists is assessed based on the time-history of the backflow centroid coordinates (cf. chapter 5). The current experimental results are further interpreted with the aid of the dynamical model proposed by Rigas *et al* (2015). Lastly, snapshot POD is conducted on the velocity fluctuations such to assess the effects of the pitch angle on the very-low-frequency wake unsteadiness.

### 6.1.2 Dynamical model of the backflow centroid motion

The approach to characterize the very-low frequency backflow instability is motivated by the work of Rigas *et al* (2015). More specifically, the motion of the reverse flow region in the azimuthal plane ( $y, z$ ), Fig. 6.1, is modeled as a Brownian process and described by means of a stochastically forced non-linear differential equation. This model, which is built upon observations conducted under axisymmetric inflow conditions, is here extended to the case of off-nominal inflow conditions (i.e. non-zero pitch angle). For this purpose an instantaneous displacement of the backflow centroid relative to its mean position  $\mathbf{s} = \mathbf{r}_c - \langle \mathbf{r}_c \rangle$  is defined, such to accommodate the mean offset caused by the introduced pitch. Assuming a rotational symmetry with respect to  $\mathbf{s} = 0$ , the backflow centroid dynamics is modeled by a stochastically perturbed Landau equation

$$\dot{\mathbf{s}} = \lambda_1 \mathbf{s} - \lambda_2 \|\mathbf{s}\|^2 + \sigma \boldsymbol{\xi}(t) \quad (6.1)$$

The first two terms in (6.1) represent the deterministic part of the model, wherein  $\lambda_1$  accounts for the linear growth rate of the disturbance and  $\lambda_2 > 0$  is the coefficient of the non-linear term responsible for the saturation of the displacement. The stochastic part of the model is contained in the third term, which is the random turbulent forcing  $\boldsymbol{\xi}(t)$  with variance  $\sigma^2$ . Introducing the relative displacement

$s = \|s\|$ , the equilibrium position  $s = 0$  is stable when  $\lambda_1 < 0$ , while it becomes unstable under a pitchfork bifurcation for  $\lambda_1 > 0$  upon which a new stable equilibrium is established at  $s = \sqrt{\lambda_1/\lambda_2}$ . With the stochastic forcing taken into account, the probability density function for  $s$  is given by (cf. Rigas *et al* 2015)

$$P(s) = \frac{1}{N} \frac{dN}{2\pi s ds} = C \exp\left(a_1 s^2 - \frac{a_2 s^4}{2}\right) \quad (6.2)$$

wherein  $N$  is the total number of observations of the centroid position,  $C$  is a normalization factor,  $a_1 = \lambda_1/\sigma^2$  and  $a_2 = \lambda_2/\sigma^2$ .

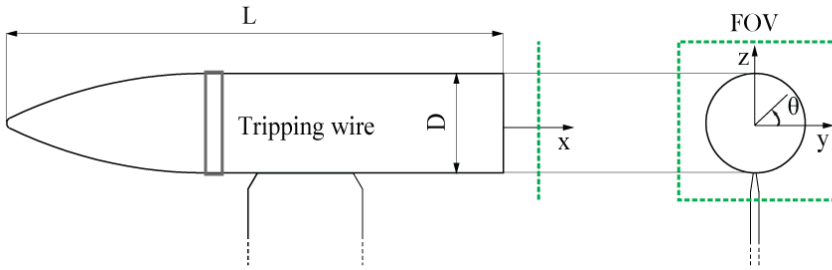


**Figure 6.1 Side and back view of the wind-tunnel model with coordinate system and field of view (FOV).**

The probability distribution in (6.2) as predicted by the stochastic model is compared in the present study with the experimental observations in order to examine the applicability of the model under asymmetric inflow conditions and to assist the interpretation of the changes in the backflow erratic behavior due to the variation in angle.

## 6.2 Experimental setup

The experiments were conducted at a diameter-based Reynolds number  $Re_D = 67,000$  on a model geometry comprising a cylindrical forebody with ogival nose with total aspect ratio  $L/D = 5$  (Fig. 6.1). A roughness patch located at the nose-body junction ensured turbulent flow conditions at the trailing edge. The boundary layer thickness 5mm upstream of this point was measured to be  $\delta_{95} = 4.8$  mm with a momentum thickness-based Reynolds number  $Re_\theta \approx 900$  (cf. chapter 4). A detailed description of the flow facility and wind tunnel model can be found in section 3.1.

Stereoscopic PIV measurements were conducted in a plane located at  $x/D = 0.3$  and oriented perpendicular to the freestream flow. The pitch angle between the model symmetry axis and the freestream flow was varied during the experiments between  $0^\circ$  and  $1^\circ$  using a dedicated support plate (cf. Fig. 3.6 and 3.7). The

recordings were performed over a total observation-time of 100 s, corresponding to 40,000  $D/U_\infty$  in convective time units. An overview of the main PIV measurement parameters is provided in Table 6.I.

**Table 6.I** Main stereoscopic PIV measurement settings

Freestream velocity $U_\infty$	20 m/s
Diameter-based Reynolds number $Re_D$	67,000
Streamwise measurement plane $x/D$	0.3
Pitch angle $\alpha$ range	$0^\circ - 1^\circ$
Laser sheet thickness $t$	1.5 mm
Laser pulse separation $\Delta t$	20 $\mu$ s
Cameras viewing angle $\beta$	$70^\circ$
Objective f- number $f_\#$	5.6
FOV size	75 x 75 mm <sup>2</sup>
Image magnification $M$	0.2
Vector pitch	0.6 mm
Acquisition frequency $f_{acq}$	50 Hz
Data ensemble size $N$	5000
Measurement duration $T$	100 s

## 6.3 Results

### 6.3.1 Mean and instantaneous backflow behavior

The effects of increasing misalignments are herein examined based on time-averaged and instantaneous velocity data.

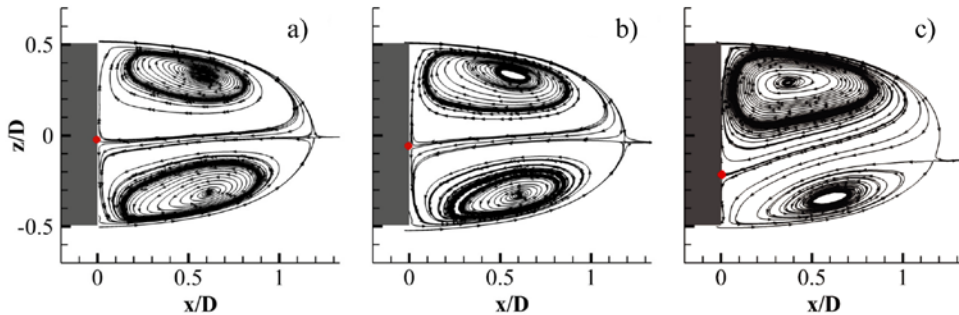


**Figure 6.2** Time-averaged streamlines in the plane  $y = 0$ . Pitch angle  $\alpha = 0^\circ$  (a),  $0.1^\circ$  (b) and  $0.3^\circ$  (c). Stagnation point on the base in red. Model edge in gray.

Additional measurements conducted in the longitudinal plane  $y = 0$  (Fig. 6.2) show that the pitch angle modifies the mean inner organization of the near-wake by inducing a vertical shift of the stagnation point on the base. In the azimuthal-radial plane this shift is reflected in a displacement of the reversed-flow region away from the geometric center of the wake and by a progressive change of the in-plane flow pattern (Fig. 6.3).

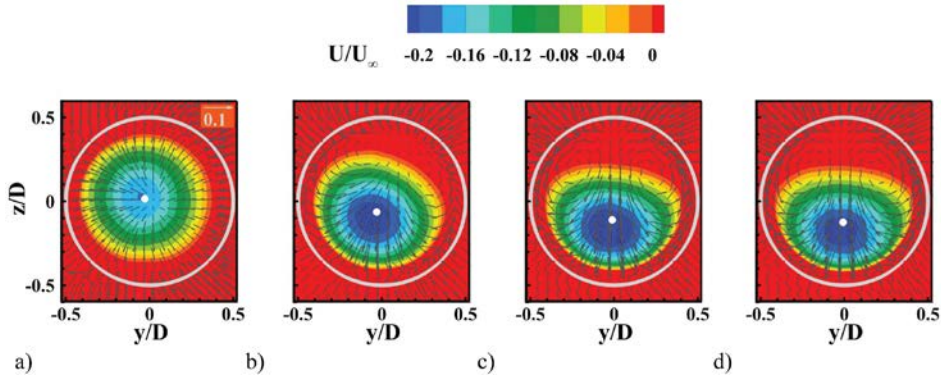


**Figure 6.3** Time-averaged velocity field in the plane  $(y, z)$ . Pitch angle  $\alpha = 0^\circ$  (a),  $0.1^\circ$  (b),  $0.3^\circ$  (c),  $0.5^\circ$  (d). Color coded out-of-plane component. Vectors plotted every 5th grid point represent in-plane velocity components. Mean backflow centroid in white. Base edge in gray.

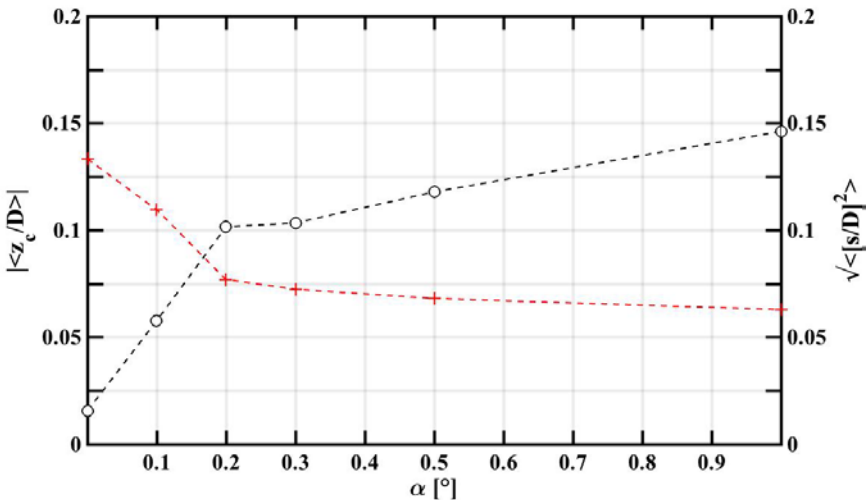


**Figure 6.4** Mean vertical position and root mean square (RMS) of the relative displacement of the backflow centroid as a function of the pitch angle.

The in-plane vectors indicate a transformation of the wake topology from a

source-like pattern observed for axisymmetric inflow conditions to two in-plane counter-rotating recirculation patterns. The latter topology may be linked to the emergence of a preferred wake orientation (Grandemange *et al* 2014).

The mean backflow centroid shows a significant sensitivity towards the angular offset for angles up to  $0.2^\circ$ , being displaced from the model axis at a rate of approximately  $0.5 D$  per degree (see Fig. 6.4), while a marked lower rate of increase is observed at larger pitch angles. Furthermore, the decreasing variance of the relative backflow displacement  $\sqrt{\langle [s/D]^2 \rangle}$  suggests a weakening of the erratic backflow behavior on increasing the angle.

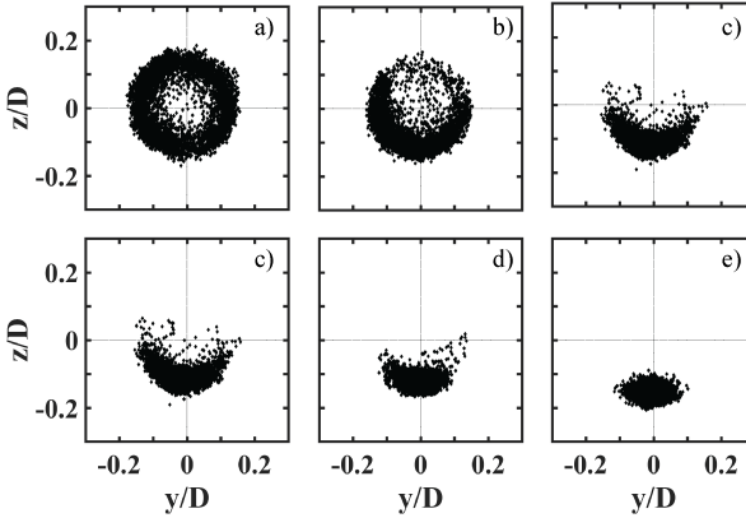


**Figure 6.5 Scatter plots of the backflow centroid in-plane position. Pitch angle  $\alpha = 0^\circ$  (a),  $0.1^\circ$  (b),  $0.2^\circ$  (c),  $0.3^\circ$  (d),  $0.5^\circ$  (e) and  $1^\circ$  (f).**

The time-history of the backflow centroid position is examined in order to retrieve information on the dynamical behavior of the reversed-flow region. With increasing pitch angles the trace of the backflow centroid motion (Fig. 6.5) evolves from the *donut*-like distribution, typically associated with the azimuthal meandering behavior, to a comparatively narrower and elongated cloud. This trend reflects the progressive confinement of the backflow motion close to the average off-center position.

The probability density distributions reported in Fig. 6.6 further reflect this transition. In particular, for angles within  $0.1^\circ$  the maximum probability of the relative displacement (Fig. 6.6a) occurs for values of  $s$  between  $0.13 D$  and  $0.07 D$ , thus reflecting the instability of the centroid position. For angles of  $0.2^\circ$  and higher instead, the probability decreases monotonically from the origin, as the position of the backflow centroid tends to settle close to the mean off-center position. Similarly,



the distributions obtained for the azimuthal coordinate (Fig. 6.6b) gradually narrow about  $3\pi/2$ , which value emerges as the preferred orientation of the instantaneous wake topology.

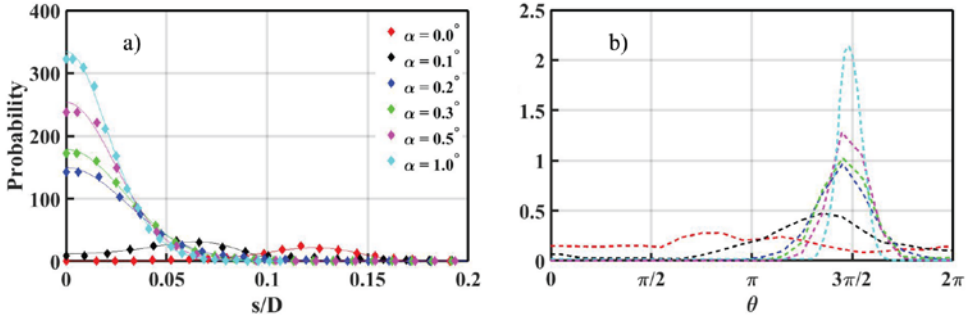


**Figure 6.6** Probability distributions of the backflow relative displacement (a) and azimuthal position (b). Solid lines in (a) indicate the curve fits based on (6.2).

The solid lines in Fig. 6.6a show the curve fit of the stochastic model presented in (6.2) to the experimental data. A good agreement is found which indicates that the model can also be used to describe the situation under asymmetric inflow conditions. The coefficient  $a_1$  associated with the stability of the equilibrium position is found to decrease with increasing angles (Fig. 6.7). The sign reversal occurring between  $0.1^\circ$  and  $0.2^\circ$  is a clear indication that the backflow settles in a stable condition, which corresponds to the azimuthal orientation imposed with the applied angle.

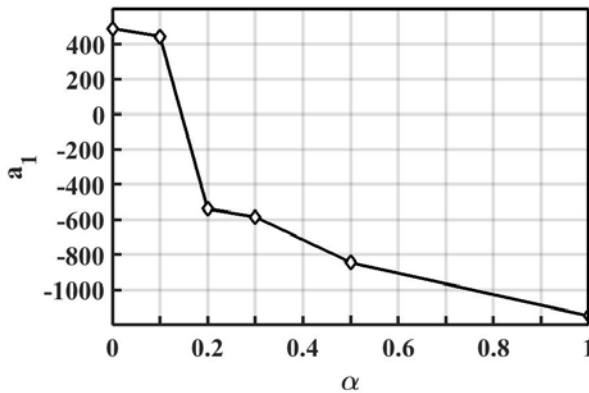


**Figure 6.7** Model coefficient  $a_1$  determined from the curve fit to the experimental probability distribution of  $s$ .

The foregoing analysis based on the application of the dynamical model of subsection 6.1.1, describes the suppression of the large-scale meandering as an inverse pitchfork bifurcation. Closer inspection of the scatter plots in Fig. 6.5 reveals

that the pitch angle introduces an asymmetry with respect to the  $z$ -direction. This fact indicates an imperfect character of the bifurcation (Strogatz 2000), which cannot be represented by the original rotationally-symmetric model. Accommodating this feature in a generalization of the two-dimensional Landau model by removing the assumption of rotational symmetry is, however, quite elaborate and outside the scope of the present discussion.

Instead of using a full 2D model, it is herein considered that the asymmetrical character of the bifurcation could be conveniently represented by studying its behavior in the proximity of the  $z$ -axis, thus assuming that  $y$  is small. With this approach an asymmetric Landau system for the vertical position of the reversed flow centroid is obtained with only two additional terms with respect to the original symmetrical system as follows

$$\frac{dz}{dt} = \lambda_0 + \lambda_1 z + \lambda_2 z^2 - \lambda_3 z^3 + \sigma \xi(t) \quad (6.3)$$

The corresponding probability density function, following a similar derivation as for (6.2), is given by

$$P(z) = \frac{1}{N} \frac{dN}{dz} = C \exp(c_0 z + c_1 z^2 + c_2 z^3 - c_3 z^4) \quad (6.4)$$

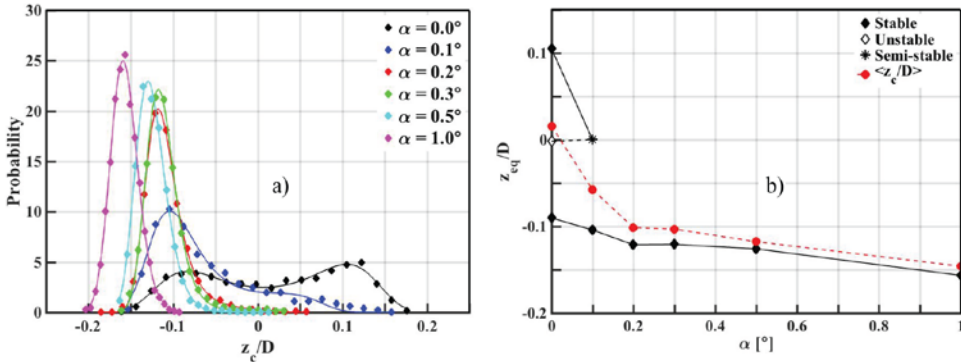


**Figure 6.8** Probability distributions of the backflow in-plane vertical position (a). Bifurcation diagram depicting stable and unstable equilibrium positions and mean vertical centroid positions of the full 2D data set as a function of the pitch angle (b). Solid lines in (a) represent the curve fits based on (6.4).

Extracting the probability density distribution from the observed data provides information on the stable and unstable equilibrium points of the system (corresponding to the minima and maxima of the probability density function respectively), which can subsequently be depicted in a bifurcation diagram ( $z_{eq}$  versus  $\alpha$ ), see Fig. 6.8b. The probability distribution is approximately symmetrical for  $\alpha = 0^\circ$  with an unstable equilibrium occurring at  $z = 0$ , and two stable equilibria

symmetrically located at  $z = \pm 0.1 D$ .

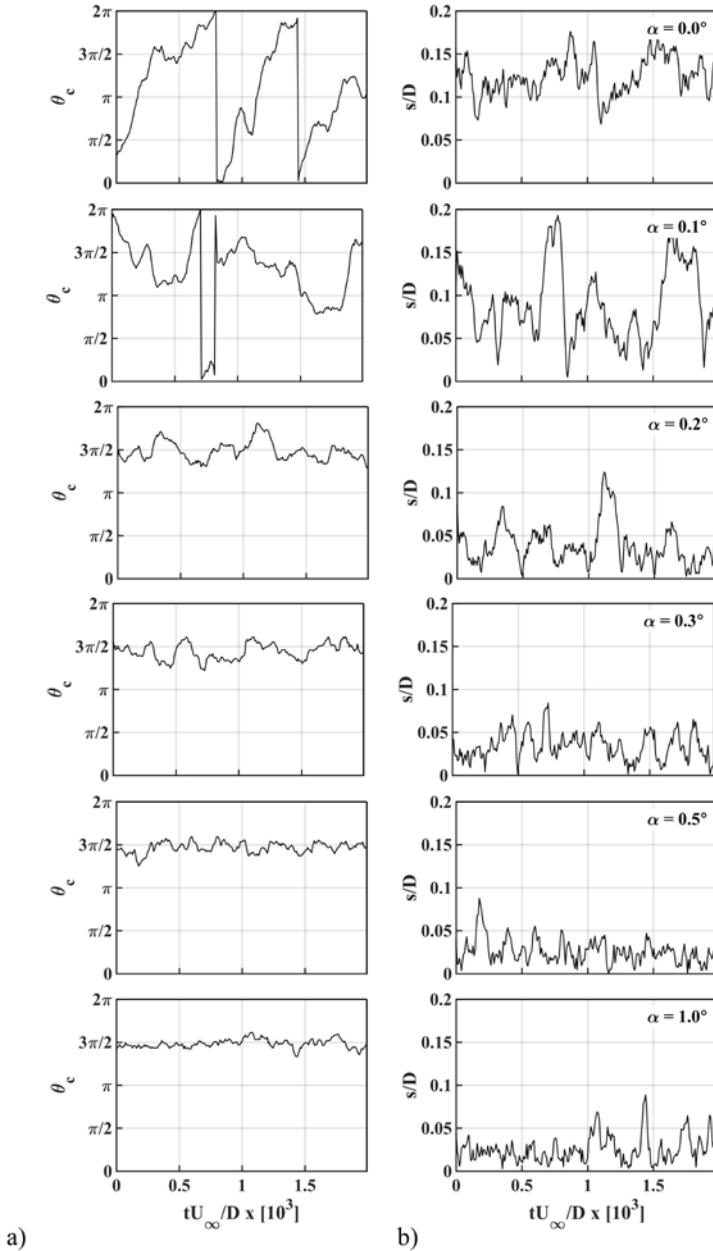


**Figure 6.9** Time-history of the backflow centroid position for increasing pitch angle. Azimuthal position (a). Relative displacement (b). Total observation time is  $2,000 D/U_\infty$ .

For  $\alpha = 0.1^\circ$  a maximum can still be observed in the probability density function for negative  $z$ , whereas the maximum on the positive  $z$  side and the minimum have collapsed leaving an inflexion point, which could be interpreted as a semi-stable equilibrium, at approximately  $z = 0$ . For larger pitch angles a clear single maximum occurs corresponding to a stable equilibrium, which is progressively displaced to larger  $z$ -values as the pitch angle increases.

Thus, the analysis is consistent with an imperfect bifurcation setting in at  $\alpha = 0.1^\circ$ , and as such, is in agreement with the conclusions from the rotationally-symmetric model. The average centroid position of the full 2D data set, comparable to the data in Fig. 6.4, has been included for comparison (dashed line). The latter shows that for small angles, viz.  $\alpha < 0.1^\circ$ , the mean position corresponds closely to the central unstable equilibrium, while for increasing pitch angles it gradually converges towards the equilibrium position of the 1D model.

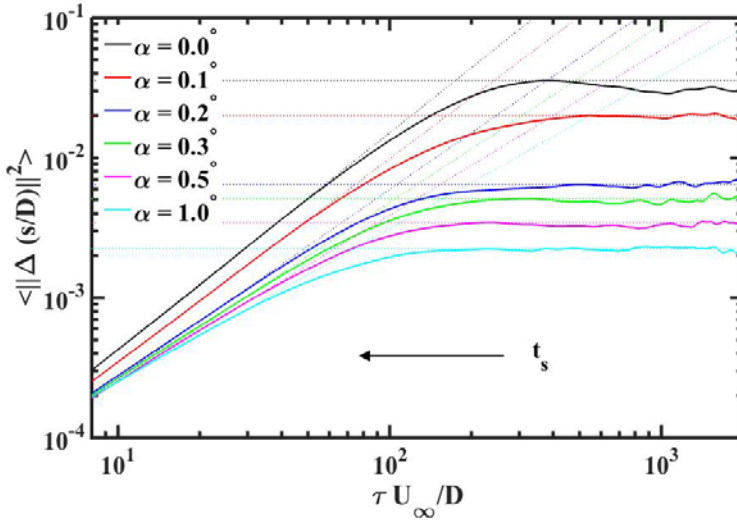


**Figure 6.10 Mean-square displacement of the backflow centroid as a function of the time-interval  $\tau$ .**

The time history of the azimuthal coordinate and relative displacement presented in Fig. 6.9 further endorses this conclusion and shows the progressive weakening of the large-scale meandering fluctuations for increasing angle and the concurrent confinement of the centroid motion near the off-center mean position.

Especially the fluctuations of the azimuthal position give evidence of a transition from a quasi-periodic meandering characterized by time-scales in the order of  $10^3 D/U_\infty$  and identifiable with an erratic precession about the model axis (Rigas *et al* 2014; Grandemange *et al* 2014), to lower-amplitude higher-frequency fluctuations about a preferred orientation corresponding to  $\theta = 3\pi/2$ . Further insight in the time-scales involved in the backflow dynamics can be extracted from the mean-square

centroid displacement, defined as  $\langle ||\Delta s(\tau)||^2 \rangle = \langle ||s(t+\tau) - s(t)||^2 \rangle$  (cf. Rigas *et al* 2015).

The mean-square displacement (MSD) (Fig. 6.10) features a linear increase with the time interval  $\tau$ , which reflects the diffusive dynamics of the backflow centroid position, while it saturates attaining a plateau, at larger time-scales, where the centroid position becomes uncorrelated with time. As the angle is increased, the MSD increase tends to be less steep and features an earlier saturation, thus reflecting the confinement of the backflow motion. This trend is seen to be associated with a reduction in the characteristic time-scales  $t_s$ .

### 6.3.2 Proper Orthogonal Decomposition

Snapshot POD (Sirovich 1987) is applied to the velocity fluctuations to further examine the effects of the misalignment on the large-scale dynamics dominating the near-wake. The reader is referred to section 3.4 for details on the mathematical procedure.

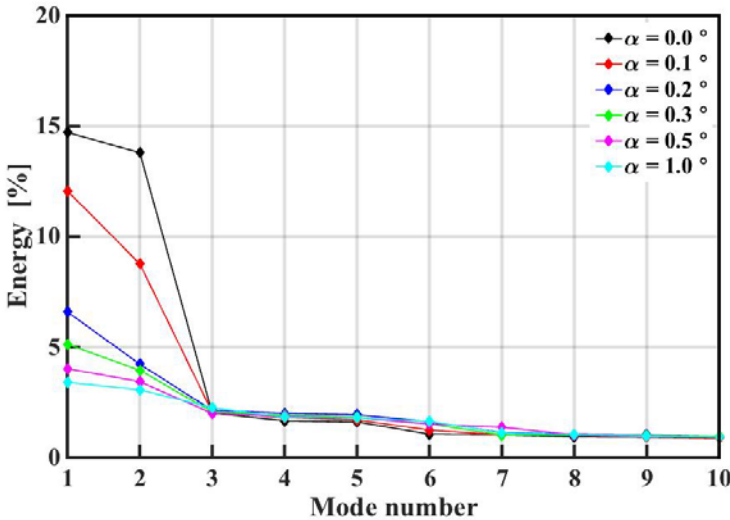
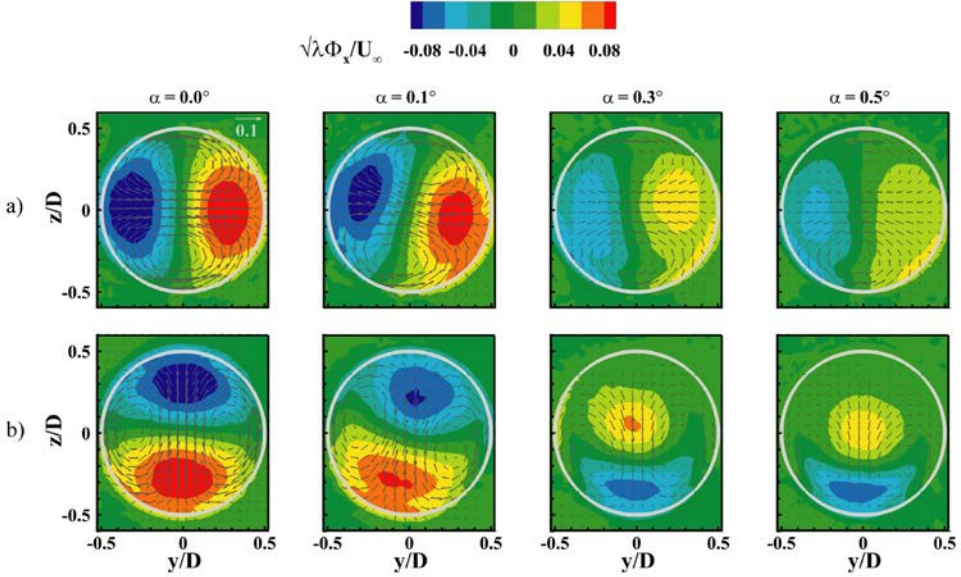


Figure 6.11 Energy contribution of the first 10 POD modes.

The relative energy contributions of the first 10 POD modes and the spatial distributions of modes  $k = 1$  and  $k = 2$  are shown in Fig. 6.11 and Fig. 6.12 respectively. As discussed in chapter 5, in axisymmetric conditions ( $\alpha = 0^\circ$ ) the two modes exhibit similar anti-symmetric dipolar arrangements and comparable energy contributions (approximately 15% and 14% respectively), suggesting that they can be identified as a pair corresponding to an azimuthal mode  $m = 1$ . The latter can be linked with the backflow meandering, for which the centroid covers the whole azimuth (cf. chapter 5).

A similar scenario is observed under small pitch angles ( $\alpha \leq 0.1^\circ$ ), albeit with

increasing differences in terms of energy and spatial distribution. The contribution of modes  $k = 1$  and  $k = 2$  starts decreasing substantially for angles of  $0.3^\circ$  and higher. This progressive loss in coherence features an increasing eccentricity in the spatial distribution and reflects the emergence of a preferred wake orientation, as previously inferred from the history of the backflow centroid position.



**Figure 6.12** POD modes  $k = 1$  (a) and  $k = 2$  (b) for different pitch angles. Color coded out-of-plane component. In-plane vectors plotted every 5th grid point represent in-plane components  $\sqrt{\lambda_k} \Phi_{k,y} / U_\infty$  and  $\sqrt{\lambda_k} \Phi_{k,z} / U_\infty$ . Base edge in gray.

A similar scenario is observed under small pitch angles ( $\alpha \leq 0.1^\circ$ ), albeit with increasing differences in terms of energy and spatial distribution. The contribution of modes  $k = 1$  and  $k = 2$  starts decreasing substantially for angles of  $0.3^\circ$  and higher. This progressive loss in coherence features an increasing eccentricity in the spatial distribution and reflects the emergence of a preferred wake orientation, as previously inferred from the history of the backflow centroid position.

The transition from long-term azimuthal meandering to small-amplitude oscillations about a mean position is further visualized in the frequency spectra of the time coefficients of the first two POD modes (Fig. 6.13). Within  $0.1^\circ$  deviations from axisymmetric conditions a significant contribution is observed at very-low frequencies around  $St_D \sim 10^{-3}$ , to a similar extent for both POD modes. At larger angles the spectra are dominated by broader band fluctuations of significantly smaller intensity in the frequency range corresponding to  $St_D = 0.005 - 0.01$ , and are only associated with mode  $k = 1$ .

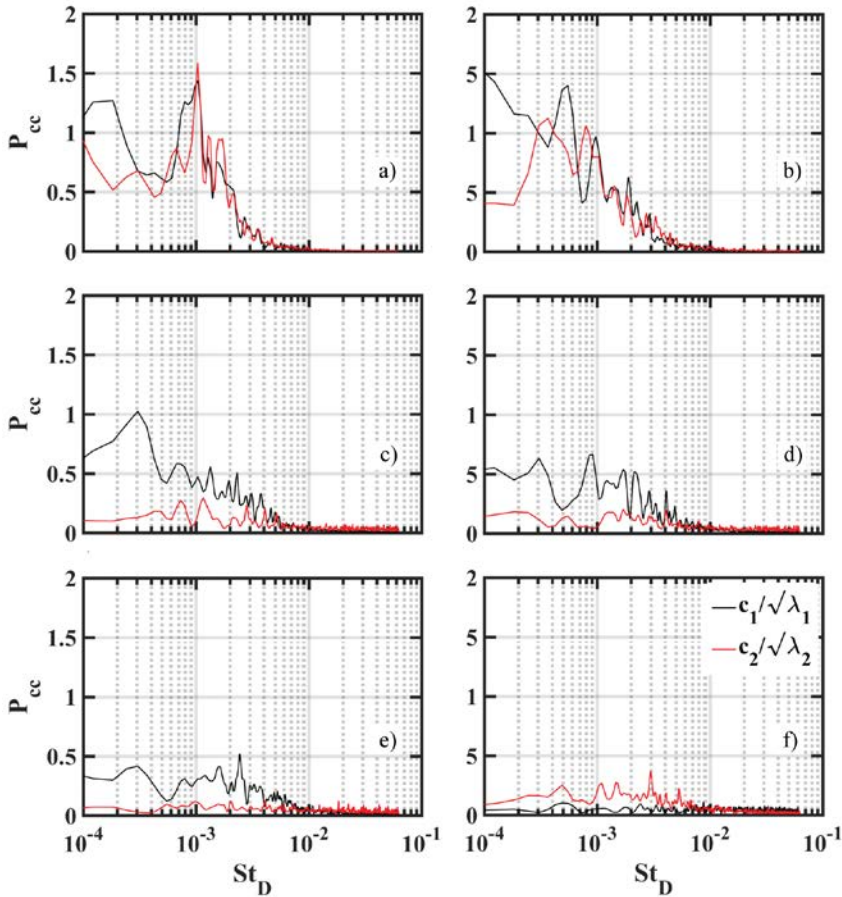


Figure 6.13 Frequency spectra of POD time-coefficients  $c_1(t)$  and  $c_2(t)$ . Pitch angle  $\alpha = 0^\circ$  (a),  $0.1^\circ$  (b),  $0.2^\circ$  (c),  $0.3^\circ$  (d),  $0.5^\circ$  (e) and  $1^\circ$  (f).

## 6.4 Conclusions

The very-low-frequency unsteadiness of the near-wake of a blunt-based axisymmetric body in pitch was characterized based on time-resolved stereoscopic PIV measurements. The angular misalignment was found to displace the inner reversed-flow region away from the model symmetry axis and to impose a preferred azimuthal orientation of the near-wake topology. The time history of the centroid position outlined the transition from an erratic azimuthal meandering of the backflow region to smaller-amplitude fluctuations about the mean off-center position.

Modeling the backflow centroid motion based on a stochastically perturbed Landau equation showed that pitch angles above  $0.1^\circ$  inhibit the erratic character

of the backflow region, which tends to settle in the off-center position imposed by the applied pitch angle. The analysis of the mean-square backflow displacement indicated an earlier saturation of the backflow fluctuations and a progressive inhibition of the diffusive dynamics of the reversed-flow region for increasing angles. The frequency spectra of the time-coefficients of the first two POD modes showed the vanishing of the very-low-frequency contribution typically identified with the backflow azimuthal meandering for angles for  $0.2^\circ$  or higher.

These results provide clear evidence that the reversed-flow region in the turbulent wake exhibits an erratic behavior only within small deviations from axisymmetric inflow conditions.





## CHAPTER 7

### AZIMUTHAL ORGANIZATION AND UNSTEADINESS OF AN AFTERBODY FLOW

**Abstract** This chapter investigates the azimuthal-radial topology and large-scale unsteadiness of a turbulent incompressible afterbody flow for a diameter-based Reynolds number  $Re_D = 67,000$ . The behavior of the near-wake is examined at different streamwise stations downstream of the trailing edge for diameter ratios of  $d/D = 0.2$  and  $0.4$ . The long time-averaged velocity field shows that the central protrusion does not alter the mean near-wake topology significantly. However, the statistical fluctuations in the radial direction reduce by nearly 80% when increasing the afterbody diameter ratio up to  $0.4$  starting from the blunt-based case. The time-history of the backflow centroid position gives no evidence of an azimuthal meandering motion for diameter ratios of  $d/D = 0.2$  and  $0.4$ . The large-scale fluctuations identified by snapshot POD are found to progressively reduce with increasing protrusion diameters, reflecting a decreasing large-scale organization of the near-wake flow. Inspection of the spatial eigenmodes highlights the occurrence of a large-scale radial displacement of the wake for diameter ratios of  $d/D = 0$  and  $0.2$  occurring equally along all azimuths. For larger afterbody cross-sections the large-scale fluctuations are found to occur along a preferred azimuth.

The present results show that the coherence of the backflow azimuthal fluctuations is disrupted in presence of an afterbody with  $d/D = 0.2$  and  $0.4$ . Thus, for these configurations the wake dynamics is dominated by the fluctuations associated with the shear layer development\*

---

\*This work has been presented at the 5th International Conference on Jet, Wakes and Separated Flows in Stockholm, Sweden, in June 2015.

## **7.1 Introduction**

The low-frequency unsteadiness in the near-wake of a bluff body of revolution is significantly affected by the base geometry (cf. chapter 2). Among others, the experiments conducted by Wolf *et al* (2012) showed that for a truncated-base rocket configuration the turbulence intensity reduces by approximately 25% when adding a rear cylindrical protrusion (i.e. afterbody). The studies of Dépres *et al* (2004) revealed that the elongation of the afterbody with respect to the base diameter, viz.  $L/D$ , plays a major role in the flow reattachment process, thereby affecting both the flow topology and the unsteady behavior of the wake. The influence of the afterbody diameter on the scaling of the reattachment distance and on the flow organization, as well as on the radial velocity fluctuations has been recently discussed in Gentile *et al* (2016b), (cf. chapter 4). Through spectral analysis of the POD time-coefficients in a longitudinal plane containing the mean wake axis, the authors found evidence of the very-low-frequency contribution associated with backflow meandering with decreasing intensity for increasing afterbody to main body diameter ratios  $d/D \leq 0.4$ . Yet, the orientation of the measurement plane did not provide any information on the azimuthal organization of the flow.

The current investigation builds up the discussion carried out in chapter 4 and aims at characterizing the spatial organization of the turbulent axisymmetric near-wake of an afterbody configuration. For this purpose stereoscopic PIV measurements are conducted in the azimuthal-radial plane of the wake at different streamwise stations downstream of the trailing edge and for varying afterbody diameters. Mean and instantaneous near-wake behaviors are examined for the different cases in comparison with the data gathered for the truncated-base configuration. Furthermore the influence of the afterbody diameter on the near-wake large-scale organization is examined performing a snapshot POD analysis of the velocity fluctuations (Sirovich 1987).

## **7.2 Experimental setup**

The measurements were performed on an ogive-cylinder geometry with total aspect ratio  $L/D = 5$  and equipped with a cylindrical afterbody of smaller diameter  $d$  (Fig. 7.1). In the present experiments two different configurations were examined, corresponding to an afterbody to main body diameter ratio  $d/D = 0.2$  and  $0.4$  respectively. The reader is referred to section 3.2 for details on the flow facility and wind tunnel model.

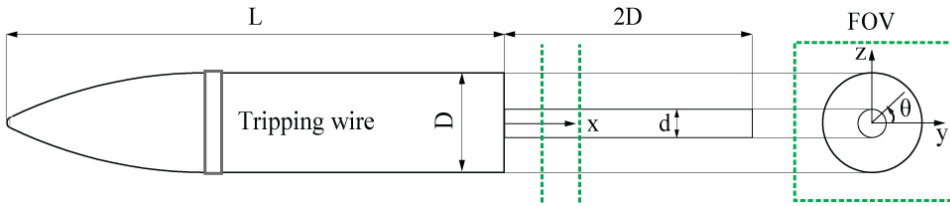


**Figure 7.1** Model schematic side and end view with coordinate system and field of view (FOV).

Stereoscopic PIV measurements were performed in azimuthal-radial planes located at  $x/D = \{0.375; 0.75\}$  downstream of the main body trailing edge, which stations correspond to about 30% and 60% of the reattachment distance respectively, for  $d/D = 0.2$  and to about 40% and 75% of the reattachment distance respectively for  $d/D = 0.4$  (cf. chapter 4). An overview of the main PIV measurement parameters is provided in Table 7.I.

**Table 7.I** Main stereoscopic PIV measurement settings

Freestream velocity $U_\infty$	20 m/s
Diameter-based Reynolds number $Re_D$	67,000
Afterbody to main body diameter ratio $d/D$	0.2, 0.4
Streamwise measurement planes $x/D$	0.375, 0.75
Laser sheet thickness $t$	3 mm
Laser pulse separation $\Delta t$	25 $\mu$ s
Cameras viewing angle $\beta$	35°
Objective f- number $f_\#$	2.8
FOV size	75 x 75 mm <sup>2</sup>
Image magnification $M$	0.16
Vector pitch	1.0 mm
Acquisition frequency $f_{acq}$	100 Hz
Data ensemble size $N$	500
Measurement duration $T$	50 s

## 7.3 Results

### 7.3.1 Flow field statistics

The time-averaged velocity field obtained at the streamwise station  $x/D = 0.75$  for increasing afterbody diameters is shown in Fig. 7.2. The data obtained for the corresponding truncated-base configuration (cf. chapter 5) are included for comparison.

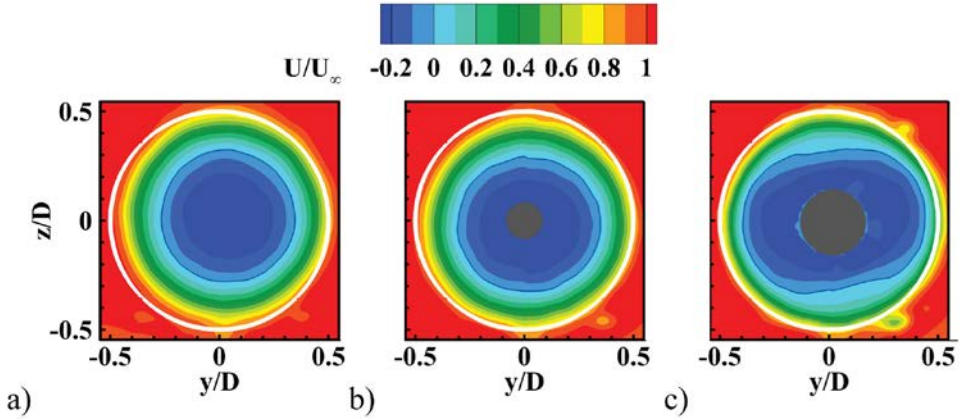


**Figure 7.2** Time-averaged velocity field at  $x = 0.75 D$ . Diameter ratio  $d/D = 0$  (a), 0.2 (b) and 0.4 (c). Color coded out-of-plane velocity. Backflow region indicated by contour line. Model base trace in white. Afterbody in gray.

The contours of the out-of-plane velocity define the toroidal wake organization typical of axisymmetric near-wake flows, characterized by a circular shear layer bounding an inner region of reversed flow with velocities up to  $0.3 U_\infty$ . The comparison between the three cases reveals no significant distortions of the mean topology due to the presence of the afterbody.

The distributions obtained in the longitudinal plane ( $x, z$ ) on the other hand, document a substantial reduction of the normal stresses along the vertical direction with increasing protrusion diameters (Fig. 7.3). This fact reflects a marked sensitivity of the near-wake flow towards variations in the base geometry (cf. chapter 4). In particular, the intensity of the radial fluctuations is found to decrease from a maximum of  $0.18 U_\infty$ , attained in absence of afterbody, to  $0.12 U_\infty$  and  $0.10 U_\infty$ , for  $d/D = 0.2$  and  $d/D = 0.4$  respectively. This observation is consistent with the experimental results by Wolf *et al* (2012), indicating a stabilization of the near-wake unsteadiness due to the presence of the protrusion.

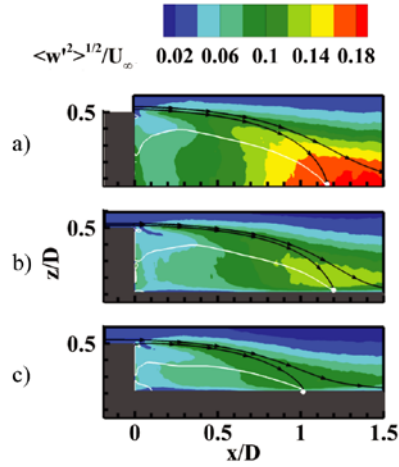


Figure 7.3 Radial fluctuations at  $y = 0$ . Diameter ratio  $d/D = 0$  (a), 0.2 (b) and 0.4 (c). Color coded RMS of the vertical velocity fluctuations. Reattachment streamline in black. Reattachment point in white. Backflow region indicated by a white contour line. Model in gray.

### 7.3.2 Backflow unsteadiness

Following the same approach illustrated in previous investigations (Grandemange *et al* 2012b; Gentile *et al* 2016a), the time-evolution of the backflow centroid position is examined to evaluate the effects of the rear-protrusion and of its diameter onto the backflow dynamics.

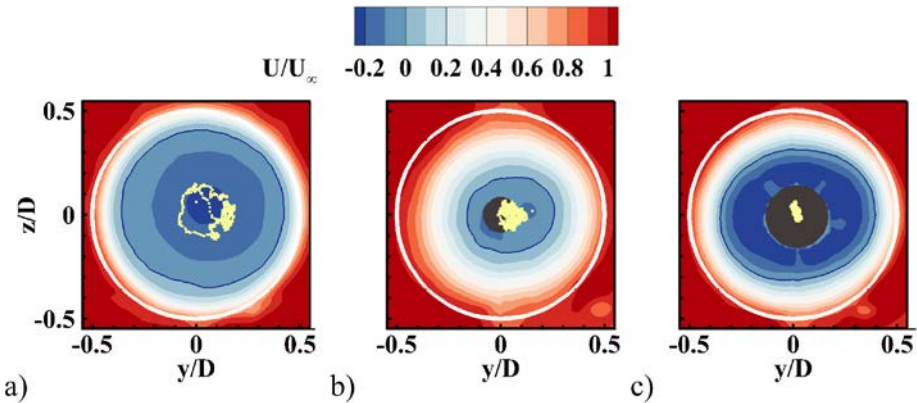


Figure 7.4 Trace of the backflow motion at  $x = 0.375 D$ . Diameter ratio  $d/D = 0$  (a), 0.2 (b) and 0.4 (c). Color coded mean out-of-plane velocity over 20,000  $D/U_\infty$ . Backflow centroid in yellow. Backflow region indicated by contour line. Model base trace in black. Afterbody in gray.

The latter are collected over a portion of the available observation-time and super-imposed

onto the contours of the mean velocity field (Fig. 7.4). The analysis is restricted to the streamwise station  $x/D = 0.375$ , where the backflow azimuthal instability is expected to be dominant (cf. chapter 5). For diameter ratios of  $d/D = 0.2$  the trace of the backflow motion displays no pattern identifiable with a coherent azimuthal meandering motion (Rigas *et al* 2014; Grandemange *et al* 2014). In fact, it appears rather random compared with the reference truncated-base case, reflecting the loss in coherence of the backflow fluctuations due to the addition of the afterbody. For further increases in the diameter ratio, i.e. to  $d/D = 0.4$ , the trace of the backflow motion appears nearly aligned with the  $z$  axis.

### 7.3.3 Proper Orthogonal Decomposition

A snapshot POD analysis of the velocity fluctuations is conducted to assess the effects of the rear-protrusion on the large-scale wake unsteadiness. The POD energy spectra shown in Fig. 7.5 feature a relatively large contribution of the first couple of modes to the turbulent kinetic energy, thus reflecting the occurrence of large-scale fluctuations.

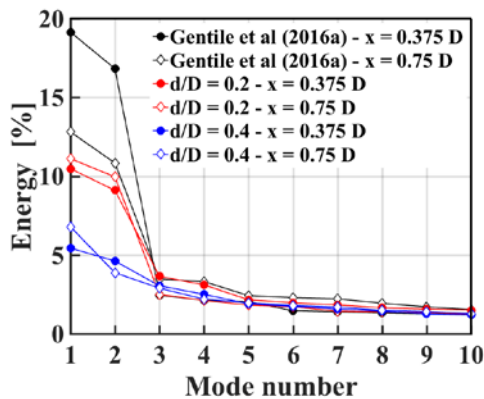


Figure 7.5 POD spectra for the first 10 modes.

Modes  $k = 1$  and  $k = 2$  capture up to 20% and 11% of the turbulent kinetic energy of the flow for  $d/D = 0.2$  and  $d/D = 0.4$  respectively, with minor variations in the streamwise direction. In particular, for  $d/D = 0.2$  the contribution of the first two modes intensifies while moving away from the base in the streamwise direction, whereas the opposite is observed for  $d/D = 0$ .

This different behavior is ascribed to the suppression of the backflow fluctuations for  $d/D = 0$  and  $0.2$ , which prevail in proximity of the base (cf. chapter 5), with consequent dominance of the shear layer fluctuations. This trend would suggest that the protrusion primarily affects the backflow unsteadiness. The first two spatial eigenmodes (Fig. 7.6) feature a typical *dipolar* distribution, which is identified with the anti-symmetric mode  $m = 1$  for  $d/D \leq 0.2$  and linked with an anti-symmetric radial displacement of the wake occurring equally in all azimuthal directions. For  $d/D = 0.4$  this dipolar

organization features mode  $k = 1$  only, indicating the occurrence of large-scale fluctuations along a preferred azimuthal direction. Mode  $k = 2$  instead, features a *quadrupole* structure, which can be linked with a wake *ovalization* (Schrijer *et al* 2014; Gentile *et al* 2016a). This missing dynamical pairing between the two modes appears consistent with the increasing energy gap indicated by the energy spectra for this configuration (cf. Fig. 7.5) and further reflects the decreasing large-scale organization of the wake for increasing afterbody cross-sections.

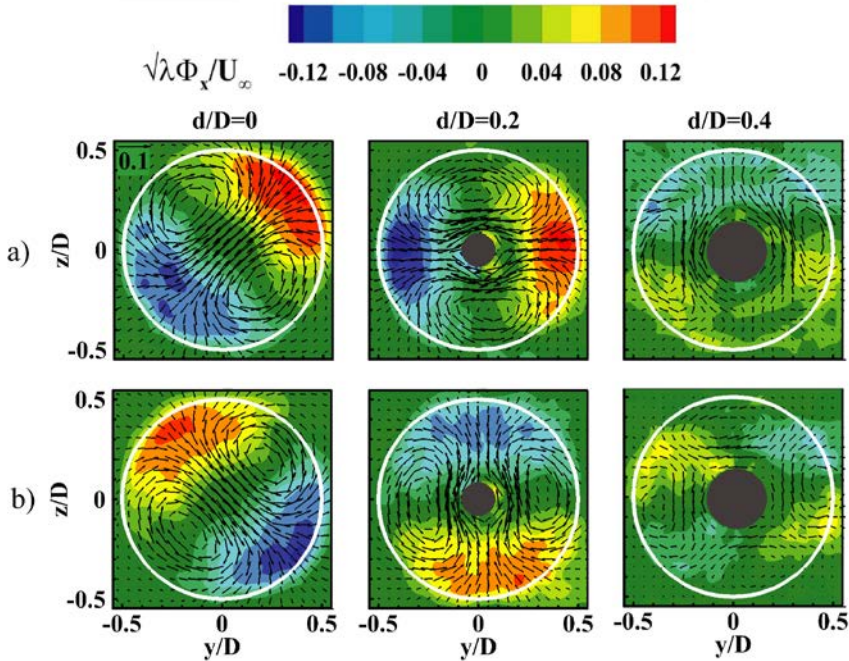


Figure 7.6 POD modes  $k = 1$  (a) and  $k = 2$  (b) at  $x = 0.75 D$  for increasing  $d/D$ . Color coded out-of-plane component. Vector arrows plotted every 4th grid point for  $d/D = 0$  and every 3th grid point for  $d/D = 0.2$  and  $d/D = 0.4$  represent in-plane components  $\sqrt{\lambda_k} \Phi_{k,y} / U_\infty$  and  $\sqrt{\lambda_k} \Phi_{k,z} / U_\infty$ . Model base trace in white. Afterbody in gray.

## 7.4 Conclusions

The azimuthal organization of the turbulent near-wake past an ogive-cylinder with afterbody was investigated at a diameter-based Reynolds number  $Re = 67,000$ . Time-resolved stereoscopic PIV measurements were performed at different cross-flow planes downstream of the trailing edge for varying diameter ratios.

Compared to the truncated-base geometry, the time-averaged velocity field showed no substantial alterations of the azimuthal-radial organization of the wake due to the rear-protrusion, whereas the statistical fluctuations of the radial velocity



reduced by up to 44% when increasing the diameter ratio up to  $d/D = 0.4$ . The time-history of the backflow centroid position shows that the protrusion entirely disrupts the coherence of the azimuthal backflow meandering for diameter ratios of  $d/D = 0.2$  and  $0.4$ . For increasing diameter ratios snapshot POD analysis of the velocity fluctuations outlined a reduction between 55% and 72% in the contributions of modes  $k = 1$  and  $k = 2$ , depending on the streamwise station. The associated spatial eigenmodes showed the occurrence of the anti-symmetric mode  $m = 1$  reflecting wake radial displacement in all directions for diameter ratios  $d/D = 0$  and  $0.2$ . For  $d/D = 0.4$  instead, the dominant fluctuations could be linked with a uni-directional wake displacement.

The present data indicate that even for relatively small afterbody diameter ratios, viz.  $d/D = 0.2$ , the afterbody strongly interferes with the backflow azimuthal fluctuations, thus significantly reducing the near-wake large-scale organization.

## **CHAPTER 8**

### **CONCLUSIONS AND RECOMMENDATIONS**

This thesis surveyed the behavior of turbulent axisymmetric base flows. A main aspect examined in the present work dealt with the flow axial symmetry. More specifically, the role of the axial symmetry of the base and of the inflow conditions was discussed with respect to the development of the long-term unsteadiness typical of such flows. Both the azimuthal and longitudinal flow topology ensuing from this long-term unsteadiness were examined in the discussion. Particular attention was put on the sensitivity of the mean near-wake flow towards angular misalignments. Furthermore, it was of interest to determine to what extent the low-frequency unsteadiness of the near-wake is affected by the base geometry.

Chapter 5 showed that the near-wake long-term unsteadiness comprises two distinct and complementary contributions, associated with the growth of the shear layer and with the erratic behavior of the inner backflow region, respectively. It was found that these two unsteady mechanisms vary along the streamwise direction in opposite ways. The results shown in chapter 6 suggest that the backflow very-low-frequency unsteadiness is intrinsically related to the axial symmetry of the flow. In particular, the inflow conditions appeared to have a major influence on the sensitivity of the near-wake topology towards small misalignment angles between the body and the incoming flow. An essential role of the axial symmetry could be inferred also with respect to the geometry of the base, which displayed a strong impact on the flow reattachment process (cf. chapter 4) and particularly, on its scaling. Lastly, from chapter 4 and 7 it emerged that the base geometry can significantly interfere with the near-wake low-frequency behavior.

These conclusions are elaborated in more details in the following paragraphs.

#### **8.1 Influence of the base geometry on the separated flow behavior**

A major topic of discussion in the present research dealt with the role played by the base geometry in the near-wake development. This point is regarded as most relevant particularly for its implications on industrial flow configurations, notably the case of space launcher vehicles. A parametric study was conducted in chapter 4 on afterbody flows with different diameter ratios modeling axisymmetric BFS flows of varying step height. The primary objective was to assess the discrepancies between afterbody and BFS flows, which could be attributed to three-dimensionality

effects. Secondly, it was of interest to examine how the afterbody to main body diameter ratio affects the large-scale wake fluctuations.

From the discussion it emerges that the reattachment process is especially sensitive to the base geometry, even with only marginal effects on the mean flow topology. The geometry of the base, viz. axisymmetric versus planar, appears to be especially crucial. In particular, it is shown that for the same step height planar and axisymmetric BFS flows feature opposite reattachment behaviors, the discrepancies becoming particularly pronounced with increasing non-dimensional step heights  $h/D$ , while vanishing with decreasing  $h/D$ . Thus, the present data suggest to restrict the customary analogy between planar BFS and afterbody flows (see e.g. Scharnowski and Kähler 2015) to a narrower range of configurations.

A further remarkable effect could be observed on the radial fluctuations associated with the shear layer flapping. Particularly when main body and afterbody diameter are comparable, the central protrusion is shown to inhibit the flapping motion substantially. While previous studies (cf. Dépres *et al* 2004) essentially linked the base flow unsteadiness with the occurrence of a solid shear layer reattachment, the present results indicate that even in presence of a *solid reattachment* the afterbody geometry could determine dramatic differences in the wake fluctuating field.

## **8.2 Streamwise development of the large-scale wake unsteadiness**

The low-frequency unsteadiness of the turbulent wake behind an ogive-cylinder was investigated in chapter 5. The study tackled with particular attention the streamwise evolution of the unsteadiness, which was identified as an open point of discussion at the beginning of this dissertation.

In agreement with previous studies (cf. Rigas *et al* 2014) the present results indicate the coexistence of two distinct contributions of the dominant anti-symmetric mode  $m = 1$ , which could be identified respectively with the flapping motion of the shear layer and with the azimuthal meandering of the inner backflow region. The time-resolved velocity data obtained throughout the near-wake region additionally highlighted a variation in the relative importance of these two unsteady mechanisms. In particular, the very-low-frequency fluctuations of the backflow region were shown intensifying in the stagnation region in proximity of the base, whereas the low-frequency flapping motion of the shear layer was observed to become dominant closer to the rear-stagnation point. Such a variation reflects the growth of the vortical structures in the shear layer and the concurrent vanishing of the inner reversed-flow. With respect to the dynamical behavior of the near-wake, this result indicates that the anti-symmetric fluctuations identified as the dominant mode mode  $m = 1$  tend to involve the whole wake only within the reattachment region, whereas they tend to be confined to the inner reversed-flow moving closer to the base.

The above finding further hints that the wake topology sensitivity towards angular misalignments tends to be especially critical in proximity of the base.

With respect to the former investigations of Rigas *et al* (2014) and Grandemange *et al* (2014), the current results add information on the streamwise evolution of the low-frequency near-wake unsteadiness, which was one of the goals of the present work. Yet, they are retrieved from data acquired at different streamwise stations at uncorrelated time-instants. As a consequence, they do not allow for conclusions on the link between the backflow meandering and the long-term vortex shedding reorientation, which was argued in the previous investigations.

Time-resolved three-dimensional measurements of the near-wake flow could shed light on this point in that they would allow for capturing the simultaneous evolution of the near-wake flow in both the streamwise direction and in the azimuthal-radial plane. This kind of information could be obtained through a large-scale high speed tomographic PIV measurement. The use of large-scale flow tracers, e.g. Helium Filled Soap Bubbles (cf. Caridi *et al* 2016), along with the latest tomographic PIV processing tools, i.e. those based on the Shake the Box algorithm (Schanz *et al* 2016), appears as a promising option to realize such a measurement. This time-resolved large-scale tomographic measurement is herein considered as a most sensible direction for the future research efforts on the subject of turbulent near-wake flows.

### **8.3 Relation between flow symmetry and very-low-frequency wake unsteadiness**

Chapter 6 focused on the relation between the very-low-frequency turbulent wake unsteadiness and the axial symmetry of the inflow conditions. The inner backflow dynamics in the turbulent wake of an ogive-cylinder was examined in presence of small pitch angles, i.e. within  $1^\circ$ . Aim of this parametric study was to define an angular domain of existence for the backflow unsteadiness, which condition appears linked to the axial symmetry of the flow.

The current data show that the axisymmetric turbulent wake features a coherent very-low-frequency meandering of the backflow region only within small deviations from axisymmetric conditions. In particular, angular misalignments between the body and the incoming flow above  $0.1^\circ$  are shown to promote a preferred wake orientation, thus stabilizing the position of the inner reversed-flow. The mean near-wake topology is found to be especially sensitive to the flow orientation within  $0.1^\circ$  deviations from axisymmetric inflow conditions, whereas it exhibits a comparatively weaker sensitivity in presence of larger angles between the body and the freestream flow.

Following from the analysis of the backflow dynamics, the present findings serve a more exhaustive characterization of the turbulent wake sensitivity towards

misalignments. In these regards, they can be considered incremental with respect to previous parametric studies (e.g. Wolf *et al* 2013 among others), whereby the turbulent wake sensitivity was mainly assessed through characterization of the near-wake statistics.

From a practical perspective, they further show that the occurrence of a long-term meandering of the backflow region is irrelevant to most turbulent wake applications, as those involve non-zero angles, see e.g. the case of projectiles and ascending space launchers.

## **8.4 Influence of the base geometry on the azimuthal wake organization and large-scale unsteadiness**

Chapter 7 addressed the influence of the base geometry on the azimuthal-radial turbulent organization and large-scale unsteadiness of a turbulent afterbody flow.

It is shown that even for relatively small diameters the presence of an afterbody prevents the occurrence of a coherent backflow meandering, while being still dominated by the shear layer flapping. For larger diameters the afterbody is found to introduce a preferred orientation for the fluctuations.

Provided a certain caution associated with the stereoscopic measurement uncertainty, the present data suggest that the very-low-frequency backflow fluctuations do not contribute to the unsteadiness of an afterbody flow.

## REFERENCES

- Achenbach, E (1974), “Vortex shedding from spheres”, *J Fluid Mech* **62**(2):209-221.
- Adrian, RJ and Westerweel, J (2011), “Particle Image Velocimetry”, *Cambridge University Press*.
- Ashok, A, van Buren, T, and Smits, AJ (2015), “Asymmetries in the wake of a submarine model in pitch”, *J Fluid Mech* **774**:416-442.
- Ashok, A, van Buren, T and Smits, AJ (2015), “The structure of the wake generated by a submarine model in yaw”, *Exp Fluids* **56**:123.
- Auguste, F, Fabre, D and Magnaudet, J (2010) “Bifurcations in the wake of a thick circular disk”, *Th Comp Fluid Dyn* **24**:305-313.
- Benedict, LH and Gould, LD (1996) “Towards better uncertainty estimates for turbulence statistics”, *Exp Fluids* **22**(2):129-136.
- Berkooz, G, Holmes, P and Lumley, JL (1993) “The proper orthogonal decomposition in the analysis of turbulent flows”, *Annu Rev Fluid Mech* **25**:539-575.
- Bobinski, T, Goujon-Durand, S and Wesfreid, JE (2014) “Instabilities in the wake of a circular disk”, *Phys Rev E* **89**(5):053021.
- Bohorquez, P, Sanmiguel-Rojas, E, Sevilla, A, Jiménez-Gonzalez, JI and Martínez-Bazàn, C (2011) “Stability and dynamics of the laminar wake past a slender blunt-based axisymmetric body”, *J Fluid Mech* **676**:110-144.
- Bourdon, CJ and Dutton, JC (1999) “Planar visualizations of large-scale turbulent structures in axisymmetric supersonic separated flows”, *Phys Fluids* **11**(1):201.
- Brücker, C (2001) “Spatio-temporal reconstruction of vortex dynamics in axisymmetric wakes”, *J Fluids Struct* **15**(3):543-554.
- Bury, Y and Jardin, T (2012) “Transitions to chaos in the wake of an axisymmetric bluff body”, *Ph Lett A* **376**:3219-3222.
- Calvert, JR, (1967) “Experiments on the flow past an inclined disk”, *J Fluid Mech* **29**(4):691-703.
- Caridi, CA, Ragni, D, Sciacchitano, A and Scarano, F (2016) “HFSB-seeding for large-scale tomographic PIV in wind tunnels”, *Exp Fluids* **57**(12):190.
- Choi, H, Jeon, WP and Kim, J (2008) “Control of flow over a bluff body”, *Annu Rev Fluid Mech* **40**:113-139.
- Chomaz, JM (2005) “Global instabilities in spatially developing flows: Non-Normality and Nonlinearity”, *Annu Rev Fluid Mech* **37**:357-392.
- Deck, S and Thorigny, P (2007) “Unsteadiness of an axisymmetric separating-reattaching flow: Numerical investigation”, *Phys Fluids* **21**:075103.
- Del Taglia, C, Blum, L, Gass, J, Ventikos, Y and Poulidakos, D (2004) “Numerical and Experimental Investigation of an Annular Jet Flow With Large Blockage”, *J Fluids Eng* **126**(3):375-384.
- Délery, JM (2001) “Robert Legendre and Henri Werlé: Toward the Elucidation of Three-Dimensional Separation”, *Annu Rev Fluid Mech* **33**:129-154.
- Dépres, D, Reijasse, P and Dussauge, JP (2004) “Analysis of Unsteadiness in Afterbody Transonic Flows”, *AIAA J* **42**(12):2541-2550.

Eaton, JK and Johnston, JP (1981) "A Review of Research on Subsonic Turbulent Flow Reattachment", *AIAA J* **19**(9):1093-1100.

Fabre, D, Auguste, F and Magnaudet, J (2008) "Bifurcations and symmetry breaking in the wake of axisymmetric bodies", *Phys Fluids* **20**:051702.

Fuchs, HV, Mercker, E and Michel, U (1979) "Large-coherent structures in the wake of axisymmetric bodies", *J Fluid Mech* **93**:185-207.

Gentile, V, Schrijer, FFJ, van Oudheusden, BW and Scarano, F (2016) "Low-frequency behavior of the turbulent axisymmetric near-wake", *Phys Fluids* **28**(6):065102.

Gentile, V, Schrijer, FFJ, van Oudheusden, BW and Scarano, F (2016) "Afterbody Effects on Axisymmetric Base Flows", *AIAA J* **54**(8):2285-2294.

Gentile, V, Schrijer, FFJ, van Oudheusden, BW and Scarano, F (2016) "Organization of an axisymmetric turbulent wake in presence of a central protrusion", *Segalini A. (eds) (ICJWSF2015). Springer Proceedings in Physics* **185**:157-163.

Gerrard, JH (1966) "The mechanics of the formation region of vortices behind bluff bodies", *J Fluid Mech* **25**(2):401-413.

Gohlke, M, Beaudoin, JF, Amielh, M, and Anselmet, F (2008) "Thorough analysis of vortical structures in the flow around a yawed bluff body", *J Turb* **9**(15).

Grandemange, M, Gohlke, M and Cadot, O (2012) "On experimental sensitivity analysis of the turbulent wake from an axisymmetric blunt trailing edge", *Phys Fluids* **24**(3):035106.

Grandemange, M, Gohlke, M and Cadot, O (2012) "Turbulent wake past a three-dimensional blunt body. Part 1. Global modes and bi-stability", *J Fluid Mech* **722**:51-84.

Grandemange, M, Gohlke, M and Cadot, O (2013) "Turbulent wake past a three-dimensional blunt body. Part 2. Experimental sensitivity analysis", *J Fluid Mech* **752**:439-461.

Grandemange, M, Gohlke, M and Cadot, O (2014) "Statistical axisymmetry of the turbulent sphere wake", *Exp Fluids* **55**(11):1838.

Hannemann, K, Pallegoix, JF, Lambaré, H, Maseland, J, Frey, AM, Deck, S, Schrijer, FFJ and Schwane, R (2011) "Launch vehicle base buffeting - recent experimental and numerical investigations", *7th European Aerothermodynamics Symposium on Space Vehicles*, Noordwijk: ESA-ESTEC, The Netherlands.

Herrin, JL, and Dutton, JC (1994) "Supersonic near-wake afterbody boattailing effects on axisymmetric bodies", *J Spacec Rockets* **31**(6): 1021-1028.

Hudy, LM, Naguib, AM, Humphreys, WM and Bartram "PIV Measurements of a 2D/3D Separating/Reattaching Boundary Layer Downstream of an Axisymmetric Backward-facing Step", *43rd AIAA Aerospace Science Meeting and Exhibit*, Reno, Nevada, 10-13 January, 2005.

Huerre, P and Monkewitz, PA (1990) "Local and Global Instabilities in Spatially Developing Flows", *Annu Rev Fluid Mech* **22**:473-537.

Jovic, S and Driver, MD (1994) "Backward-Facing Step Measurements at Low Reynolds Number,  $Re_h = 5000$ ", NASA TM-108807.

Klei, CE “Investigation of the Recirculation Region of a Generic Rocket Configuration Using Stereoscopic PIV”, *8th Pegasus-AIAA Student Conference*, Poitiers, France, 11-13 April, 2012.

Le, H, Moin, P and Kim, J (1997) “Direct numerical simulation of turbulent flow over a backward-facing step”, *J. Fluid Mech* **330**(1):349-374.

Lumley, JL (1967) “The structure of inhomogeneous turbulence”, *Atmospheric Turbulence and Wave Propagation*, AM Yaglom and VI Tatarski, 166-178, Moscow: Nauka.

Meinhart, CD, Wereley, ST and Santiago, JG (1999) “PIV measurements of a microchannel flow”, *Exp Fluids* **27**(5):414-419.

Meliga, P, Chomaz, JM and Sipp, D (2009) “Global mode interaction and pattern selection in the wake of a disk: a weakly nonlinear expansion”, *J Fluid Mech* **633**:159-189.

Merz, RA, Przirembel, CEG and Page, RH (1978) “Subsonic Axisymmetric Near-wake Studies”, *AIAA J* **16**(7):656-662.

Merz, RA (1979) “Subsonic Base Pressure Fluctuations”, *AIAA J* **17**(4):436-438.

Michelis, T and Kotsonis, M (2015) “Interaction of an Off-surface Cylinder with Separated Flow from a Bluff Body Leading Edge”, *Exp Th Fluid Sci* **19**(6):91-105.

Monkewitz, PA (1988) “A note on vortex shedding from axisymmetric bodies”, *J Fluid Mech* **192**: 561-575.

Oertel, H Jr (1990) “Wakes behind blunt bodies”, *Annu Rev Fluid Mech* **22**:539-564.

Oxlade, AR, Morrison, JF, Qubain, A and Rigas, G (2015) “High-frequency forcing of a turbulent axisymmetric wake”, *J Fluid Mech* **770**:305–318.

Pain, R, Weiss, PE and Deck, S (2014) “Zonal Detached Eddy Simulation of the Flow Around a Simplified Launcher Afterbody” **52**(9):967-1979.

Prasad, AK (2000) “Stereoscopic particle image velocimetry”, *Exp Fluids* **29**(2):103-116.

Provansal, M, Mathis, C and Boyer, L (1987) “Bernard von Karman instability: transient and forced regimes”, *J Fluid Mech* **182**:1-22.

Raffel, M, Willert, CE, Wereley, S and Kompenhans, J (2007) “Particle Image Velocimetry - A Practical Guide”, *Springer*, New York, 2<sup>nd</sup> edition.

Ragni, D, Schrijer, F, van Oudheusden, BW, and Scarano, F (2010) “Particle tracer response across shocks measured by PIV”, *Exp Fluids* **57**(12):190.

Rigas, G, Oxlade, AR, Morgans, AS and Morrison, JF (2014) “Low-dimensional dynamics of a turbulent axisymmetric wake”, *J Fluid Mech* **755**:185-207.

Rigas, G, Oxlade, AR, Morgans, AS, Brackston, RD and Morrison, JF (2015) “Diffusive dynamics and stochastic models of turbulent axisymmetric wakes”, *J Fluid Mech* **778**.

Roshko, A, (1955) “On the wake and drag of bluff bodies”, *J Aero Sc* **22**(2):124-132.

Samimy, M and Lele, SK “Motion of particles with inertia in a compressible free shear layer”, *Phys Fluids* **3**:1915-1923.

Sanmiguel-Rojas, E, Sevilla, A, Martinez-Bazàn, C, Chomaz, JM (2009) “Global mode analysis of axisymmetric bluff body wakes: Stabilization by base bleed”, *Phys Fluids* **21**:114102.

Scarano, F (2012) “Tomographic PIV: Principles and Practice”, *Meas Sci Tech* **24**(1):012001.



## References

- Scarano, F and Benocci, C and Riethmuller, ML (1999) "Pattern recognition analysis of the turbulent flow past a backward facing step", *Phys Fluids* **11**(12):3808-3818.
- Scarano, F and Riethmuller, ML (2000) "Advances in Iterative Multigrid PIV Image Processing", *Exp Fluids* **29**(1):S51-S60.
- Schanz, D, Gesemann, S and Schröder A (2016) "Shake-The-Box: Lagrangian particle tracking at high particle image densities", *Exp Fluids* **57** (5):1-27.
- Scharnowski, S and Kähler, CJ (2015) "Investigation of a transonic separating/reattaching shear layer by means of PIV", *Theor Appl Mech Lett* **5**(1):5-9.
- Schrijer, F, Sciacchitano, A, Scarano, F, Hanneman, K, Pallegoix, J, Maseland, J and Schwane, R "Experimental Investigation of Base Flow Buffeting on the Ariane 5 Launcher Using High Speed PIV", *7th European Symposium on Aerothermodynamics for Space Vehicles*, Brugge, Belgium, 9-12 May, 2011.
- Schwarz, V, Bestek, H and Fasel, H (1994) "Numerical simulation of Nonlinear Waves in the Wake of an Axisymmetric Bluff Body", *25th AIAA Fluid Dynamics Conference*, Colorado Springs, Colorado, 20-23 June, 1994.
- Schrijer, FFJ, Sciacchitano, A and Scarano, F (2014) "Spatio-temporal and modal analysis of unsteady fluctuations in a high-subsonic base flow", *Phys Fluids* **26**:086101.
- Siacci, F (1888) "Balistica", *Casanova*, Torino, 2<sup>nd</sup> edition.
- Simpson, RL (2001) "Junction Flows", *Annu Rev Fluid Mech* **33**:415-443.
- Sirovich, L (1987) "Turbulence and the dynamics of coherent structures. Part 1-3", *Quarterly of Applied Mathematics* XLV **3**:561-590.
- Slessor, MD, Zhuang, M, and Dimotakis, PE (2000) "Turbulent shear-layer mixing: growth-rate compressibility scaling", *J Fluid Mech* **414**:35-45.
- Smits, AJ and Dussauge, JP (2006) "Turbulent Shear Layers in Supersonic Flow", *Springer*, New York, 2<sup>nd</sup> edition.
- Soloff, SM, Adrian, RJ and Liu, ZC (1997) "Distortion compensation for generalized stereoscopic particle image velocimetry", *Meas Sc Techn* **8**(12):1441-1454.
- Spazzini, PG, Iuso, G, Onorato, M, Zurlo, N and Di Cicca, GM (2001) "Unsteady behavior of back-facing step flow Unsteady Behavior of Back-Facing Step Flow", *Exp Fluids* **30**(5):551-561.
- Strogatz, SH (2000) "Nonlinear dynamics and chaos: with applications to physics, biology, chemistry, and engineering", *Perseus Books publishing*, Massachusetts.
- Taneda, S (1956) *J Phys Soc Jpn* **11**:306-307.
- Thompson, MC, Leweke, T and Provansal, M (2001) "Kinematics and dynamics of sphere wake transition", *J Fluids Struct* **15**(3-4):575-585.
- Townsend, AA (1956) "The structure of turbulent shear flow", *J Fluid Mech* **1**(5):554-560.
- van Dyke, M (1982) "An Album of Fluid Motion", *The Parabolic Press*, Stanford, California.
- van Oudheusden, BW, Scarano, F, van Hinsberg, NP and Watt, DW (2005) "Phase-resolved characterization of vortex shedding in the near-wake of a square-section cylinder at incidence", *Exp Fluids* **39**:86-98.

- Vanierschot, M and Van den Bulck, E (2011) “Experimental study of low precessing frequencies in the wake of a turbulent annular jet”, *Exp Fluids* **50**(1):189-200.
- Weiss, PE and Deck, S (2011) “Control of the antisymmetric mode  $m=1$  for high Reynolds axisymmetric turbulent separating/reattaching flows”, *Phys Fluids* **23**:095102.
- Westerweel, J (1997) “Fundamentals of digital particle image velocimetry”, *Meas Sci Tech* **8**:1379-1392.
- Westerweel, J and Scarano, F (2005) “Universal Outlier Detection for PIV Data”, *Exp Fluids* **39**(6):1096-1100.
- Westerweel, J, Elsinga, GE and Adrian, RJ (2012) “Particle Image Velocimetry for Complex and Turbulent Flows”, *Annu Rev Fluid Mech* **45**:409-436.
- Wieneke, B (2005) “Stereo-PIV using self-calibration on particle images”, *Exp Fluids* **39**(2):267-280.
- Williamson, CK (1996) “Vortex Dynamics in the Cylinder Wake”, *Annu Rev Fluid Mech* **28**:477-539.
- Wolf, CC (2012) “The Subsonic Near-Wake of Bluff Bodies, PhD thesis, Aachen University Press.
- Wolf, CC, Henke, R and Hörschemeyer, R (2010) “Investigation on turbulence properties in the wake of a generic rocket model”, Sonderforschungsbereich/Transregio 40–Annual Report.
- Wolf, CC, Klei, CE, Buffo, RM, Hörschemeyer, R and Stumpf, E (2012) “Comparison of Rocket Near-wakes with and without Nozzle Simulation in Subsonic Freestream Conditions”, *42nd AIAA Fluid Dynamics Conference and Exhibit*, New Orleans, Louisiana, 25-28 June, 2012.
- Wolf, CC, You, Y, Hörschemeyer, R, Lüdeke, H and Hannemann, V (2013) “Base-flow sensitivity of a generic rocket forebody towards small freestream angles” EUCASS Proceedings Series – Advances in Aerospace Sciences **5**:169-190.

## LIST OF PUBLICATIONS

### Journal papers

Gentile, V, van Oudheusden, BW, Schrijer, FFJ, and Scarano, F (2017) “The effect of angular misalignment on low-frequency axisymmetric wake instability”, *J Fluid Mech* **813**:R3.

Gentile, V, Schrijer, FFJ, van Oudheusden, BW and Scarano, F (2016) “Afterbody Effects on Axisymmetric Base Flows”, *AIAA J* **54**(8):2285-2294.

Gentile, V, Schrijer, FFJ, van Oudheusden, BW and Scarano, F (2016) “Low-frequency behavior of the turbulent axisymmetric near-wake”, *Phys Fluids* **28**(6):065102.

### Conference proceedings

van Gent, PL, Gentile, V, Schrijer, FFJ, and van Oudheusden, BW “Experimental assessment of PIV/PTV-based pressure reconstruction techniques applied to a low-speed base flow”, *6<sup>th</sup> Workshop on non-intrusive measurements for unsteady flows and aerodynamics*, Delft, The Netherlands, 25-26 October, 2016.

Gentile, V, Schrijer, FFJ, and van Oudheusden, BW “Very-low-frequency instability of an axisymmetric body”, *6th Workshop on non-intrusive measurements for unsteady flows and aerodynamics*, Delft, The Netherlands, 25-26 October, 2016.

Gentile, V, Schrijer, FFJ, van Oudheusden, BW and Scarano, F “Low-frequency wake instability of an axisymmetric bluff body in pitch”, *18th International Symposium on Symposium on the Application of Laser and Imaging Techniques to Fluid Mechanics*, Lisbon, Portugal, 4-7 July, 2016.

Blinde, PL, Gentile, V, Schrijer, FFJ, and van Oudheusden, BW “Determination of instantaneous pressure in an axisymmetric base flow using time-resolved tomographic PIV”, *4th Workshop on non-intrusive measurements for unsteady flows and aerodynamics*, Poitiers, France, 26-27 October, 2015.

Gentile, V, Schrijer, FFJ, van Oudheusden, BW and Scarano, F “Time-dependent behaviour of the recirculation region behind an axisymmetric bluff body”, *9th International Symposium on Turbulence and Shear Flow Phenomena*, Melbourne, Australia, 30 June-3 July, 2015.

Gentile, V, Schrijer, FFJ, van Oudheusden, BW and Scarano, F “Azimuthal organization of an axisymmetric turbulent wake in presence of a central

protrusion”, *5th International Conference on Jets, Wakes and Separated Flows*, Stockholm, Sweden, 15-18 June, 2015.

Gentile, V, Schrijer, FFJ, van Oudheusden, BW and Scarano, F “Afterbody Effects on Axisymmetric Base Flows”, *53rd AIAA aerospace sciences meeting*, Kissimee (FL), USA, 5-9 January, 2015.

## **Book chapters**

Gentile, V, Schrijer, FFJ, van Oudheusden, BW and Scarano, F (2016) “Organization of an axisymmetric turbulent wake in presence of a central protrusion”, *Segalini A. (eds) (ICJWSF2015). Springer Proceedings in Physics 185:157-163.*

## **Reports**

Buoso, S, Gentile, V, and Tol, H (2016) “Weakly non-linear expansion of the Ginzburg-Landau equation”, *ERCOfTAC Spring School on reduced-order models for non-linear dynamics in fluid flows*, Montestigliano, Italy, 17-22 April, 2016.

# CURRICULUM VITAE

02-05-1988      Born in Crotone, Italy

## Education

2012-2017      **Doctor of Philosophy**

Thesis title: *Turbulent axisymmetric base flows: Symmetry and long-term behavior*  
Aerospace Engineering  
Delft University of Technology, The Netherlands

2009-2012      **Master of Science**

Thesis title: *Modeling of thermo-ablative phenomena by means of ESATAN-TM software*  
Space Engineering  
Sapienza University of Rome, Italy

2006-2009      **Bachelor of Science**

Thesis title: *Thruster systems for spacecraft attitude control*  
Aerospace Engineering  
Sapienza University of Rome, Italy

## Experience

2011-2012      **Internship**

Avio S.p.A., Colleferro, Italy

## ACKNOWLEDGEMENTS

This work comes out as a great time investment and exercise of patience, not only from my side. As such, it owes its existence to all the people who gave me support and encouragement throughout the time I have been a Ph.D. student at TU Delft. I would like to use this last chapter to express my appreciation for them.

I owe my very first thanks to my supervisor and promotor Prof. Fulvio Scarano for his guidance during these important four years of my life. Thank you, Fulvio for pushing me out of my shell, for being a great teacher and for your enduring patience towards my plot labeling skills. Thanks to Dr. Bas van Oudheusden for being dependable and clear, providing scientifically-righteous suggestions. Thanks to Dr. Ferry Schrijer for his friendly supervision, especially at the beginning of my Ph.D. Thank you Ferry, for giving me the opportunity to assist you in your courses and thus, learn a lot about managing time, as well as people. Thanks for your dedication in pulling bluntness out of me and also, for sparing some whenever I could not bear it. Thanks to the three of you for keeping an eye on how I was doing during this time.

This work could not have been possible without the assistance of the technicians of the Aerodynamics department of TU Delft, Frits Donker Duyvis, Peter Duyndam, Henk-Jan Siemer and Nico van Beek. Special thanks to you, Peter, for being cool about getting instructions from poorly-written sticky notes and thanks Frits, for helping out with the expensive equipment and for sharing Gilmour's tour dates with me. Thank you Colette, for managing my unfortunate planning skills and my stress waves and for being up for help on all sorts of matters.

Thanks to Dr. Marios Kotsonis for dispensing unrequested honesty and countless free drinks, to Dr. Andrea Sciacchitano and Dr. Mustafa Perçin for their advises and brotherly mockeries.

Thanks to my PhD fellows Koen, Martin, Paul, Qingqing, Rakesh, Shaafi, Tiago, Varun, Wouter, Zeno, for making working hours and lunch breaks lighter. My deep gratitude to my colleague Theo Michelis, who has shared with me working space and time, apartments, thoughts and a great deal of amusement during these years. Grazie a Jacopo Serpieri for winning my *hydrophobic* attitude with well-concealed attentions and shrilly sound effects. Thanks to Beppe Caridi, for his availability and kindness and to Jan Schneiders, for his candor and for the genuine interest in roman street jargon. Thanks to my former colleague Dr. Kyle Lynch for the patient supervision during my first PIV (un)experiences.

Special thanks to Dr. Daniele Ragni, Dr. Francesco Avallone and Carlos Arce León from the Aeroacoustics section. Thanks Dani, for your affection and generosity. Thanks Fra for your friendship and chill help and for your misplaced trust in my reading suggestions. Thanks Carlos, for being friendly and supportive, particularly during my very first test campaign. Thanks also to the girls from Delft, Greta, Sara and

Sere for the nice time spent together. Thanks to my good friend Sogol Nayeri for her wisdom and tasteful haircuts.

I here take the opportunity to express my gratitude to my Coolhaven buddy, Egle Kalonaityte for her time, care and appreciation. Thank you Egle, for being a paranymp during my defense and in many other occasions, for the small and big talks we shared, the laughter and your questionable zest for 80's music.

BLM Martina Bertola, my friend from the other side of Piazza Vittorio, for your understanding, loyalty and trust.

Thanks to Martina Orlandi, for the truthful advises on life, people, academia and for acknowledging my diplomacy skills.

Thanks to Claudia Rischer for being such a lovely flatmate in Delft, and fun buddy in many other places across Europe. Thanks to Julia Moser for keeping in touch with me from down under and for the nice time in Melbourne.

I could not miss to mention my genuine appreciation for my friends back in Rome. Thanks to Silvia Falcone, for everything. Major thanks to Nadia D'Ippolito Merrar, who has shared plenty with me through the years. Thanks, Nad for being such a challenging friend, for never being boring nor clumsy, for decrypting my words and getting the unspoken ones. Thanks to Viviana Proietti for her friendship and curiosity towards what and how I do in life. Special thanks to Matteo Tiberi for skillfully editing the cover of my thesis. Thanks to Gabu, France, Mara, Fabrizio, Silla, Domenico, Luca, Sabrina.

Finally, I would like to thank my parents, who raised me at their best and never treated me as if I were better than the other kids. Thanks to my mother, Susanna, who taught me the importance of discipline and to my father, Rizieri, for showing me the value of being rebel sometimes. I would like to acknowledge also the energy and support I got from my aunt Gabriella and from my cousin Giulia. Thanks also to Beppe, who still pushes me into being an educated kid. Thanks to my sister in law, Milla for her help and reliability in several occasions. Lastly, I want to acknowledge my brother, Claudio, for providing most unwanted, yet important supervision on my life. Mi raccomando.

Delft, April 6, 2017